SOURCE-CHANNEL CODING FOR ROBUST IMAGE TRANSMISSION AND FOR DIRTY-PAPER CODING

A Dissertation

by

YONG SUN

Submitted to the Office of Graduate Studies of
Texas A&M University
in partial fulfillment of the requirements for the degree of

DOCTOR OF PHILOSOPHY

December 2005

Major Subject: Electrical Engineering

SOURCE-CHANNEL CODING FOR ROBUST IMAGE TRANSMISSION

AND FOR DIRTY-PAPER CODING

A Dissertation

by

YONG SUN

Submitted to the Office of Graduate Studies of
Texas A&M University
in partial fulfillment of the requirements for the degree of

DOCTOR OF PHILOSOPHY

Approved by:

Chair of Committee,   Zixiang Xiong
Committee Members,   Costas N. Georghiades
    Andrew K. Chan
    Andreas Klappenecker
Head of Department,   Costas N. Georghiades

December 2005

Major Subject: Electrical Engineering

ABSTRACT

Source-channel Coding for Robust Image Transmission

and for Dirty-paper Coding. (December 2005)

Yong Sun, B.S., Tsinghua University, Beijing, P.R.China;

M.S., Tsinghua University, Beijing, P.R.China

Chair of Advisory Committee: Dr. Zixiang Xiong

In this dissertation, we studied two seemingly uncorrelated, but conceptually related problems in terms of source-channel coding: 1) wireless image transmission and 2) Costa ("dirty-paper") code design.

In the first part of the dissertation, we consider progressive image transmission over a wireless system employing space-time coded OFDM. The space-time coded OFDM system based on a newly built broadband MIMO fading model is theoretically evaluated by assuming perfect channel state information (CSI) at the receiver for coherent detection. Then an adaptive modulation scheme is proposed to pick the constellation size that offers the best reconstructed image quality for each average signal-to-noise ratio (SNR).

A more practical scenario is also considered without the assumption of perfect CSI. We employ low-complexity decision-feedback decoding for differentially space-time coded OFDM systems to exploit transmitter diversity. For JSCC, we adopt a product channel code structure that is proven to provide powerful error protection and bursty error correction. To further improve the system performance, we also apply the powerful iterative (turbo) coding techniques and propose the iterative decoding of differentially space-time coded multiple descriptions of images.

The second part of the dissertation deals with practical dirty-paper code designs.

We first invoke an information-theoretical interpretation of algebraic binning and motivate the code design guidelines in terms of source-channel coding. Then two dirty-paper code designs are proposed. The first is a nested turbo construction based on soft-output trellis-coded quantization (SOTCQ) for source coding and turbo trellis-coded modulation (TTCM) for channel coding. A novel procedure is devised to balance the dimensionalities of the equivalent lattice codes corresponding to SOTCQ and TTCM. The second dirty-paper code design employs TCQ and IRA codes for near-capacity performance. This is done by synergistically combining TCQ with IRA codes so that they work together as well as they do individually. Our TCQ/IRA design approaches the dirty-paper capacity limit at the low rate regime (e.g., < 1.0 bit/sample), while our nested SOTCQ/TTCM scheme provides the best performs so far at medium-to-high rates (e.g., ≥ 1.0 bit/sample). Thus the two proposed practical code designs are complementary to each other.

To my parents.

ACKNOWLEDGMENTS

It is with great appreciation that I acknowledge my advisor, Prof. Zixiang Xiong, for his patient guidance and constant support. Since the first project with him, I have been impressed by his broad knowledge and academic excellence. This dissertation would never have been possible without his insight and encouragement.

I would like to thank my committee members Prof. Costas N. Georghiades, Prof. Andrew K. Chan and Prof. Andreas Klappenecker for taking time to review this dissertation and give valuable feedback. I would also like to thank Prof. Xiaodong Wang for his motivations and suggestions on the work in the first part of my dissertation.

Many thanks are also due to Dr. Vladimir Stanković, Dr. Angelos Liveris and Dr. Samuel Cheng. Their kind help and valuable comments have always been of great benefit to my research.

Finally, I would like to express my gratitude to Yiwen Wang, Kun Men and all my current and former colleagues in Wireless Communication Lab. I would never forget the happy time with you at A&M!

TABLE OF CONTENTS

LIST OF TABLES

LIST OF FIGURES

CHAPTER I

INTRODUCTION

In this dissertation, two research problems are investigated: 1) robust image transmission over wireless channels; 2) practical Costa ("dirty-paper") code design. They are seemingly uncorrelated, but conceptually related in their nature of source-channel coding.

A.   Robust Image Transmission over Wireless Channels

Shannon's information separation theorem [1, 2] states that in a communication system, one can optimize the source coding (data compression) and channel coding (error protection) separately without any performance loss. However, this only holds under the assumptions of infinite delay and complexity (e.g., infinite long codeword length), which are usually invalid in practice. In recent years, considerable interests have developed in various schemes of joint source-channel coding (JSCC). That is, jointly optimized source-channel coders are employed to tradeoff the source and channel coding and thus achieve significant performance improvement over separate source and channel coding.

One example is the wireless image communication system, which is becoming more popular with the increasing demands for efficient progressive multimedia transmission over wireless channels. Progressive transmission is motivated by the embedded nature of state-of-the-art of image coders such as SPIHT [3] and JPEG2000 [4]. These scalable coders have the attractive feature that any initially received portion of the source bitstream can be used to decoded an image with quality commensurate

The journal model is *IEEE Transactions on Communications.*

with the bitrate and that additional received source bits can be used to improve upon the image quality. Intuitively, information bits in an embedded bitstream have decreasing orders of significance, i.e., the first bit is the most important, the second bit is less important, and so on. For progressive image transmission over noisy channels, this necessitates unequal error protection (UEP) in JSCC: more error protection for the beginning part of the source coded image bitstream, less protection for the middle part, and yet less or even no protection for the last part.

Most works on wireless multimedia transmission assume a memoryless (e.g., BSC and AWGN) channel [5, 6, 7]. For fading channels, a two-state Gilbert-Elliot model is employed to simulate bursty errors in [8]. The JSCC design in [8] targets at *bad* channel conditions and hence is not optimal for *good* channel conditions. Image transmission over practical wireless channels was recently studied by Song and Liu [9]. They evaluated the space-time coded orthogonal frequency-division multiplexing (STC-OFDM) system and proposed a practical UEP scheme for JSCC with Reed-Solomon (RS) codes because of their good bursty error correction capability.

In this dissertation, we consider a new system that integrates progressive image coding, channel coding, signal modulation and antenna diversity for wireless image transmission. Specifically, we study the progressive image transmission with JSCC over STC-OFDM systems, as illustrated in Fig. 1. The image is first fed into the embedded image coder (e.g., SPIHT [3] and JPEG2000 [4]). Based on JSCC, the source bitstream is transformed into a sequence of packets by the channel encoders. Note that UEP is fulfilled by providing more error protection for the significant (beginning) part of the bitstream. We transmit all the packets through the STC-OFDM system with multiple antennas. At the receiver, the sent symbols are first detected via STC-OFDM decoding. Then after channel decoding, part of bitstream can be recovered from the correctly decoded packets. The image decoder reconstructs the transmitted

image using the source bits before the first error in the recovered bitstream.

Transmitter
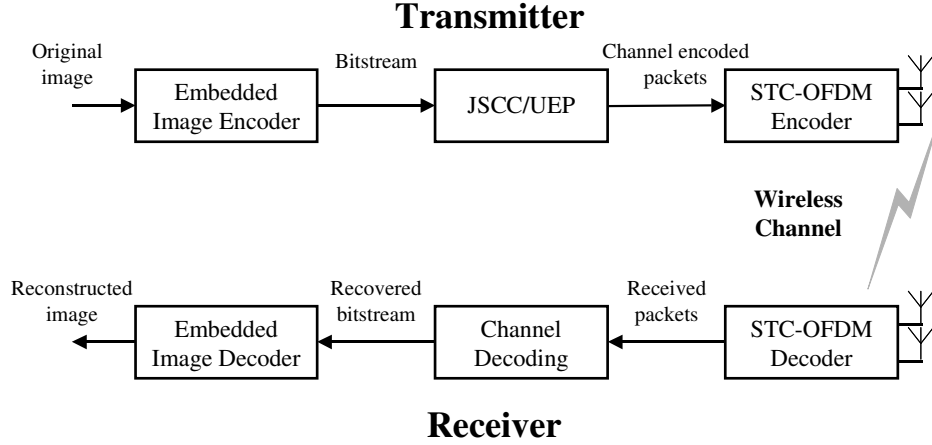
Fig. 1. Progressive image transmission system over STC-OFDM systems.

Orthogonal frequency-division multiplexing (OFDM) is a multi-carrier digital modulation technique that is becoming more and more popular. It has been shown to be effective for digital audio and digital video broadcasting in Europe. The IEEE 802.11 standard uses OFDM modulation for wireless LANs operating at bit rates up to 30 Mbps at 5 GHz. In OFDM [10, 11], the entire channel is divided into many narrow sub-channels through which data are transmitted in parallel, thereby increasing the symbol duration and reducing inter-symbol interference. In addition, OFDM transforms a frequency-selective fading channel into a set of parallel flat-fading channels. Recent works have addressed channel estimation and receiver design for STC-OFDM systems [12, 13].

Space-time coding (STC), which integrates spatial diversity in antenna array and channel coding, can provide significant capacity gains in wireless channels. Since Alamouti introduced a simple transmission scheme with two transmit antennas [14], there have been many recent works addressing the design and applications of STC [15, 16, 17, 18]. Most research on STC system design assumes that the receiver

knows the fading channel state information (CSI) for coherent detection. When no CSI is available, two methods are usually used for non-coherent detection. One is to estimate the CSI before performing decoding [13, 19, 20]. Iterative techniques (e.g., the expectation-maximization (EM) algorithm [21, 22]) are usually used in receiver design with good performance but at high computational complexity. More recently, Lu *et al.* designed an iterative receiver for STC-OFDM systems in unknown wireless dispersive fading channels in [12] with reduced complexity.

Another approach to exploiting transmit diversity while not requiring the CSI at the receiver is differential space-time coding (DSTC) [23, 24]. When compared with the algorithms based on CSI estimation (e.g., EM-based iterative receiver for space-time coded OFDM systems [12]), DSTC is attractive due to its robustness and low computational complexity. It is also more power-efficient since no pilot symbols are required to track the CSI. However, DSTC exhibits an error floor when employed in fading channels, just like the conventional differential demodulation schemes. The usual solution is multiple-symbol detection (MSD) [25], which makes use of ML sequence estimation rather than symbol-by-symbol detection as in conventional differential detection. However, MSD has relatively high computational complexity. A low-complexity DSTC technique, which considerably reduces the error floor, especially in fast fading channels, is developed in [26] based on multiple-symbol decision-feedback decoding [27, 28].

Although embedded source coding, STC and OFDM have been treated separately under different contexts of communications system design, for the specific problem (of progressive image transmission over STC-OFDM systems) addressed here and many related more general problems, the tight coupling between these source and channel coding components in the form of UEP becomes interesting and challenging. Were it not for the embedded nature of source coding, EEP would suffice and separate

designs of source coding and channel coding (or coded modulation) would be optimal by Shannon's separation theorem [1, 2].

Having motivated the choice of embedded image coding, STC and OFDM, we now address the main problem arising from the need of UEP in JSCC: an actual fast UEP algorithm for assigning different channel code rates to different parts of the source bitstream. Note that the UEP algorithm has to be fast to accommodate time-varying wireless channel conditions.

An extremely fast near-optimal algorithm based on *local search* was presented in [29]. Armed with this fast UEP algorithm, we covert the problem of progressive image transmission over STC-OFDM systems into one of optimal JSCC in the form of UEP. Specifically, for a given signal-to-noise ratio (SNR), the BER performance of the space-time coded OFDM system is treated as the channel condition in the JSCC/UEP design so that the end-to-end quality of reconstructed images is optimized in the average minimum mean square error (MSE) sense. This is different from most data communications system designs where the aim is often to minimize the BER and the smaller the BER (e.g., $< 10^{-6}$) the better. In addition, JSCC design is targeted at allowing image communication systems to operate at a much higher BER (hence lower SNR) range (e.g., from 10^{-3} to 10^{-1}), while limiting the occurrence of bad image quality (due to channel decoding error) to less than one in a thousand image transmissions. Because low SNR can be transformed into savings in power, our new philosophy in JSCC should impact the design of future wireless image transmission systems.

1. Main Contributions

Depending on the availability of the CSI at the receiver in STC-OFDM systems, this work has the following novelties:

1. <u>Coherent detection</u>: We first assume perfect CSI at the receiver and set up the whole progressive image transmission system. One important contribution is the introduction of a **newly built broadband multiple-input multiple-output (MIMO) fading model**, with both time-domain fading correlation due to Doppler shift and spatial-domain fading correlation among different receive antennas induced by the surrounding environmental parameters. Coherent detection allows us to theoretically analyze its BER performance. We also introduce **adaptive modulation** as an additional mechanism for optimizing system performance.

2. <u>Non-coherent detection</u>: When CSI is not available at the receiver in practical applications, the low-complexity decision-feedback differential-detection receiver is adopted due to the increasing demand of real-time wireless communication. Based on this image transmission system with DSTC, we propose the **iterative decoding of differentially space-time coded multiple descriptions of images** to further improve the system performance with successive iterations.

B. Practical Costa ("Dirty-paper") Coding

Our second research topic concerns with practical code designs for the celebrated Costa ("dirty-paper") problem [30]. We start by reviewing the original background knowledge on channel coding with side information (CCSI) at the encoder, i.e., Gelfand-Pinsker coding [31].
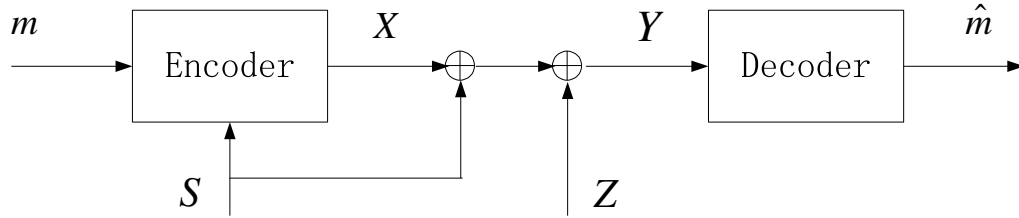
Fig. 2. Gelfand-Pinsker coding or CCSI at the encoder.

Gelfand-Pinsker coding [31] is schematically shown in Fig. 2. The transmitter wishes to send message $m \in \{1, \ldots, M\}$ over a memoryless channel, which is defined by the transition probabilities $p(y|x, s)$, where X and Y are the channel input and output, respectively, the i.i.d. random variable S is the state of the channel (side information) known non-causally to the encoder but not to the decoder. X and Y are related by

$$Y = X + S + Z, \tag{1.1}$$

where Z is the channel noise. Based on the selected message m and the side informa-tion S, the encoder sends X, which must satisfy the power constraint $E[w(X, S)] \leq P_X$, with $w(\cdot, \cdot)$ being the cost measure. The capacity is given by [31]

$$C^* = \max_{p(u,x|s)} [I(U; Y) - I(U; S)],$$

where U is an auxiliary random variable such that $Y \rightarrow (X, S) \rightarrow U$ and $Y \rightarrow$

$(U, S) \to X$ and $E[w(X, S)] \leq P_X$.

Gelfand-Pinsker coding in general suffers capacity loss when compared to channel coding with side information available at both the encoder and the decoder. However, when Z is $N(0, P_Z)$, we have the famous dirty-paper problem [30] without capacity loss, i.e.,

$$C^* = \frac{1}{2} \log_2(1 + \frac{P_X}{P_Z}). \tag{1.2}$$

Note that the influence of the side information S is completely cancelled, and thus, the capacity is the same as if S were available at the decoder as well. And we make no assumption about S.

From an information-theoretical perspective, according to [32], there are granular gain and boundary gain in source coding, and coding gain and shaping gain in channel coding. Dirty-paper coding is primarily a channel coding problem (for transmitting messages), one should consider the shaping gain and the coding gain. In addition, the side information necessitates source coding (e.g., via a *message-based binning scheme* [33]) to satisfy the power constraint, i.e., the constellation needs to be infinitely replicated so that one can quantize the side information to satisfy the power constraint. However, source coding in dirty-paper coding is not conventional because there is only granular gain, but no boundary gain. One needs to establish the equivalence between the shaping gain in channel coding and the granular gain in source coding (e.g., via a nested lattice code [34]) for dirty-paper coding. Then one can shoot for the shaping gain via source coding and the coding gain via channel coding, i.e., **dirty-paper code design is a source-channel code design problem**. In practice, the former should be done with quantizers (e.g., trellis-coded quantization (TCQ) [35]) having almost spherical Voronoi regions in a high-dimensional Euclidean space, and the latter with near-capacity channel codes (e.g., turbo [36] and low-density parity-check

(LDPC) [37, 38] codes).

Driven by applications in data hiding [39] and precoding for inter-symbol interference channels [40] and ignited by recent discovery of its important role in broadcast coding [41, 42], dirty-paper code design has become one of the hottest research topics [43, 44, 45, 46, 47, 48]. Although Costa's proof shows the existence of a capacity achieving random binning scheme, it does not give any indication about practical code construction. As discussed in the above paragraph, a message-based binning scheme [33] is needed for practical dirty-paper code design. One convenient way to illustrate algebraic binning is through a nested lattice code. Zamir *et al.* [34] showed that a nested lattice scheme can approach the capacity as the dimensionality of the employed lattices goes to infinity. However, nested lattice coding calls for a joint source-channel code design with the same dimensional coarse/source and fine/channel lattice codes, which are not easy to implement in high dimensions. Thus in joint source-channel code design for dirty-paper coding, one needs to match the employed source and channel codes in terms of having equal lattice dimensions.

Chou *et al.* [43, 44] proposed a trellis-based construction which applies TCQ [35] to achieve the high-dimensional lattice quantization in source coding and uses turbo trellis-coded modulation (TTCM) [49] as the powerful channel code. However, TCQ works in a sub-optimal way when combined with TTCM because of the lattice-dimensional mismatch between them. Indeed, at an embedding rate of 1 bit/sample, this scheme performs 2.0dB away from the capacity [44].

At low rates or equivalently, low signal-to-noise ratios, the dirty-paper code design problem is more challenging. Recently, Erez and ten Brink [47] proposed a coding scheme within the framework of nested lattice quantization based on lattice precoding and trellis shaping [46, 50, 51]. The main advantage of this scheme is the separation of the source coding component and the channel coding component, which enables the

employment of the most powerful source and channel codes that are of different lattice dimensions. The code design in [47] based on irregular repeat-accumulate (IRA) [52, 53, 54] codes performs only 1.3dB from the capacity limit at a low rate of 0.25 bit/sample, which is the best result reported so far. Another practical scheme for the dirty-paper problem was reported by Bennatan *et al.* in [48]. This scheme applies superposition coding [55] and the source and channel codes are designed separately. The design in [48] based on LDPC code achieves the same performance as in [47] (e.g., 1.3dB away from the capacity at 0.25 bit/sample).

1.   Main Contributions

In this dissertation, we propose a source-channel coding approach to dirty-paper coding. In addition to channel coding, source coding is employed to satisfy the power constraint due to the presence of encoder side information. The basic element of CCSI is *binning*. Following the guideline in terms of source-channel coding for algebraic binning, we present two practical code designs as follows.

1. **Nested turbo codes**: We address practical dirty-paper code design based on nested lattice codes and propose a nested turbo construction using soft-output TCQ (SOTCQ) for source coding and TTCM [49] for channel coding. A novel procedure is devised to obtain an optimal tradeoff between the source and channel coding performance via balancing the dimensionalities of the equivalent lattice codes corresponding to SOTCQ and TTCM. Our nested turbo code approach performs well at both moderate and high embedding rate regime, e.g., ≥ 1.0 bit/sample.

2. **Dirty-paper code design based on TCQ and IRA codes**: Targeting the more challenging low rate regime, we propose practical code designs using TCQ

[35], in conjunction with both non-systematic and systematic IRA codes [52] and point out that the latter offers additional flexibility in allowing more design options for the systematic part, leading to better performance within the same complexity constraint. At low embedding rates, e.g., 0.25 and 0.5 bit/sample, our design provides the best result to approach the theoretical limit of dirty-paper coding.

C.   Organization of the Dissertation

This dissertation is organized as follows.

In Chapter II, the progressive image transmission over STC-OFDM systems will be discussed with the assumption of coherent detection at receivers and a new broadband MIMO fading model. Its efficiency is confirmed by both our performance evaluation and the simulation results. Based on this image transmission system, the proposal of the adaptive modulation scheme is also studied here.

In Chapter III, a more practical scenario for robust image transmission will be considered. We apply the low-complexity decision-feedback differential-detection receiver for exploiting transmit diversity while not requiring the CSI at the receiver in STC-OFDM systems. Then we justify the employment of the product code as a more powerful JSCC scheme to combat bursty errors in fading channels. Finally, we make a connection between this product code structure and multiple description (MD) coding, and thus propose a new iterative decoding technique for differentially space-time coded MDs of images.

Chapter IV of this dissertation will cover the practical code designs for the dirty-paper problem. By introducing the source-channel coding approach to dirty-paper coding, we show the total gap to capacity limit can be separated into modulo loss

due to source coding and packing loss due to channel coding. Then following the code design guideline to apply both strong source and channel codes so that the total loss is minimized, we present two independent dirty-paper code designs which favor different embedding rate regimes. The nested turbo code construction works well in high or moderate rate region ($\geq$1.0 bit/sample), while the code design based on TCQ and IRA codes provide the best performance so far at low rates ($<$1.0 bit/sample).

Finally in Chapter V, we will summarize this dissertation and provide concluding remarks.

CHAPTER II

PROGRESSIVE IMAGE TRANSMISSION OVER STC-OFDM-BASED MIMO
SYSTEMS WITH ADAPTIVE MODULATION

A.   Introduction

In this chapter, we combine JSCC with STC-OFDM systems for progressive image transmission. For JSCC, the channel coder with RCPC/CRC is applied because of its capability to handle bad channels with quite high BER (e.g., $10^{-3} \sim 10^{-1}$). Contrary to using EEP as done in [56], we employ UEP as called for by the sequential dependencies induced by the embedded source bitstream. We focus on the performance evaluation of the image transmission system and introduce **adaptive modulation** as an additional mechanism for optimizing system performance.

We first evaluate the STC-OFDM system based on a **newly built broadband MIMO fading model**, which is parameterized by the various parameters of the physical environment such as delay spread, cluster angle spread, antenna spacing, and Doppler shift [57, 58, 59]. When compared to the traditional flat fading or frequency-selective fading model, our new fading channels have both time-domain fading correlation due to Doppler shift and spatial-domain fading correlation among different receive antennas induced by those environmental parameters. To simplify the analysis, we study the case with only two transmit antennas and two receive antennas and assume that the receiver has perfect channel state information for coherent detection. A close-form expression of BER is derived for the STC-OFDM-based MIMO system with M-PSK modulation. Both the time-domain and the spatial-domain fading correlation are taken into account in our derivations and their effects on the system performance are comprehensively studied. Regarding to the time-varying character-

istics of fading channels, we show that the interferences within single sub-carrier and from other sub-carriers will result in error floors at high SNRs. However, in the low SNR range, where our interest lies, the error floor is much less pronounced. In addition, when the normalized maximum Doppler frequency is small (e.g., when the mobile receiver is moving at a low speed), the small error floor can be ignored.

Effective JSCC design requires two sets of parameters as inputs: the operational rate-distortion (R-D) function of the image coder and the probabilities of decoding error in packets protected by various RCPC rates for a given BER of the STC-OFDM-based MIMO system. The operational R-D function of embedded coders (e.g., SPIHT [3]) can be generated by encoding the original image once and decoding the bitstream at different lower rates. However, the probability of packet decoding error can not be evaluated accurately by analytical methods. To get around this problem, we realize that most UEP algorithms [5, 6, 7] are designed for BSCs, we thus assume a BSC whose crossover probability is the average BER of our STC-OFDM-based MIMO system. Then for a given average BER, we compute the probabilities of packet decoding error for various channel code rates via Monte Carlo simulations. In practical image transmissions, due to the bursty nature of errors in fading channels, we employ bit interleaving to validate the BSC assumption (with uniformly distributed bit errors) via a random interleaver, as suggested in [9].

Given the image coder (hence the operational R-D function) and the average BER of STC-OFDM-based MIMO system with a certain constellation size M (hence the probabilities of packet decoding error), a UEP scheme can be determined by the fast local search algorithm in [6], resulting the best tradeoff between source coding and channel coding for a fixed transmission rate under a fixed channel condition (BER). From the exact assignment of source bits in the UEP solution, we can compute the best achievable average MSE from the operational R-D function and formulate an

end-to-end performance measure of the image transmission system for a given M. This prompts us to propose an adaptive modulation scheme [60] to tradeoff channel condition and throughput (constellation size). To motivate adaptive modulation, we note that state-of-the-art JSCC (e.g., [56]) can be designed for channels with average BER as high as 10^{-1}. Thus we can potentially achieve high throughput by relying on JSCC to handle bad channel conditions. Specifically, when the SNR increases to a point that almost all source bits can be received correctly without channel coding, we switch to a higher M to gain more transmitted bits and enlist JSCC to help mitigate the effect of increased BER. As a result, based on the performance of the image transmission system for various M, we pick the M that offers the best image quality for each average SNR.

We provide simulation results, which are generated by averaging the MSEs of practical image transmissions before converting the average MSE into peak signal-to-noise ratio (PSNR). We assume that the UEP scheme has been obtained via the system evaluation as discussed above. We also assume that a random bit interleaver is performed over all packets corresponding to the whole image. Our simulation results are in good agreement with our expectation, corroborating the performance derivation of the image transmission system and the proposed adaptive modulation scheme.

This chapter is organized as follows. We will first review the required background knowledge on progressive image coder, STC, OFDM, and JSCC with its fast local search algorithm. In Section C, we introduce the STC-OFDM-based MIMO system based on the new MIMO fading model and evaluate its BER performance. In Section D, we examine JSCC of image transmission over the STC-OFDM-based MIMO system and propose an adaptive modulation scheme. In Section E, we present numerical results, and in Section F, we conclude this chapter and suggest the future work.

B.   Background

1.   Embedded Image Coding

A popular image coding techniques featuring progressive transmission is the SPIHT algorithm [3], which is the enhanced version of the Embedded Zerotree Wavelet (EZW) coding [61]. A coding algorithm producing an embedded code has the property that the bits in the bit stream are generated in order of importance, so that all the low rate codes are included at the beginning of the bit stream. Typically, the encoding process stops when the target bit rate is met. Similarly, the decoder can interrupt the decoding process at any point in the bit stream, and still reconstruct the image. Therefore, a compression scheme generating an embedded code can start sending over the network the coarser version of the image first, and continues with the progressive transmission of the refinement details.

Besides its embedded feature and low complexity, the SPIHT coder outperforms most other coders [62]. The efficiency of SPIHT arises from exploiting the properties of the wavelet coefficients and from the efficient use of data models and conditional entropy coding. One property is that subbands of similar orientation are correlated across different scales. A simple, yet general model that describes the distribution of the wavelet coefficients is based on the zerotree assumption, which assumes that, if a wavelet coefficient at a certain scale is insignificant with respect to a given threshold, then all the coefficients of the same orientation in the same spatial location at finer scales are also insignificant with respect to the threshold.

With the rapid progress of wavelet-based image coding, the new JEPG2000 image coding standard also includes the wavelet transform and applies the embedded block coding with optimal truncation (EBCOT) [63] algorithm for bit-plane coding the wavelet coefficients. Unlike SPIHT which employs the arithmetic coding [64] on the

significant bits only, the arithmetic coding in EBCOT is also applied on the sign bits and the refinement bits. Furthermore, since EBCOT breaks one bit-plane into three fractional bit-planes and compresses them in a decreasing order of R-D importance, the complexity of JPEG2000 coding is higher than that of SPIHT coding. In terms of compression efficiency, JPEG2000 performs comparably to SPIHT. The strength of the JPEG2000 standard lies in its rich set of features such as lossy and lossless compression, scalability in rate and image resolution, region of interest (ROI) coding, and error resilience.

In this dissertation, our focus is the proposal of the adaptive modulation based on the performance evaluation of the progressive image transmission scheme over STC-OFDM-based MIMO systems. In fact any embedded image coder can be applied in our setup. Finally, we select the SPIHT codec due to its high efficiency and low complexity.

2.   STC-OFDM Systems

Consider an STC-OFDM communication system with K sub-carriers, N_T transmit antennas and N_R receive antennas as shown in Fig. 3.

Firstly the information bits are modulated by an M-PSK modulator and grouped into OFDM codewords of length K through a serial to parallel converter. Then they are encoded by an STC encoder. Each STC codeword consists of (PN_T) symbols, which are transmitted from N_T transmit antennas and across P consecutive OFDM slots at a particular OFDM sub-carrier. Let $x_j[p, k]$ denote the output of an STC encoder at the pth OFDM word associated with the k-th sub-carrier and the jth transmit antenna, where $p = 1, \ldots, P; k = 0, \ldots, K - 1; j = 1, \ldots, N_T$. They are actually the transmitted symbols in frequency domain. By IDFT and adding proper cyclic prefixes, we obtain the transmitted symbols in time domain. Then these symbols are

Transimitter
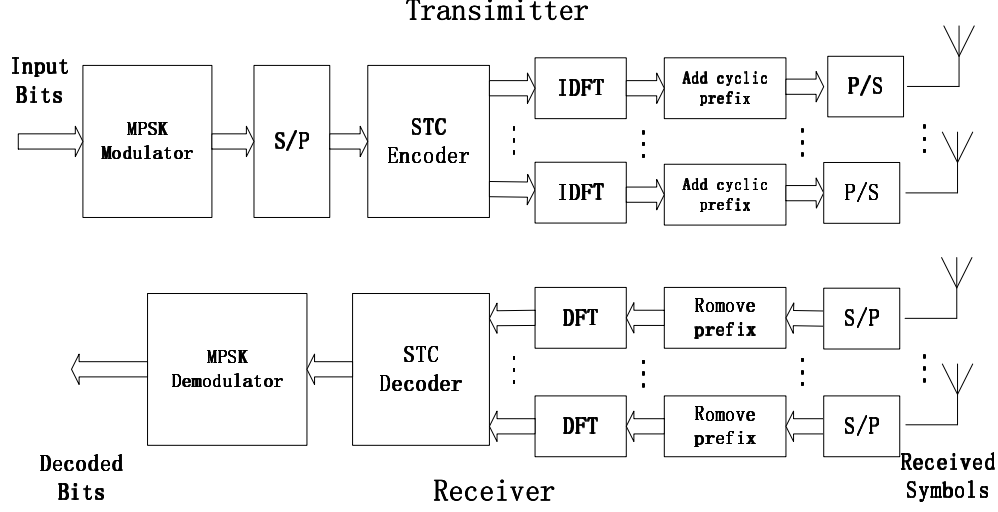
Fig. 3. Block diagram of STC-OFDM system.

transmitted serially from the K sub-carriers of each transmit antenna.

In OFDM systems, we assume the frequency-selective fading channel. Consider the channel response between the j-th transmit antenna and the i-th receive antenna, which is given by [65]

$$h_{i,j}(\tau; t) = \sum_{l=0}^{L-1} \alpha_{i,j}(l; t) \delta\left(\tau - \frac{l}{\triangle_f}\right), \qquad (2.1)$$

where $\delta(\cdot)$ is the Kronecker delta function; $L \triangleq \lceil \tau_m \Delta_f + 1 \rceil$ denotes the maximum number of resolvable taps, with τ_m being the maximum multi-path spread and Δ_f the tone spacing of the OFDM system; $\alpha_{i,j}(l; t)$ is the complex amplitude of the l-th tap, whose delay is $l/\triangle_f$. Each of them is independent of the other taps and has the same normalized correlation function but its own average power $\sigma_{i,j,l}^2, l = 0, 1, \ldots, L-1$. Assume Jakes' fading channel model [66] with

$$R_{\alpha_{i,j}}(l; t) = \sigma_{i,j,l}^2 J_0(2\pi f_D t), \ l = 0, 1, \ldots, L-1, \qquad (2.2)$$

where $J_0(\cdot)$ is the 0-th order Bessel function of the first kind; f_D is the Doppler

frequency.

For OFDM systems with proper cyclic extension, sample timing and tolerable leakage, the channel frequency response between the j-th transmit antenna and the i-th receive antenna at the p-th OFDM word and at the k-th subcarrier can be expressed as

$$H_{i,j}[p,k] \;=\; \sum_{l=0}^{L-1} h_{i,j}[l;p]e^{-j2\pi kl/K} \;\; \text{with} \;\; h_{i,j}[l;p] \triangleq \alpha_{i,j}(l;pT_s), \qquad (2.3)$$

where T_s is the duration of one OFDM word. Note that we assume that each tap of fading process remains static during each OFDM word but it varies from one OFDM word to another.

At the receivers, the received symbols first go through the serial to parallel converters. After removing the cyclic prefixes and applying DFT on the time-domain received symbols, we obtain the frequency-domain received symbols as

$$\boldsymbol{y}_i[p] \;=\; \boldsymbol{X}[p]\,\boldsymbol{W}\boldsymbol{h}_i[p] + \boldsymbol{z}_i[p], \qquad i=1,\ldots,N_R, \;\; p=1,\ldots,P, \;\; (2.4)$$

$$\text{with} \quad \boldsymbol{X}[p] \;\triangleq\; [\boldsymbol{X}_1[p],\ldots,\boldsymbol{X}_{N_T}[p]]_{K\times(N_TK)},$$

$$\boldsymbol{X}_j[p] \;\triangleq\; \text{diag}\,\{x_j[p,1],\ldots,x_j[p,K]\}_{K\times K},$$

$$\boldsymbol{W} \;\triangleq\; \text{diag}\,\{\boldsymbol{W}_f,\ldots,\boldsymbol{W}_f\}_{(N_TK)\times(N_TL)},$$

$$\boldsymbol{W}_f \;\triangleq\; [\boldsymbol{w}_f(0),\boldsymbol{w}_f(1),\ldots,\boldsymbol{w}_f(K-1)]^{\text{H}}_{K\times L},$$

$$\boldsymbol{w}_f(k) \;\triangleq\; \left[1,e^{-j2\pi k/K},\ldots,e^{-j2\pi k(L-1)/K}\right]^{\text{H}},$$

$$\boldsymbol{h}_i[p] \;\triangleq\; \left[\boldsymbol{h}^{\text{H}}_{i,1}(p),\ldots,\boldsymbol{h}^{\text{H}}_{i,N_T}(p)\right]^{\text{H}}_{(N_TL)\times 1},$$

$$\boldsymbol{h}_{i,j}[p] \;\triangleq\; [h_{i,j}[0,p],\ldots,h_{i,j}[L-1,p]]^{T}_{L\times 1},$$

where $\boldsymbol{h}_i[p]$ is the (N_TL)-dimension vector containing the complex channel frequency responses between the i-th receive antenna and all N_T transmit antennas at the

p-th OFDM word; $x_j[p, k]$ is the STC symbol transmitted from the j-th transmit antenna at the k-th sub-carrier and at the p-th OFDM word; $\boldsymbol{y}_i[p]$ is the K-dimension vector of received signals from the i-th receive antenna at the k-th sub-carrier and at the p-th time slot; $\boldsymbol{z}_i[p]$ is the additional white Gaussian noise (AWGN), which is complex Gaussian with covariance matrix $\sigma_z^2 \boldsymbol{I}$. In our work, we apply M-PSK signal constellation, i.e., $x_j[p, k] \in \mathcal{A} \triangleq \{\frac{1}{\sqrt{N_T}} e^{j\frac{2\pi k}{M}}, k = 0, 1, \ldots, M - 1\}$, where the factor $\frac{1}{\sqrt{N_T}}$ is used to normalize the energy of the transmitted signals.

The space-time code was introduced systematically in [16]. Following [16], the space-time code is defined by a $(P \times N_T)$ matrix $\mathcal{G}$. Each row of $\mathcal{G}$ is a permuted and transformed (i.e., negated and/or conjugated) version of the N_T-dimensional vector of complex data symbols $\boldsymbol{x}$. In the simplest case with $P = 2, N_T = 2$, we get the Alamouti code [14]

$$\mathcal{G}_2 = \begin{bmatrix} x_1 & x_2 \\ -x_2^* & x_1^* \end{bmatrix}. \tag{2.5}$$

The data vector is defined as $\boldsymbol{x} = [x_1, x_2]$. At the first time slot, the symbols on the 1st row $[x_1, x_2]$ are transmitted simultaneously from transmit antenna 1 and 2, respectively. At the 2nd time slot, the symbols on the second row $[-x_2^*, x_1^*]$ are transmitted simultaneously from the two transmit antennas. And note that the code matrix is orthogonal to allow a simple decoding scheme.

It is possible to simplify the system by also assuming that the fading process remains static during one STC codeword (i.e., the channel time responses $\boldsymbol{h}_i[p], p = 1, \ldots, P$, remain constant during each P consecutive OFDM slots). Then the system

model in (2.4) can be modified as

$$\underline{\boldsymbol{y}}_i \;=\; \underline{\boldsymbol{X}}\,\boldsymbol{W}\,\boldsymbol{h}_i + \underline{\boldsymbol{z}}_i, \quad i = 1, \ldots, N_R, \tag{2.6}$$

$$\text{with } \underline{\boldsymbol{y}}_i \;=\; \left[\boldsymbol{y}_i^{\mathrm{H}}[1], \ldots, \boldsymbol{y}_i^{\mathrm{H}}[P]\right]^{\mathrm{H}}_{(PK)\times 1}, \quad \underline{\boldsymbol{X}} \triangleq \left[\boldsymbol{X}^{\mathrm{H}}[1], \ldots, \boldsymbol{X}^{\mathrm{H}}[P]\right]^{\mathrm{H}}_{(PK)\times(N_T K)},$$

$$\underline{\boldsymbol{z}}_i \;\triangleq\; \left[\boldsymbol{z}_i^{\mathrm{H}}[1], \ldots, \boldsymbol{z}_i^{\mathrm{H}}[P]\right]^{\mathrm{H}}_{(PK)\times 1}, \quad \boldsymbol{h}_i \triangleq \boldsymbol{h}_i[1] = \boldsymbol{h}_i[2] = \ldots = \boldsymbol{h}_i[P].$$

According to the above definitions, we have

$$\boldsymbol{W}^{\mathrm{H}}\underline{\boldsymbol{X}}^{\mathrm{H}}\underline{\boldsymbol{X}}\,\boldsymbol{W} \;=\; \boldsymbol{W}^{\mathrm{H}}\left(\sum_{p=1}^{P} \boldsymbol{X}^{\mathrm{H}}[p]\boldsymbol{X}[p]\right)\boldsymbol{W}$$

$$=\; \boldsymbol{W}^{\mathrm{H}}\left(\frac{P}{N_T}\boldsymbol{I}\right)\boldsymbol{W} = \left(\frac{PK}{N_T}\right)\cdot\boldsymbol{I} \tag{2.7}$$

Note that (2.6) and (2.7) are key equations to design the detection schemes for the STC-OFDM system.

a. Coherent Detection for STC-OFDM Systems

Assuming perfect channel state information is available at the receiver for coherent detection, based on (2.6), the decision rule can be expressed as

$$\hat{\underline{\boldsymbol{X}}} \;=\; \arg\min_{\underline{\boldsymbol{X}}} \sum_{i=1}^{N_R} \left\|\underline{\boldsymbol{y}}_i - \underline{\boldsymbol{X}}\,\boldsymbol{W}\,\boldsymbol{h}_i\right\|^2$$

$$=\; \sum_{k=0}^{K-1} \arg\min_{\{\boldsymbol{x}[p,k]\}_p} \left[\sum_{i=1}^{N_R}\sum_{p=1}^{P} \left|y_i[p,k] - \boldsymbol{x}^{\mathrm{H}}[p,k]\,\boldsymbol{W}'_f(k)\boldsymbol{h}_i[p]\right|^2\right] \tag{2.8}$$

$$\text{with } \boldsymbol{x}[p,k] \;\triangleq\; \left[x_1[p,k], \ldots, x_{N_T}[p,k]\right]^{\mathrm{H}}_{N_T\times 1},$$

$$\boldsymbol{W}'_f(k) \;\triangleq\; \mathrm{diag}\left[\boldsymbol{w}_f^{\mathrm{H}}(k), \ldots, \boldsymbol{w}_f^{\mathrm{H}}(k)\right]_{N_T\times(N_T L)},$$

where $\hat{\underline{\boldsymbol{X}}}$ denotes the decisions of data symbols. All other notations follow the definitions in (2.4)$\frown$(2.6).

From (2.8) we can see that the decision rule can be broken into K independent minimization problems since the K sub-carriers can be considered separably.

And each minimization problem is solved by enumerating over all possible $\boldsymbol{x}[p,k] \in \mathcal{A}^{N_T}, p = 1, \ldots, P$. According to the coding constraints of STC as defined in (2.5), $\boldsymbol{x}[p,k], p = 1, \ldots, P$, should be different permutations and/or transformations of $\boldsymbol{x}[1,k]$.

3.   JSCC for Progressive Image Transmission

JSCC design is the main component of our image transmission system. As shown in Fig. 4, the channel encoder transforms the source bitstream into N_P packets with the same lengthes L_P but their own code rates $r_{k_i}, i = 1, 2, \ldots, N_P$. Given m channel codes $c_1, \ldots, c_m$, let $\mathcal{R}$ be the set of corresponding code rates $r_1 < r_2 < \cdots < r_m$. For $i = 1, \ldots, m$, let $p(r_i)$ denote the probability of a decoding error in a packet protected by code c_i. Then an N_P-packet error protection scheme (EPS) $R = (r_{k_1}, \ldots, r_{k_{N_P}}) \in \mathcal{R}^{N_P}$ assigns to each packet $i, i = 1, \ldots, N_P$, a channel code rate $r_{k_i} \in \mathcal{R}$. The optimization problem is to determine R to achieve the best reconstructed image quality in some criteria. More details are discussed in the following sections.
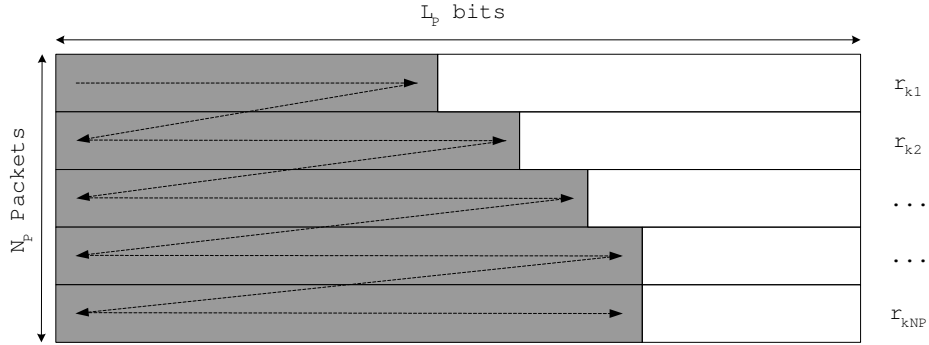
Fig. 4. Structure of packets for image transmission with UEP. The shaded stripes denote the embedded source bitstream which flows along the direction of the dashed line, while the blank ones denote the RCPC/CRC parity bits corresponding to the code rates r_{k_i} of the packets.

Two criteria are usually considered: rate-optimal (RO) solution and distortion-optimal (DO) solution.

The RO solution maximizes the expected number of correctly-received source bits, i.e.,

$$\mathrm{E}_{N_P}[r](R) = \sum_{i=0}^{N_P} P_i(R)V_i(R), \tag{2.9}$$

where $V_0(R) = 0$ and for $i \geq 1$, $V_i(R) = \sum_{j=1}^{i} \upsilon(r_{k_j})$ with $\upsilon(r_{k_j}) = L_P r_{k_j}$ being the number of source bits in the j-th packet. For $i = 1, \ldots, N_P - 1$, $P_i(R) = \prod_{j=1}^{i}(1 - p(r_{k_j}))p(r_{k_{i+1}})$ is the probability that no errors occur in the first i packets but with an error in the next one, $P_0(R) = p(r_{k_1})$ is the probability of an error in the first packet, and $P_{N_P}(R) = \prod_{j=1}^{N_P}(1 - p(r_{k_j}))$ is the probability that all N_P packets are correctly received.

The DO solution minimizes the expected MSE of the reconstructed image, i.e.,

$$\mathrm{E}_{N_P}[D](R) = \sum_{i=0}^{N_P} P_i(R)D_i(R), \tag{2.10}$$

where $D_0(R) = D_0$ is a constant, and for $i \geq 1$, $D_i(R)$ is the reconstruction MSE using the first i packets. The probability that no errors occur in the first i packets, $P_i(R), i = 0, \ldots, N_P$, has been defined above in the case of RO solution.

The optimal EPS can be computed by enumerating all possible N_P-packet EPS's and selecting the best one. It is prohibitively time consuming when many code rates are allowed. Thus fast algorithms are necessary for the JSCC design.

One fast algorithm for RO solution was introduced by Stanković *et al.* In [7]. The idea is to determine a trivial 1-packet RO EPS at first and to complete N_P-packet solution repetitively since it is easy to derive a i-packet RO EPS from a $(i-1)$-packet

RO EPS. Details of this algorithm are in [7].

In a subsequent work [6], Hamzaoui *et al.* presented a local search algorithm to solve the DO problem by iterative improvement. Starting with the fast computation of an RO solution to (2.9), a quick local search can be performed among the neighbors of the RO EPS to reach an approximation of a DO solution to (2.10). The neighbor is defined as one EPS that differs from the current EPS in only one code rate but provide stronger protection. If a candidate in the neighborhood is better than the current EPS, we adopt it and repeat the local search from this new solution. Otherwise, we stop. Details of this local search algorithm are given in [6].

RO solution is shown to be a good approximation of DO solution in [6]. And the RO EPS is independent of both the image and the source coder. Thus the EPS information is not required in the overhead since the UEP design can be repeated at the receiver side. Furthermore, the RO solution is progressive, i.e., if an RO EPS for a target transmission rate is determined, then the RO EPS for all lower transmission rates can be obtained easily without repeating the optimization. If we allow a certain extent of degradation in reconstructed image quality, RO solution is a substitution for DO solution, as the work in [9].

In this chapter, we focus on the best performance of the image transmission system. Thus DO solution is studied and its EPS design is computed by using the fast local search algorithm in [6].

C. STC-OFDM Systems with a New Broadband MIMO Fading Model

1. Broadband MIMO Fading Channel Model

We first introduce a newly built broadband MIMO fading model parameterized by the various parameters of the physical environment such as delay spread, cluster angle

spread, antenna spacing, and Doppler frequency. The resulting channels will have both time-domain fading correlation due to Doppler frequency and spatial-domain fading correlation induced by those environmental parameters. Our channel model is based on the previous works reported in [57, 58, 59].
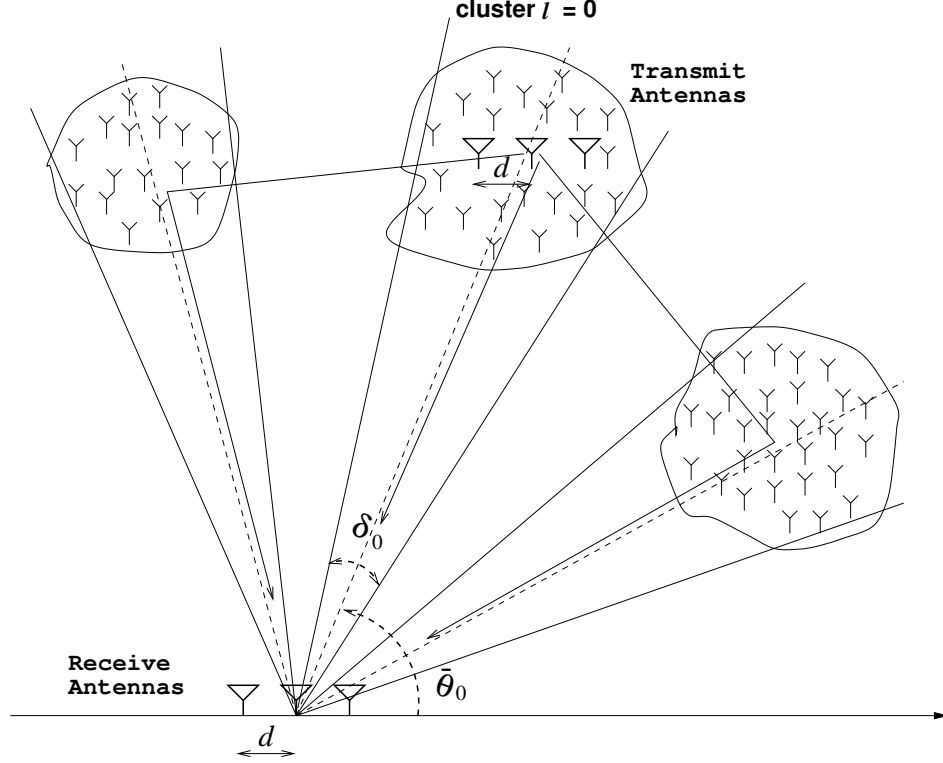
Fig. 5. Schematic representation of the broadband MIMO fading channel composed of multiple clustered paths. Each cluster has a mean angle of arrival $\bar{\theta}_l$ and an angle spread δ_l. The absolute antenna spacing is denoted by d.

We assume that the transmit antennas are surrounded by scatterers in the vicinity so that fading at the transmitter end is spatially uncorrelated. We also assume the receive antennas at the base station are placed high above the ground level so that the scattering in the vicinity area can be ignored, which implies correlation of spatial fading at the receiver end. For the sake of simplicity, no line of sight (LOS) is assumed between the mobile and the receiving array. We model the delay spread

by assuming that there are L significant scatterer clusters, which correspond to L resolvable paths, as pictured in Fig. 5, and each of the paths from the same scatterer cluster experiences the same delay. Each scatterer cluster has a mean angle of arrival at the receive antenna denoted as $\bar{\theta}_l$, a cluster angle spread δ_l, and a path gain σ_l^2. We also assume a uniform linear array (ULA) at both the transmitter and receiver with identical antenna elements. The relative antenna spacing is denoted as $\Delta = d/\lambda$, where d is the absolute antenna spacing and λ is the wavelength of the transmitted narrow-band signal.

We consider a MIMO communication system with N_T transmit antennas and N_R receive antennas. Let the $(N_R N_T) \times 1$ vector $\boldsymbol{h}_l$ represents the l-th tap of the discrete-time MIMO fading channel impulse response. Suppose different scatter clusters are uncorrelated, i.e., $\mathrm{E}\left\{\boldsymbol{h}_l \boldsymbol{h}_{l'}^H\right\} = \boldsymbol{0}_{(N_R N_T \times N_R N_T)}$, for $l \neq l'$, where $\boldsymbol{h}_l \triangleq \left[\boldsymbol{h}_0^{l\,T}, \boldsymbol{h}_1^{l\,T}, \ldots, \boldsymbol{h}_{N_T-1}^{l\quad T}\right]_{(N_R N_T \times 1)}^T$ with $\boldsymbol{h}_i^l \triangleq \left[h_{i,0}^l, h_{i,1}^l, \ldots, \ h_{i,N_R-1}^l\right]_{(N_R \times 1)}^T$, $h_{i,j}^l$ denotes the time-domain fading coefficient of the l-th tap associated with the i-th transmit antenna and the j-th receive antenna.

We assume that the $\boldsymbol{h}_i^l$'s $(l = 0, 1, \ldots, L-1; i = 0, 1, \ldots, N_T-1)$ are all vectors of zero-mean complex Gaussian random variables and the $N_R \times N_R$ correlation matrix $\boldsymbol{R}_l = \mathrm{E}\left\{\boldsymbol{h}_i^l \boldsymbol{h}_i^{l\,H}\right\}$ is independent of the index i, i.e., the fading statistics are the same for all transmit antennas. According to [57], we can write the spatial-domain correlation matrix $\boldsymbol{R}_l$ as

$$[\boldsymbol{R}_l]_{j,j'} \triangleq \mathrm{E}\left\{h_{i,j}^l (h_{i,j'}^l)^*\right\} = \sigma_l^2 \rho_l \left((j - j')\Delta, \ \bar{\theta}_l, \ \sigma_{\theta_l}\right), \quad l = 0, 1, \ldots, L-1. \quad (2.11)$$

We next assume that the angle of arrival for the l-th path cluster θ_l is Gaussian distributed, i.e., $\theta_l \sim \mathcal{N}(\bar{\theta}_l, \ \sigma_{\theta_l}^2)$. The variance $\sigma_{\theta_l}^2$ is proportional to the angular spread δ_l. It is shown in [58] that the correlation function can be approximated for

small angle spread as

$$\rho_l(p\Delta, \ \bar{\theta}_l, \ \sigma_{\theta_l}) \approx \exp\{-j2\pi p\Delta \cos(\bar{\theta}_l) - \frac{1}{2}[2\pi p\Delta \sin(\bar{\theta}_l)\sigma_{\theta_l}]^2\}. \qquad (2.12)$$

When exploiting the time-domain fading correlation due to the Doppler frequency, we assume a Jake's model [66] as

$$R_h(m) = \mathrm{E}\left\{h_{i,j}^l[n](h_{i,j}^l[n+m])^*\right\} = \sigma_l^2 J_0(2\pi f_D mT) \qquad (2.13)$$

where $h_{i,j}^l[n]$ corresponds to the fading coefficient at the n-th time slot; $J_0(\cdot)$ is the 0-th order Bessel function of the first kind; f_D is the Doppler frequency and T is the duration of the time slot.

2.   Mathematical STC-OFDM-based MIMO System Model

It is simple to fulfill a MIMO system via well-studied STC with multiple receive antennas. Since STC systems are originally designed for flat-fading channels, it is challenging to apply them over multi-path MIMO fading channels. One approach is to employ OFDM techniques, which can transform a multi-path fading channel into many parallel flat fading sub-channels, to combat multi-path delay spread in high-rate wireless systems. In this section, we will provide the STC-OFDM-based MIMO system model and analyze its performance with coherent detection.

For the sake of simplicity, we consider an STC-OFDM-based MIMO system with two transmit antennas and two receive antennas ($N_T = N_R = 2$) and K sub-carriers, signalling through an L-tap MIMO fading channel. Under the assumption that the fading channel coefficients remain constant within the interval of one STC word, namely $P = 2$ consecutive OFDM words, similarly with (2.6), the system model is

given by

$$\underline{Y} = \underline{X}\,\underline{W}_L\,\underline{h} + \underline{Z} \tag{2.14}$$

$$\text{with}\quad \underline{Y} \triangleq \left[\, \boldsymbol{Y}_{0,0}^T,\ \boldsymbol{Y}_{0,1}^T,\ \boldsymbol{Y}_{1,0}^T,\ \boldsymbol{Y}_{1,1}^T \,\right]_{(4K\times 1)}^T,$$

$$\boldsymbol{Y}_{j,p} \triangleq [Y_j(p,0), Y_j(p,1), \ldots, Y_j(p, K-1)]_{(K\times 1)}^T,$$

$$\underline{X} \triangleq \mathrm{diag}\,(\boldsymbol{X}, \boldsymbol{X})_{(4K\times 4K)},\ \boldsymbol{X} \triangleq \begin{pmatrix} \boldsymbol{X}_0 & \boldsymbol{X}_1 \\ -\boldsymbol{X}_1^H & \boldsymbol{X}_0^H \end{pmatrix},$$

$$\boldsymbol{X}_i \triangleq \mathrm{diag}\,(X_i[0], X_i[1], \ldots, X_i[K-1])_{(K\times K)},$$

$$\underline{W}_L \triangleq \mathrm{diag}\,(\boldsymbol{w}_L, \boldsymbol{w}_L, \boldsymbol{w}_L, \boldsymbol{w}_L)_{(4K\times 4L)},$$

$$[\boldsymbol{w}_L]_{r,s} \triangleq e^{-j\frac{2\pi}{K}rs},\ r = 0, \ldots, K-1; s = 0, \ldots, L-1,$$

$$\underline{h} \triangleq \left[\, \boldsymbol{h}_{0,0}^T, \boldsymbol{h}_{1,0}^T, \boldsymbol{h}_{0,1}^T, \boldsymbol{h}_{1,1}^T \,\right]_{(4L\times 1)}^T,$$

$$\boldsymbol{h}_{i,j} \triangleq \left[h_{i,j}^0, h_{i,j}^1, \ldots, h_{i,j}^{L-1} \right]^T,$$

where $Y_j(p,n)$ is the frequency-domain received symbol of the n-th sub-carrier at the p-th time slot and the j-th receive antenna; $X_i[n]$ represents the transmitted symbol of the n-th sub-carrier from the i-th antenna. In our work, we apply M-PSK constellation, i.e., $X_i[n] \in \mathcal{A} \triangleq \left\{ \frac{1}{\sqrt{2}} e^{j\frac{2\pi k}{M}}, k = 0, 1, \ldots, M-1 \right\}$. The factor $1/\sqrt{2}$ is used to normalize the energy of the transmitted symbols since two transmit antennas are considered here; The AWGN vector $\underline{Z}$ contains independent zero-mean complex Gaussian random variables with power σ_z^2.

3. BER performance of STC-OFDM-based MIMO System with Coherent Detection

When the CSI $\underline{\boldsymbol{h}}$ is known to the receiver, ML algorithm can be used as the decoding algorithm for coherent detection, i.e.,

$$\hat{\underline{\boldsymbol{X}}} = \arg\max_{\underline{\boldsymbol{X}}} \ \log p\left(\underline{\boldsymbol{Y}}|\underline{\boldsymbol{X}}\right) = \arg\min_{\underline{\boldsymbol{X}}} \left\| \underline{\boldsymbol{Y}} - \underline{\boldsymbol{X}} \underbrace{\underline{\boldsymbol{W}}_L \underline{\boldsymbol{h}}}_{\underline{\boldsymbol{H}}} \right\|^2, \tag{2.15}$$

where $\underline{\boldsymbol{H}}$ contains the frequency-domain fading coefficients by performing DFT on time-domain $\underline{\boldsymbol{h}}$. We can see that the OFDM technique transforms an L-path fading channel in time domain into K parallel flat-fading sub-channels in frequency domain.

From (2.15) and some detailed derivations in Appendix A, we compute the average BER of the proposed system as

$$P_b \ \cong \ \frac{N_m}{\log_2 M} \cdot \frac{1}{16\rho^3} \Big\{ 8\rho^3 + f(1+\rho)(2-\rho-8\rho^2-5\rho^3) + f(1-\rho)(-2-\rho+8\rho^2-5\rho^3) $$
$$+ f^3(1+\rho)(\rho+2\rho^2+\rho^3) + f^3(1-\rho)(\rho-2\rho^2+\rho^3) \Big\}, \tag{2.16}$$

with

$$N_m = \left\{ \begin{array}{ll} 1, & M = 2 \\ 2, & M > 2 \end{array} \right. , \quad f(\xi) = \sqrt{\frac{\frac{K}{K+G} \cdot \frac{\bar{\gamma}_s}{2} \sin^2 \frac{\pi}{M} \cdot \xi}{\frac{K}{K+G} \cdot \frac{\bar{\gamma}_s}{2} \sin^2 \frac{\pi}{M} \cdot \xi + 1}}, \quad \rho = \left| \frac{\sum_{l=0}^{L-1} \sigma_l^2 \rho_l(\Delta, \bar{\theta}_l, \sigma_{\theta_l})}{\sum_{l=0}^{L-1} \sigma_l^2} \right|,$$

where $\bar{\gamma}_s$ is the average SNR of the MIMO system. $G \geq L - 1$ is the length of guard interval in the OFDM system to remove the inter-symbol interference. Note that (2.16) is an exact close-form expression of BER for BPSK and QPSK. When $M > 4$, it is also a good approximation if Gray mapping is applied.

From (2.16), we see that the spatial fading correlation is induced by ρ, i.e., the norm of correlation coefficient of the fading channels at different receivers.

As introduced in Section 2, the assumption of the constant fading channels within one STC-OFDM codeword is necessary for the receiver design. However, this assump-

tion does not hold since the practical channels are time-varying. One straightforward solution is to take the mean of all fading coefficients during one STC-OFDM codeword as a new common fading coefficient. This modelling mismatch will induce the ICI from other sub-carriers, hence result in an error floor with the increase of SNR. The detailed analysis of the time variance in OFDM systems is discussed in Appendix B.

By regarding the ICIs as additive noise terms, we can still compute the BER performance by (2.16), but with a new function $f(\xi)$ as

$$f(\xi) = \sqrt{\frac{\frac{K}{K+G} \cdot \frac{\bar{\gamma}_s^{\mathrm{TV}}}{2} \sin^2 \frac{\pi}{M} \cdot \xi}{\frac{K}{K+G} \cdot \frac{\bar{\gamma}_s^{\mathrm{TV}}}{2} \sin^2 \frac{\pi}{M} \cdot \xi + 1}}, \tag{2.17}$$

with

$$\bar{\gamma}_s^{\mathrm{TV}} = \frac{\bar{\gamma}_s \cdot \psi(f_D, T, K, G)}{\bar{\gamma}_s \left(1 - \psi(f_D, T, K, G)\right) + 1}, \tag{2.18}$$

$$\psi(f_D, T, K, G) = \frac{1}{2K^2} \sum_{n=0}^{K-1} \sum_{n'=0}^{K-1} \left\{ J_0(2\pi f_D(n - n')T) + J_0(2\pi f_D(n - n' + K + G)T) \right\}.$$

Details of the derivations are given in Appendix B. From (2.18), we see that the temporal fading correlation is also exploited.

Fig. 6 plots the BER performance of the STC-OFDM-based MIMO system with $N_T = 2$ transmit antennas and $N_R = 2$ receive antennas over a $L = 3$-tap fading channel. We assume QPSK modulation and the OFDM system with $K = 128$ sub-carriers and the guard interval of length $G = 4$. Various spatial correlation coefficients $\rho \in [0, 1]$ are considered. Given a data rate of 500 Kbauds/sec, we also select two normalized Doppler shifts $f_D T = 2 \times 10^{-4}$ and 10^{-5} to study the effect of temporal fading correlation.

We see that the BER performance gets worse with the increase of spatial fading correlation coefficient ρ. When $\rho = 0$, it is obviously a usual frequency-selective fading
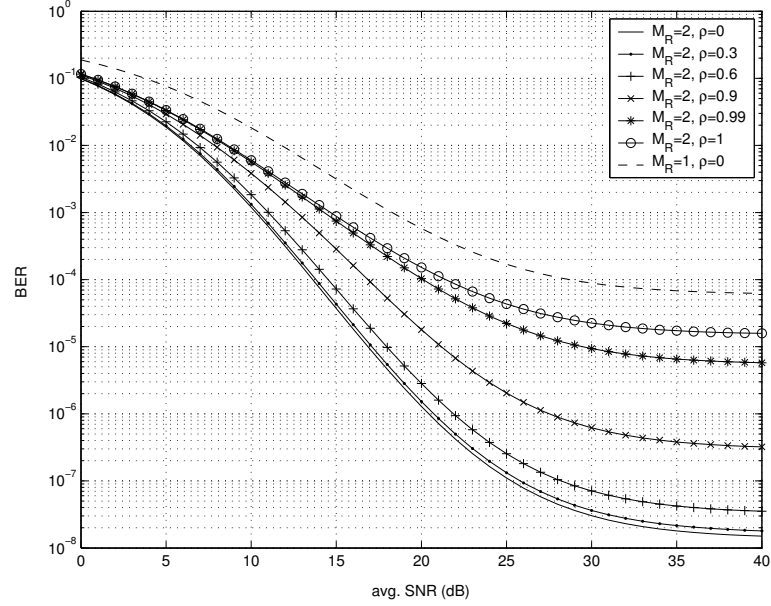
(a) $f_D T = 2 \times 10^{-4}$
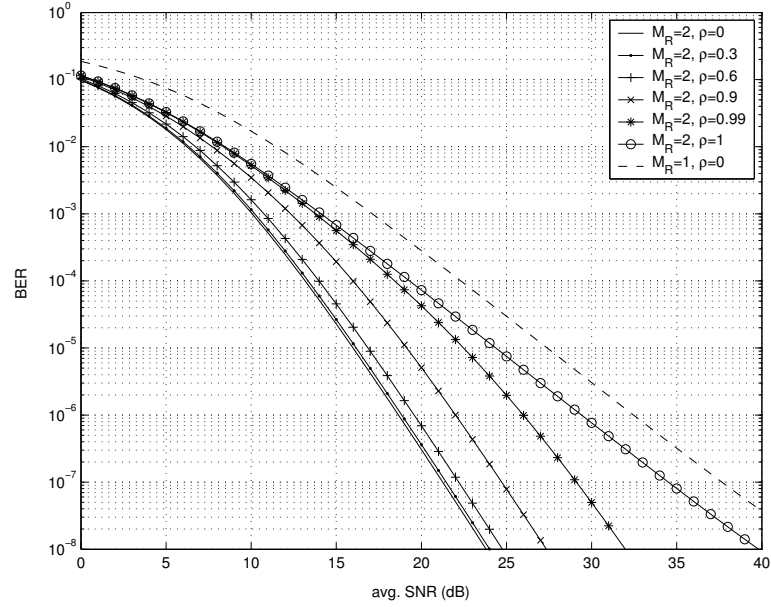
(b) $f_D T = 10^{-5}$

Fig. 6. BER performance of STC-OFDM-based MIMO system with $N_T = 2$ transmit antennas and $N_R = 2$ receive antennas, signaling through an ($L=3$)-tap fading channel. Various spatial correlation coefficients $\rho \in [0, 1]$ and two Doppler frequencies, (a) $f_D T = 2 \times 10^{-4}$; (b) $f_D T = 10^{-5}$, are considered. We assume QPSK modulation and the OFDM system with $K = 128$ sub-carriers and the guard interval of length $G = 4$.

channel. When $\rho = 1$, it reduces to a system with only single receive antenna in the means of diversity, since the symbols from a certain transmit antenna can be viewed to pass through two equal fading channels to the receive antennas. Specifically, this repetitive transmission, working like a repetition code, make the BER performance with $\rho = 1$ be 3 dB better than that of the case with single receive antenna (denoted by dashed lines in Fig. 6). Another observation is that the degradation of BER performance is much more remarkable for large ρ. For example, we only find a 1-dB loss when increasing ρ from 0 to 0.6. But a 2.5-dB gap can be observed between the curves with $\rho = 0.6$ and $\rho = 0.9$.

From the discussion above, the time-varying property of the fading coefficients induces ICI among the sub-carriers within one OFDM codeword, hence results in an error floor in BER performance. As shown in Fig. 6, if $f_D T = 2 \times 10^{-4}$, the error floor occurs when SNR>15dB. If $f_D = 10^{-5}$, the error floor is not pronounced when SNR<40dB. That is, the larger the Dopper frequency f_D, the severer the ICI. And obviously, the error floor goes up with the increase of ρ.

D.   Progressive Image Transmission System with Adaptive Modulation

Fig. 7 gives the block diagram of the image transmission system, which consists of three main functional blocks: progressive image coding, JSCC and STC-OFDM. The image is first fed into the embedded SPIHT image coder. The bitstream is transformed into a sequence of packets by the RCPC/CRC channel encoder. Note that more significant source bits are assigned ahead with stronger protection via UEP. We transmit all the packets through the STC-OFDM-based MIMO system. At the receiver, the received symbols are first decoded by coherent detection. After channel decoding, parity checking is performed via CRC decoding. Whenever an error is

detected, CRC decoding stops. The image decoder then reconstructs the transmitted image using the correctly decoded source bits before the first packet with decoding error.
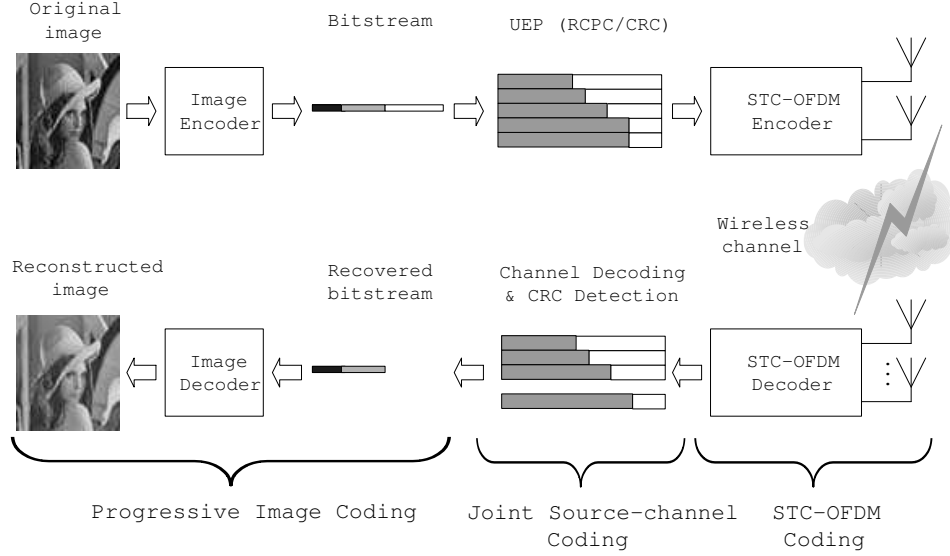
Fig. 7. Overall block of image transmission system over STC-OFDM systems.

As introduced in Section B.3, the DO EPS design in JSCC requires two sets of parameters as inputs: the R-D function $D(r_s)$ of the image coder (where D is the MSE and r_s is the source rate in bits per pixel (bpp)) and the probabilities of packet decoding error $p(r_c)$ for RCPC rate r_c at a given BER P_b by (2.16) and (2.17).

The R-D function $D(r_s)$ is easy to generate by practically encoding and decoding the original image. That is, we encode the image at a given highest source rate and then decode the bitstream at different low rates.

The probability of packet decoding error $p(r_c)$ is difficult to evaluate accurately by analytical methods. Since in our system the RCPC is based on hard-decision viterbi decoding, we assume a straightforward BSC, whose crossover probability is P_b. Given a BER P_b and a channel code rate r_c, we compute the corresponding $p(r_c)$ via Monte Carlo method and store these results in a lookup table for their future

usages. Part of values of $p(r_c)$ are demonstrated in Fig. 8 for the set of RCPC code rates $\mathcal{R} = \{8/9,\ 8/10,\ldots,8/32\}$ and the range of BER $0.01 \sim 0.2$.
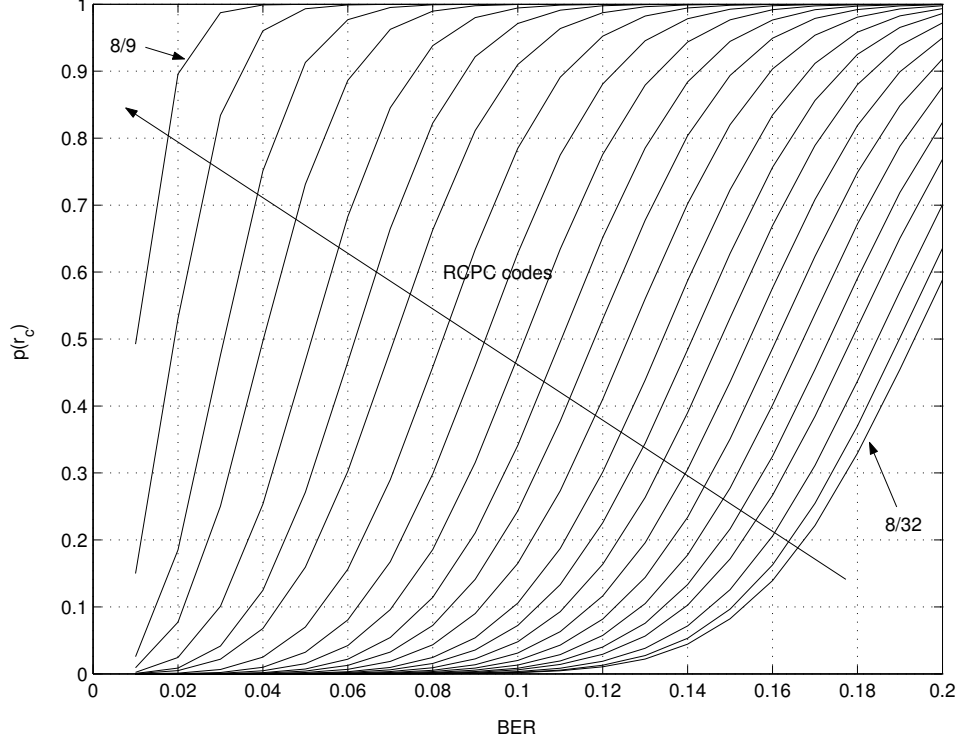
Fig. 8. The probability of packet decoding error $p(r_c)$ with the RCPC codes.

Another reason to assume a BSC is that many JSCC schemes [5, 6, 7] are designed for such channels. When compared with BSC, fading channels has the bursty nature of errors. One straightforward way to break error burst is by using bit-interleaver. In our practical image transmission, a random bit interleaving is performed over all N_P packets corresponding to the whole image.

Note that at high SNR (hence low BER), channel coding is not necessary and more source bits are assigned to obtain better performance. Thus the candidate rates for the UEP design are $\mathcal{R}' = \{1\} \cup \mathcal{R}$, where $r_c = 1$ means no RCPC is applied. Based on the BSC assumption, the probability of packet decoding error with $r_c = 1$

is easy to compute by

$$p(r_c = 1) = 1 - (1 - P_b)^{L_P} \tag{2.19}$$

Once the two sets of parameters are obtained, the DO EPS R is computed by the fast local search algorithm in [6]. Based on R, we compute the expected MSE by (2.10).

In this way, we obtain an end-to-end performance metric of the image transmission system, i.e., $\text{MSE}(\bar{\gamma}_s, M)$ as a function of average SNR and constellation size. The performance derivation is summarized in Fig. 9.
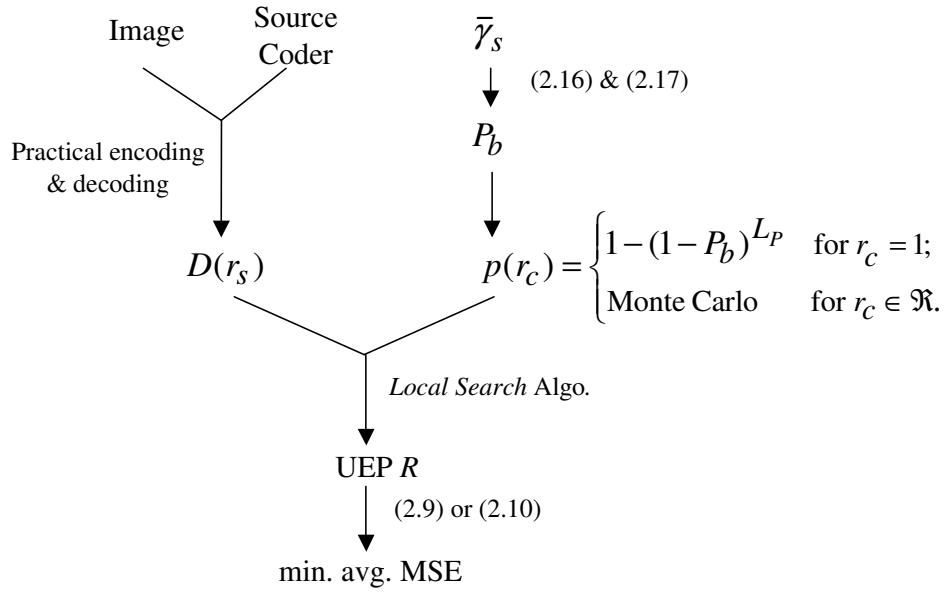
Fig. 9. Summary of performance evaluation of the image transmission system.

1.   Adaptive Modulation Scheme

Based on the performance metric introduced in the previous section, an adaptive modulation scheme [60] can be proposed to match the constellation size M with varying channel conditions. The motivation is that we can potentially achieve high channel throughput (constellation size) by relying on JSCC to handle bad channel conditions (average BER). Thus, with the increase of SNR, we can switch to a larger M to achieve a higher transmission bit rate and use JSCC to help mitigate the effect of increased BER; And for a given SNR, we tradeoff the average BER with M to achieve the best reconstructed image quality. This is fulfilled via the end-to-end performance measure of the image transmission system. To give fair comparisons for various M, we need to keep an identical total symbol energy. One way is to apply different packet lengths as $L_P = L_P^{\mathrm{BPSK}} \log_2 M$ with L_P^{BPSK} being the packet length of BPSK modulation. Other parameter settings are the same for different M.

Our adaptive modulation scheme is formulated as follows. At a given SNR, we pick the M that offers the minimal average MSE subjected to a fixed transmission rate r_t in symbols per pixel (spp), i.e.,

$$M(\bar{\gamma}_s) = \arg \min_{M} \ \mathrm{MSE}(\bar{\gamma}_s, M) \qquad \text{s.t.} \quad r_t = \frac{L_P N_P / \log_2 M}{N_r N_c} = \text{const.}, \ \forall M, (2.20)$$

where a image with $N_r \times N_c$ pixels is assumed.

E.   Numerical Results and Discussions

We study the transmission of the 512×512 gray-scale Lena image over the M-PSK modulated STC-OFDM-based MIMO systems. Given the set of BER curves in Fig.6, only two bounds, i.e., the lower bound (solid line) with $N_T = 2, N_R = 2, \rho = 0$ and the upper bound (dashed line) with $N_T = 2, N_R = 1, \rho = 0$, are considered. To
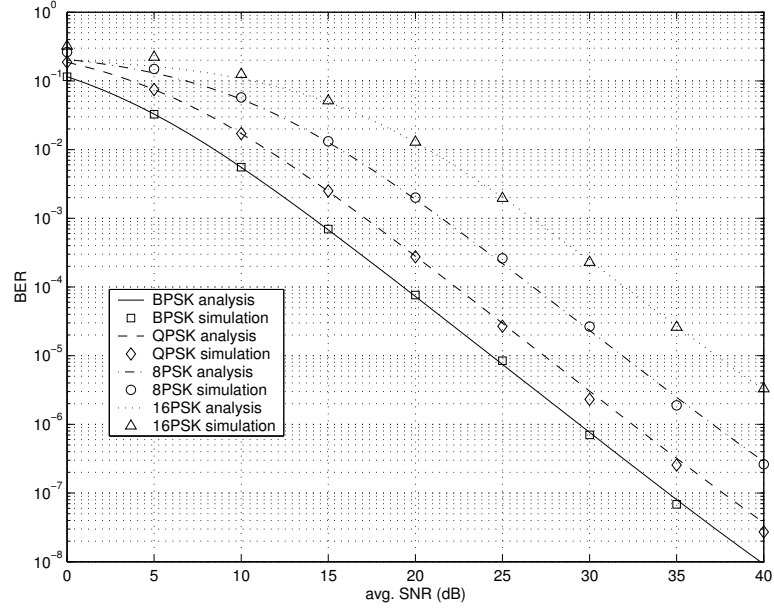
(a) $N_T = 2, N_R = 1$
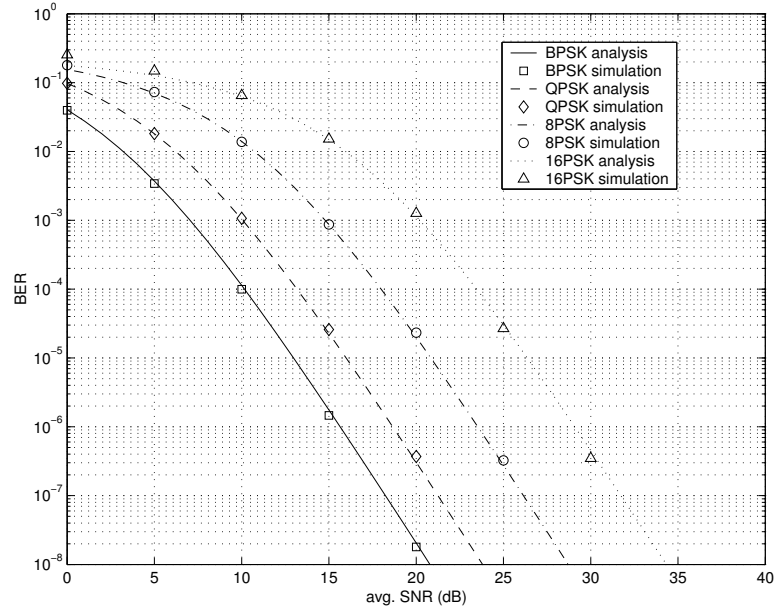
(b) $N_T = 2, N_R = 2$

Fig. 10. BER performances of STC-OFDM-based MIMO system for various constellation sizes M with $K = 128, L = 3, G = 4, f_D T = 10^{-5}$ and (a) $N_T = 2, N_R = 1$, (b) $N_T = 2, N_R = 2$. The performance given by (2.16) and (2.17) is plotted, with discrete points being the corresponding simulation results.

eliminate the effect from the error floor, we select the lower normalized Doppler shift $f_D T = 10^{-5}$. Other parameters about the fading channels are set as in Section 3. Fig. 10 plots the BER performance with various constellation sizes (up to 16PSK). We also give some discrete simulation results, which are in good agreement with the performance of BPSK and QPSK. And for $M > 4$, (2.16) is also a good approximation when SNR>10dB.

For the JSCC scheme, an embedded bitstream generated by the SPIHT image coder is transformed into $N_P = 256$ packets of length $L_p = 256 \log_2 M$ bits each. This corresponds to the transmission rate $r_t = 0.25$ spp. Within each packet, a 16-CRC code [67] generated by 0x15935 polynomial is applied to detect the error. The RCPC codes [68] with generator polynomials $(0117, 0127, 0155, 0171)$ produce a rate $1/4$ mother code having a puncturing rate of 8. Thus the set of RCPC rates is $\mathcal{R} = \{8/9, 8/10, \ldots, 8/32\}$ and the candidate rates for the UEP design are $\mathcal{R}' = \{1\} \cup \mathcal{R}$. Given each code rate r_c and the BER P_b, we evaluate the probability of packet decoding error $p(r_c)$ as shown in Fig. 8.

This image transmission system is evaluated by its PSNR performance. We compute the average MSE of reconstructed image based on the processes in Fig. 9 before converting the average MSE to PSNR by

$$\text{PSNR} = 10 \log_{10} \left(\frac{255^2}{\text{MSE}} \right) \quad \text{(dB)} \tag{2.21}$$

We also confirm our performance evaluation by simulation results, which are generated after averaging the average MSEs of 1000 practical image transmissions before converting the average MSE into PSNR. We assume that the UEP design R in JSCC is determined in advance from the performance evaluation as illustrated in Fig. 9. Note that for the practical image transmission, a random bit interleaving is performed over all $N_P = 256$ packets before the transmission of them through the

STC-OFDM-based MIMO system.

We first consider the case of the upper bound in Fig. 6 (b) with $N_T = 2, N_R = 1, \rho = 0$ in the STC-OFDM system. The PSNR performances versus SNR with various M are plotted in Fig. 11. Obvious and irregular gaps are observed between the PSNR curves of DO and RO solutions with maximal degradations as 0.50, 0.70, 0.93 and 1.37 dB for BPSK, QPSK, 8PSK and 16PSK, respectively. It is not surprising to see that the PSNR curves from RO solutions are not necessarily monotonously increasing since an RO EPS may not lead to a DO EPS. We also show the simulation results in discrete points, which are in good match with the DO solution. For 8PSK and 16PSK, the disagreement between the DO solution and simulation results is only found at quite low SNR, since (2.16) is not a good approximation of BER performance in those cases.

To combat bursty errors in fading channels and validate the BSC assumption in JSCC design, the employment of a random interleaver is necessary in practical image transmission. Based on the same UEP scheme R, we compare the simulation results with and without interleaver in Fig. 11 (a). The significant improvement in PSNR performance shows the effectiveness of the random interleaver.

To give a convenient comparison, we plot the PSNR performances for various M in Fig. 12 (a). We see that the PSNR curve of a larger M starts from a lower point but outperforms that of a smaller M with the increase of SNR, and finally approaches a higher PSNR limit given by source coding since more bits are transmitted. This observation motivates the proposal of a 4-level adaptive modulation scheme to tradeoff average BER with constellation size, as discussed in Section 1. This approach results in 4 SNR ranges as indicated in Table I, each of them is assigned to a constellation size. The best achievable PSNR performance is shown as the thick line in Fig. 12(a), i.e., the envelope of all PSNR curves. Note that the inaccurate approximation for

(a) BPSK
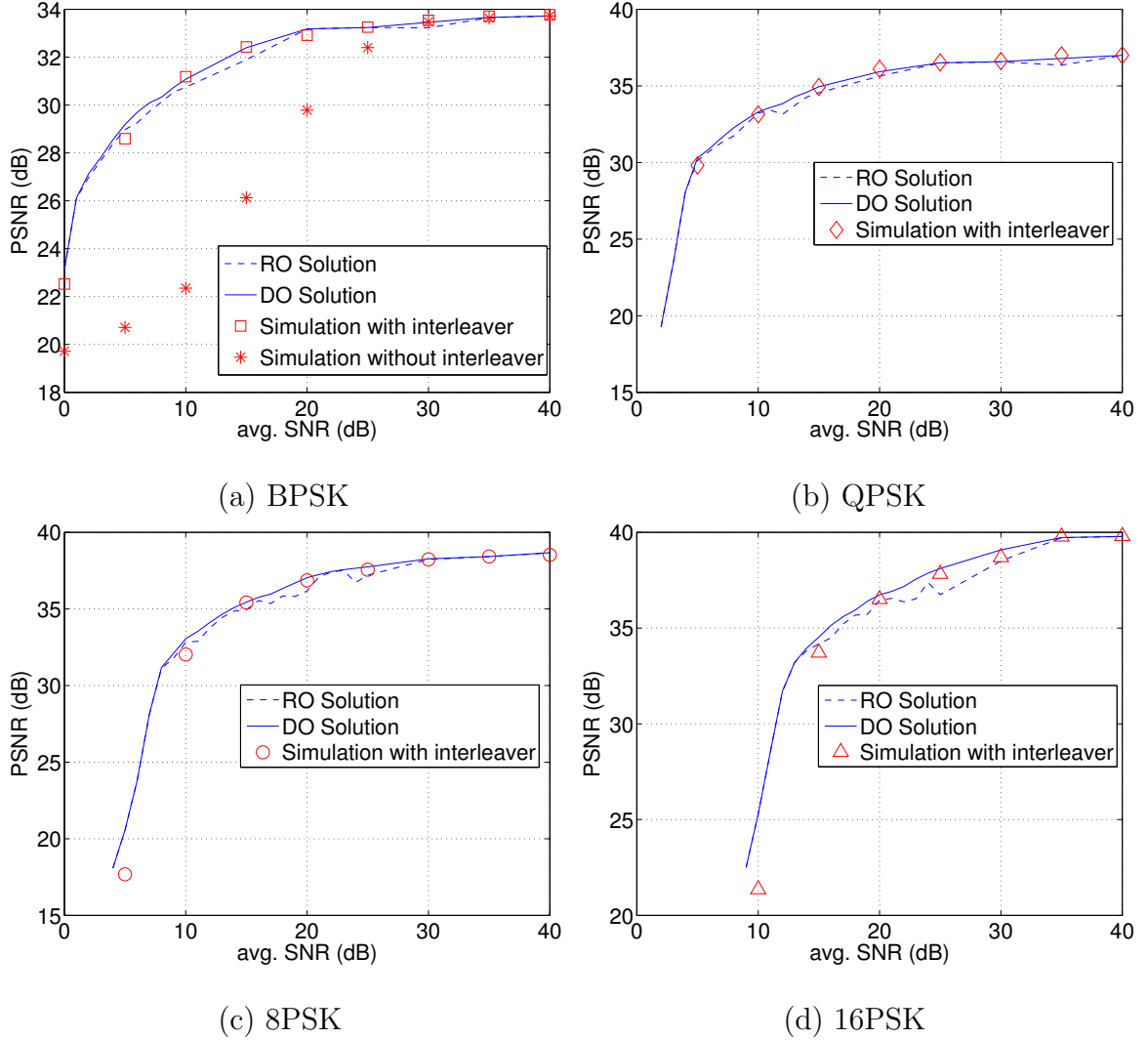
(b) QPSK

(c) 8PSK

(d) 16PSK

Fig. 11. Reconstructed image quality in PSNR of the image transmission system with (a) BPSK, (b) QPSK, (c) 8PSK and (d) 16PSK modulation. $N_P = 256$ packets of length $L_P = 256 \log_2 M$ bits each are transmitted over the STC-OFDM-based MIMO system with $N_T = 2, N_R = 1, K = 128, L = 3, G = 4$ and $f_D T = 10^{-5}$. The PSNR performances of DO and RO solutions are shown in solid lines and dashed lines, respectively. And the simulation results for DO solution are plotted in discrete points.

8PSK and 16PSK at low SNR has no much effect on the allocation of SNR ranges.

PSNR performances of the image transmission system with multiple receive antennas ($N_R = 2$) are given in Fig. 12 (b). When comparing with the case with a single receive antenna for a given M, we see that the diversity gain in BER performance is translated into the improvement in reconstructed image quality. And the improvement is more significant at low SNR because of the PSNR limit determined by source coding and constellation size.

Then a similar 4-level adaptive modulation scheme is proposed. Compared with the case of a single receive antenna, the SNR ranges are left shifted as shown in Table I, since the PSNR curves approach their limits sooner with the increase of SNR. And more PSNR gains for the best achievable reconstructed image quality (i.e., the thick lines in Fig. 12) are observed. Specifically, PSNR gains are 5.7, 2.2, 1.6, 1.1 dB at SNR=0, 10, 20, 30dB, respectively.

Table I. Allocation of SNR ranges for various constellation schemes.

Constellation scheme	SNR range (dB)	
	$N_R = 1$	$N_R = 2$
BPSK	$(-\infty, 4.3]$	$(-\infty, 0.6]$
QPSK	$(4.3, 11.0]$	$(0.6, 10.8]$
8PSK	$(11.0, 22.8]$	$(10.8, 19.0]$
16PSK	$(22.8, +\infty)$	$(19.0, +\infty)$
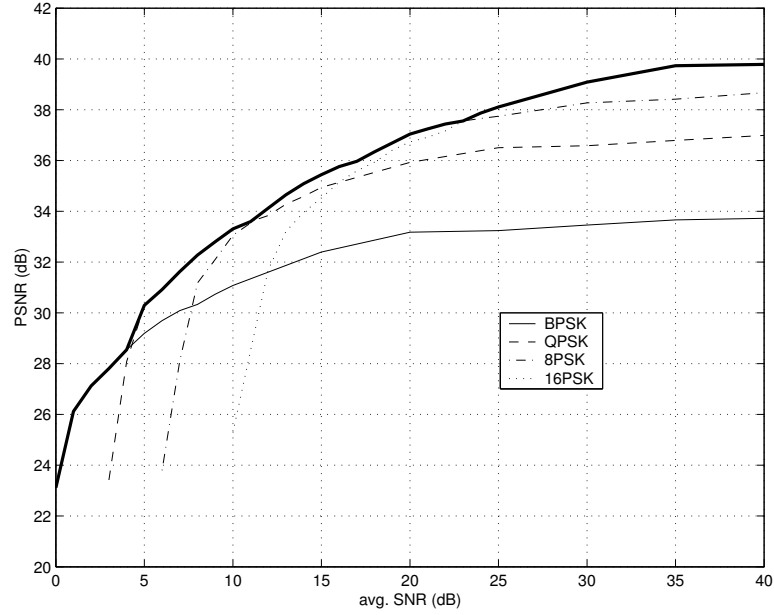
(a) $N_T = 2, N_R = 1$
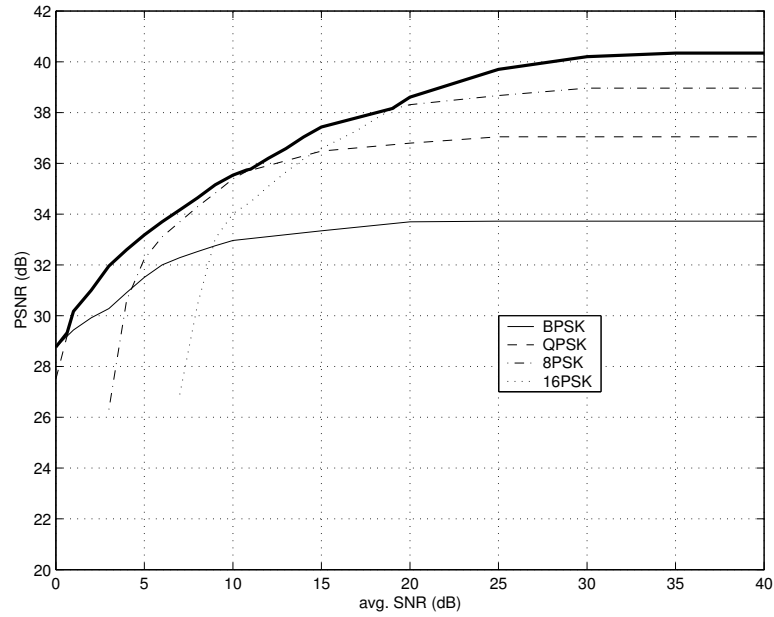
(b) $N_T = 2, N_R = 2$

Fig. 12. Reconstructed image quality in PSNR of the image transmission system for various constellation sizes M. $N_P = 256$ packets of length $L_P = 256 \log_2 M$ bits are transmitted over the STC-OFDM-based MIMO system with $K = 128, L = 3, G = 4, f_D T = 10^{-5}$ and (a) $N_T = 2, N_R = 1$, (b) $N_T = 2, N_R = 2$. The thick line is the envelope of all PSNR curves.

F. Conclusions and Future Work

In this chapter, we describe a robust end-to-end image transmission system by combining physical-layer wireless communication techniques (e.g., STC-OFDM-based MIMO systems) and JSCC. We evaluate STC-OFDM-based MIMO system by its BER performance and then apply the fast algorithm for DO UEP design, so as to map the BER performance into expected reconstructed image quality in PSNR. Based on the PSNR performances for various constellations sizes, we propose an adaptive modulation scheme to tradeoff the channel condition (average BER) with the channel throughput (constellation size) to achieve the best PSNR performance for a given average SNR. Its effectiveness is confirmed by the simulation results. The diversity gain from multiple antennas results in better reconstructed image quality, especially in low SNR range.

To simplify the performance derivation, we assume that the receiver has perfect knowledge of the CSI. But in practice, CSI may not be available at the receiver. One usual solution is DSTC due to its robustness and simplicity. Implemental issues related to this technique are still attractive but beyond the scope of this chapter. And our derivation based on coherent detection provides a upper bound on the performance of the practical image transmission system. Our work based on DSCT will be reported in the next chapter.

There are several directions in which we could carry on our future work. One direction is to apply schemes other than the usage of interleaver to handle fading channels. One scheme is the product code [69, 70]. The row code of the product code is EEP by using a concatenation of an outer CRC code and an inner RCPC code, while the column code is UEP with a systematic RS code. The other scheme is the combination of the packetization technique with the forward error correction

[71, 72]. The idea is to packetize the output bitstream of an embedded source coder into independently decodable packets, which are then protected by a concatenated RCPC/CRC coder with EEP. Both schemes are proved to be efficient. Furthermore, these two schemes require $P_n(r_k)$, the probability that n packets of N_P are detected with errors for RCPC rate r_k, as an input parameter. Compared with the JSCC design in this chapter, $P_n(r_k)$ is easy to determine via simulation over fading channels without the assumption of memoryless channel (e.g., BSC).

Another direction of future research is to improve adaptive modulation. For the adaptive modulation scheme proposed in this chapter, we can not see much gain in PSNR performance at a low SNR range. A more efficient adaptive modulation scheme can be realized by increasing the number of transmit or receive antennas to achieve more diversity gain (approach to an AWGN channel). But this method is not feasible when many antennas are not allowed. Another method is to apply a more efficient channel code (e.g., turbo code [36] or LDPC code [37, 38]) than convolutional code (i.e., RCPC [68]) to combat the fading noise in the STC-OFDM system. More current work is reported by Lan *et al.* in [73], where the design and application of rate-compatible irregular repeat accumulate codes [52] for scalable image transmission over BSCs are studied.

CHAPTER III

PROGRESSIVE IMAGE TRANSMISSION OVER DIFFERENTIALLY
SPACE-TIME CODED OFDM SYSTEMS

A.   Introduction

In Chapter II, we have designed the progressive image transmission system over STC-
OFDM systems and its efficiency has been confirmed via simulations. Based on this
well-studied setup, in this chapter, we consider a scenario which is much closer to the
real practice. In details, we propose a new system with **DSCT** and JSCC based on
product code structure.

1. **DSTC**: In practice, CSI is not available at the receiver. We select DSTC due
   to its robustness and lower complexity when compared to approaches based on
   CSI estimation (e.g., EM-based iterative receiver for space-time coded OFDM
   systems [12]). And it is more power-efficient since no pilot symbols are required
   to track the CSI. However, DSTC exhibits an error floor when employed in fad-
   ing channels, just like the conventional differential demodulation schemes. The
   usual solution is MSD [25], which makes use of ML sequence estimation rather
   than symbol-by-symbol detection as in conventional differential detection. How-
   ever, MSD has relatively high computational complexity. A low-complexity
   DSTC technique, which considerably reduces the error floor, especially in fast
   fading channels, is developed in [26] based on multiple-symbol decision-feedback
   decoding [27, 28]. Due to the increasing demand of real-time wireless commu-
   nication, we adopt this low-complexity decision-feedback differential-detection
   receiver for the image transmission over space-time coded systems. Note that
   DSTC can work well for any fading model given its known channel character-

istics. And the focus of this chapter is the integration of DSTC in the image transmission system. Thus for the sake of simplicity, we assume the **common frequency-selective fading channel** instead of the new broadband MIMO fading model as introduced in Chapter II.

2. **Product code structure**: In Chapter II, the UEP scheme in JSCC is straightforward and simple. And the performance evaluation is further simplified under the assumption of BSC (validated via a long random interleaver). For the practical progressive image transmission, the most powerful JSCC systems are due to Sherwood *et al.* [69] and Sachs *et al.* [70]. Both systems use an embedded wavelet-based source code (e.g., SPIHT [3] and JPEG2000 [4]) and a product channel code. The row code of the product code is a concatenation of an outer CRC code [67] and an inner RCPC code [68], while its column code is a RS code [74]. Both systems use EEP along the rows and UEP along the columns. But whereas the system of [69] puts the earliest symbols of the embedded bitstream in the first rows, the system of [70] puts these symbols in the first columns. Consequently, the first system has a better progressive ability. On the other hand, the system of [70] offers a better reconstruction quality. From another view of channel coding, systematic RS codes [74] are capable of correcting bursty errors due to fading channels. As demonstrated in [69], more powerful error protection can be achieved when another channel code (e.g., a RCPC/CRC code [56]) is applied perpendicularly to the RS codes. Thus we choose the product code structure briefly mentioned in [69] but made more explicit in [70, 29], where the required UEP is employed along the column RS code before EEP along the row RCPC/CRC code.

Note that advanced channel codes (e.g., turbo codes [36] or low-density parity-check codes [37, 38]) can be used in place of the simple RCPC/CRC code with higher complexity or longer delay. Moreover, the JSCC scheme also allows us to treat the packets in the product code structure as the MDs of the image. These facts motivate us to combine techniques in signal processing (MD coding) and communications (channel coding and space-time coding) in a framework based on iterative (turbo) decoding for image transmission over wireless fading channels.

MD coding [75] has recently emerged as an attractive framework for robust multimedia transmission over on-off channels. MD coding is a technique that generates multiple correlated descriptions of a source. Any one of these descriptions can be used to reproduce the original source with certain fidelity. When more than one descriptions are available to the decoder, they can be synergistically combined to enhance the quality. From a source coding viewpoint, MDs can be generated via MD quantization, MD correlating transforms, or MD coding with frames. MD coding can also be viewed as a means of JSCC, then the MDs can be easily generated with embedded coding [3] and UEP [76].

Srinivasan [77] first employed iterative (turbo) technique in decoding MDs transmitted over an AWGN channel. Results in [77] (with a Gaussian source and two MD scalar quantizers [78]) indicate that the efficacy of iterative decoding depends on the amount of correlation in the two descriptions. Moreover, at the same overall transmission rate, the system employing MD coding in [77] was shown to outperform a reference system that uses only scalar quantization. Other related works are in [79, 80, 81].

We study transporting MDs over wireless fading channels [82, 83] rather than the on-off channels considered in most works related to MD coding. The idea is to use channel coding (e.g., iterative decoding [84]) techniques developed for serially con-

catenated coding systems to improve the performance of the receiver with successive iterations. One similar work was discussed by Barros *et. al* in [85], where the iterative decoder is fulfilled by the concatenation of MD scalar quantization and convolutional codes.

From the above discussions, in the second part of this chapter, we treat MD coding as JSCC and apply iterative (turbo) decoding of MDs for image transmission. Motivated by the work in [86], we consider the image transmission system consisting of two constituent codes – an MD code as the outer code and a differential space-time code as the inner code. Both constituent codes are used as means of introducing redundancy for error robustness. The outer MD code can be based on MD correlating image transforms or embedded coding [3] and UEP [76]. We adopt the latter approach and split an embedded image bitstream into MDs using the product code structure in [76]. The inner code is a channel code whose rate depends on the amount of diversity in space-time coding [14]. In this work, we fix this amount of diversity (hence the inner code rate) and rely on optimal design of the outer MD code to handle channel variations. Specifically, for a given channel condition (or BER), optimal MD coding is determined via JSCC in the form of embedded coding and optimal product code design. The row code of the product code [69, 70] uses a concatenation of CRC code and RCPC code, as necessitated by the iterative decoding algorithm of [86]. The column code employs a systematic RS code that guarantees successful generation of MDs (rows). Based on a serial concatenation of the two constituent codes, the MDs are multiplexed and interleaved using a random interleaver before being passed to the differential space-time coder. The differential space-time coder then maps the input bits into MPSK symbols and transmits them using two antennas through a flat-fading channel.

To iteratively decode the differential space-time coded MDs, we propose a receiver that consists of a MAP differential space-time decoder [86], an MD decoder, an interleaver and a deinterleaver. The two decoders exchange extrinsic values or *a priori probabilities* (APP) of transmitted bits between themselves in successive iterations.

This chapter is organized as follows. We start by reviewing DSTC, the EM-based iterative receiver with CSI estimation, and the product code structure in Section B. Then we combine the embedded image coder, product code, and DSTC for progressive image transmission over DSTC systems in Section C. The iterative decoding of differentially space-time coded multiple descriptions of images is motivated and discussed in Section D. Finally, the numerical results are given in Section E, and the conclusions are drawn in Section F.

B. Background

1. EM-based Iterative Receiver for STC-OFDM System

In Chapter II, we have reviewed the transmission model of an STC-OFDM communication system and its coherent detection by assuming perfect CSI at the receiver. When no CSI is available, we estimate the CSI and employ the EM-based ML receiver for STC-OFDM systems [12]. Such a communication scheme is usually carried out in a burst manner. The data burst is shown in Fig. 13. The first slot contains the known pilot symbols. The rest slots contain q STC codewords.

The ML detection problem based on (2.6) is

$$\underline{\hat{X}} = \arg\max_{\underline{X}} \sum_{i=1}^{N_R} \log p\left(\underline{y}_i | \underline{X}\right) \tag{3.1}$$

where the summation of log-probabilities from all N_R receive antennas follows from the assumption that the noise at different receive antennas are independent. The
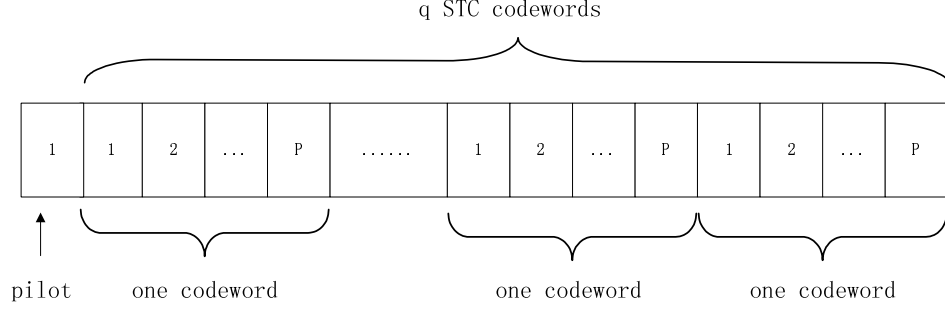
Fig. 13. The data burst used in EM-based iterative receiver. The first slot contains the known pilot symbols, and the rest slots contain q STC codewords.

optimal solution to (3.1) is of prohibitive complexity. To reduce the complexity, we use the EM algorithm to solve (3.1) iteratively according to the following steps [12]:

1. E-step: Compute$Q\left(\underline{\boldsymbol{X}}|\underline{\boldsymbol{X}}^{(\kappa)}\right) = \mathrm{E}\left\{\left[\sum_{i=1}^{N_R}\log p\left(\underline{\boldsymbol{y}}_i|\underline{\boldsymbol{X}},\boldsymbol{h}_i\right)\right]\middle|\underline{\boldsymbol{y}}_i,\underline{\boldsymbol{X}}^{(\kappa)}\right\}$ (3.2)

2. M-step: Solve$\underline{\boldsymbol{X}}^{(\kappa+1)} = \arg\max_{\underline{\boldsymbol{X}}} Q\left(\underline{\boldsymbol{X}}|\underline{\boldsymbol{X}}^{(\kappa)}\right);$ (3.3)

where $\underline{\boldsymbol{X}}^{(\kappa)}$ denotes the decisions of the data symbols at the κ-th EM iteration. Note that $\underline{\boldsymbol{X}}^{(\kappa)}$ must satisfy the STC coding constraints in (2.5).

And the EM-based iterative space-time decoding algorithm can be summarized as [12]

1. Definitions:

$$\underline{\boldsymbol{y}}_i[m] \triangleq \left[\boldsymbol{y}_i^{\mathrm{H}}[mP+1],\ldots,\boldsymbol{y}_i^{\mathrm{H}}[mP+P]\right]^{\mathrm{H}}$$
$$\{\underline{\boldsymbol{y}}_i[m]\}_i \triangleq \left\{\underline{\boldsymbol{y}}_1[m],\ldots,\underline{\boldsymbol{y}}_{N_R}[m]\right\}$$
$$\boldsymbol{X}[m] \triangleq \left[\boldsymbol{X}^{\mathrm{H}}[mP+1],\ldots,\boldsymbol{X}^{\mathrm{H}}[mP+P]\right]^{\mathrm{H}}$$

2. Channel estimate for the pilot slot: $\hat{\boldsymbol{h}}_i[0] = \frac{1}{K}\boldsymbol{W}^{\mathrm{H}}\boldsymbol{X}^{\mathrm{H}}[0]\boldsymbol{y}_i[0],\quad i=1,\ldots,N_R$

3. EM-based iterative decoding for the q data slots:

    for $m=0,1,\ldots,q-1$

for $n = 1, 2, \ldots, P$

$$\tilde{\boldsymbol{h}}_i[mP + n] = \text{Temp-filter}\left\{\hat{\boldsymbol{h}}_i[mP + n - 1], \ldots, \hat{\boldsymbol{h}}_i[mP + n - \iota]\right\},$$

$$\triangleq \sum_{j=1}^{\iota} a_j \hat{\boldsymbol{h}}_i[mP + n - j], \qquad i = 1, \ldots, N_R$$

where $\hat{\boldsymbol{h}}_i[mP + n - j], j = 1, \ldots, \iota$, is computed by Step $(\star)$ below;

$\{a_j\}_{j=1}^{\iota}$ denotes the coefficients of an ι-length ($\iota \leq Pq$) temporal

filter, which can be pre-computed by solving the Wiener equation or

from the robust design as in [19, 20].

end

Initial estimation of $\underline{\boldsymbol{X}}^{(0)}$ [19, 20]:

$$\underline{\boldsymbol{X}}^{(0)}[m] = \arg\max_{\underline{\boldsymbol{X}}}\left\{\sum_{i=1}^{N_R}\sum_{n'=1}^{P}\log p\left[\boldsymbol{y}_i[mP + n']|\underline{\boldsymbol{X}}, \tilde{\boldsymbol{h}}_i[mP + n']\right]\right\}$$

EM-based iterative decoding by (3.2) and (3.3):

$$\underline{\boldsymbol{X}}^{(\kappa+1)} = \text{EM}\left\{\{\underline{\boldsymbol{y}}_i[m]\}_i, \underline{\boldsymbol{X}}^{(\kappa)}[m]\right\}$$

for $n = 1, 2, \ldots, P$

$$\hat{\boldsymbol{h}}_i[mP+n] = \frac{1}{K}\boldsymbol{W}^{\text{H}}\underline{\boldsymbol{X}}^{(I)\text{H}}[m]\underline{\boldsymbol{y}}_i[m], \qquad i = 1, \ldots, N_R \qquad (\star)$$

end

end

2. Differential Space-time Coding

Differential coding is a simple and efficient way to handle the case when no CSI is available at the receiver. For STC, it is easy to design the differential coding scheme for $N_T = 2$ transmit antennas based on the code matrix (2.5) [24]. However, it is not easy to extend the scheme to the case with $N_T > 2$ without a penalty in rate. Because according to [24], the code matrix $\mathcal{G}$ should be orthogonal, but such designs do not exist for $N_T > 2$ [17]. Thus we only consider the system with two transmit antennas (i.e., $N_T = 2, P = 2$) in the sequel.

Firstly, we define the following vectors and matrices for $N_T = 2, P = 2$

$$\boldsymbol{a}_n[p, k] \triangleq [a_{n,1}[p, k], a_{n,2}[p, k]]^{\mathrm{H}}, \qquad p = 1, 2; k = 1, \dots, K, \quad (3.4)$$

$$\boldsymbol{A}_{n,j}[p] \triangleq \mathrm{diag}\{a_{n,j}[p, 1], \dots, a_{n,j}[p, K]\}_{K \times K}, p = 1, 2; j = 1, 2, \quad (3.5)$$

$$\boldsymbol{A}_n[p] \triangleq [\boldsymbol{A}_{n,1}[p], \boldsymbol{A}_{n,2}[p]]_{K \times (2K)}, \qquad p = 1, 2, \dots, \quad (3.6)$$

$$\underline{\boldsymbol{A}}_n \triangleq [\boldsymbol{A}_n^{\mathrm{H}}[1], \boldsymbol{A}_n^{\mathrm{H}}[2]]_{(2K) \times (2K)}^{\mathrm{H}}. \quad (3.7)$$

where $a_{n,j}[p, k]$ is the MPSK information symbol transmitted from the j-th transmit antenna at the k-th sub-carrier and at the p-th OFDM word of the n-th STC codeword. And the coding constraints of STC are taken into account when constructing the data vector $\boldsymbol{a}_n[p, k] \in \mathcal{A}^{N_T}, \forall p$, i.e., $\boldsymbol{a}_n[p, k], \forall p$, are different permutations and/or transformations of $\boldsymbol{a}_n[1, k]$ as defined in (2.5). Finally, $\underline{\boldsymbol{A}}_n$ contains all the information symbols associated with the n-th STC codeword.

Next the space-time differential block code is recursively defined as

$$\underline{\boldsymbol{X}}_0 = \underline{\boldsymbol{A}}_0, \qquad \underline{\boldsymbol{G}}_n \triangleq \underline{\boldsymbol{A}}_n \underline{\boldsymbol{A}}_0^{\mathrm{H}}, \qquad \underline{\boldsymbol{X}}_n = \underline{\boldsymbol{G}}_n \underline{\boldsymbol{X}}_{n-1}, \ n = 1, 2, \dots, \quad (3.8)$$

It is easy to verify that $\underline{\boldsymbol{A}}_n$, $\underline{\boldsymbol{G}}_n$ and $\underline{\boldsymbol{X}}_n$ are all orthogonal matrices for $N_T = 2, P = 2$, i.e.,

$$\underline{\boldsymbol{A}}_n \underline{\boldsymbol{A}}_n^{\mathrm{H}} = \underline{\boldsymbol{A}}_n^{\mathrm{H}} \underline{\boldsymbol{A}}_n = \boldsymbol{I}_{2K}, \quad \underline{\boldsymbol{G}}_n \underline{\boldsymbol{G}}_n^{\mathrm{H}} = \underline{\boldsymbol{G}}_n^{\mathrm{H}} \underline{\boldsymbol{G}}_n = \boldsymbol{I}_{2K}, \quad \underline{\boldsymbol{X}}_n \underline{\boldsymbol{X}}_n^{\mathrm{H}} = \underline{\boldsymbol{X}}_n^{\mathrm{H}} \underline{\boldsymbol{X}}_n = \boldsymbol{I}_{2K}. \quad (3.9)$$

Similarly with (2.6), the received signal can be modelled as

$$\underline{\boldsymbol{y}}_{n,i} = \underline{\boldsymbol{X}}_n \boldsymbol{W} \boldsymbol{h}_{n,i} + \underline{\boldsymbol{z}}_{n,i}, \qquad i = 1, \dots, N_R, n = 0, 1, \dots, \quad (3.10)$$

$$\text{with } \underline{\boldsymbol{y}}_{n,i} = [\boldsymbol{y}_{n,i}^{\mathrm{H}}[1], \boldsymbol{y}_{n,i}^{\mathrm{H}}[2]]_{(2K) \times 1}^{\mathrm{H}}, \ \underline{\boldsymbol{z}}_{n,i} = [\boldsymbol{z}_{n,i}^{\mathrm{H}}[1], \boldsymbol{z}_{n,i}^{\mathrm{H}}[2]]_{(2K) \times 1}^{\mathrm{H}},$$

$$\boldsymbol{h}_{n,i} = \boldsymbol{h}_{n,i}[1] = \boldsymbol{h}_{n,i}[2],$$

where $\underline{\boldsymbol{y}}_{n,i}[p]$ is the K-dimensional vector of the received signals from the i-th receive

antenna at the p-th OFDM word in the n-th STC codeword. $\boldsymbol{z}_{n,i}[p]$ is the AWGN with covariance matrix $\sigma_z^2 \boldsymbol{I}$.

a. Multiple-symbol Decision-feedback Differential Space-time Decoding

Now we review multiple-symbol decision-feedback differential space-time decoding [26]. The communication is carried out in a burst manner as shown in Fig. 14. For MSD, we decode the current OFDM codeword (n-th codeword) together with the previous $N-1$ codewords ($\{n-1, n-2, \ldots, n-N+1\}$-st codewords), where N is the observation window size.
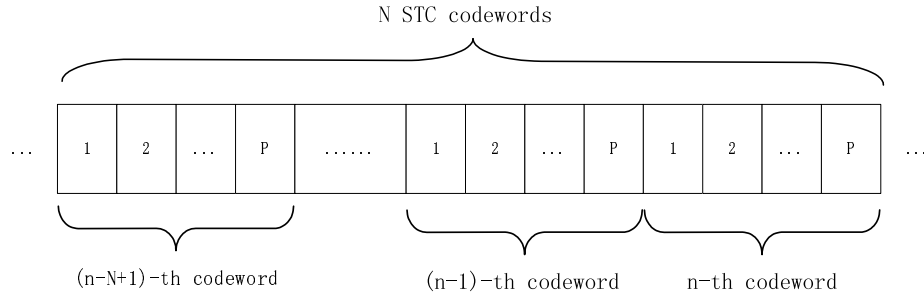
Fig. 14. The data burst used in multiple-symbol detection. Where N is the observation window size.

Then (3.10) can be modified as

$$\overline{\boldsymbol{y}}_{n,i} = \overline{\boldsymbol{X}}_n \overline{\boldsymbol{W}} \overline{\boldsymbol{h}}_{n,i} + \overline{\boldsymbol{z}}_{n,i}, \qquad i = 1, \ldots, N_R, \tag{3.11}$$

$$\text{where} \quad \overline{\boldsymbol{y}}_{n,i} = \left[\underline{\boldsymbol{y}}_{n,i}^{\mathrm{H}}, \underline{\boldsymbol{y}}_{n-1,i}^{\mathrm{H}}, \cdots \underline{\boldsymbol{y}}_{n-N+1,i}^{\mathrm{H}}\right]_{(2NK)\times 1}^{\mathrm{H}},$$

$$\overline{\boldsymbol{X}}_n = \mathrm{diag}\left\{\underline{\boldsymbol{X}}_n, \underline{\boldsymbol{X}}_{n-1}, \ldots, \underline{\boldsymbol{X}}_{n-N+1}\right\}_{(2NK)\times(2NK)},$$

$$\overline{\boldsymbol{W}} = \mathrm{diag}\left\{\boldsymbol{W}, \boldsymbol{W}, \ldots, \boldsymbol{W}\right\}_{(2NK)\times(2NL)},$$

$$\overline{\boldsymbol{h}}_{n,i} = \left[\underline{\boldsymbol{h}}_{n,i}^{\mathrm{H}}, \underline{\boldsymbol{h}}_{n-1,i}^{\mathrm{H}}, \cdots \underline{\boldsymbol{h}}_{n-N+1,i}^{\mathrm{H}}\right]_{(2NL)\times 1}^{\mathrm{H}},$$

$$\overline{\boldsymbol{z}}_{n,i} = \left[\underline{\boldsymbol{z}}_{n,i}^{\mathrm{H}}, \underline{\boldsymbol{z}}_{n-1,i}^{\mathrm{H}}, \cdots \underline{\boldsymbol{z}}_{n-N+1,i}^{\mathrm{H}}\right]_{(2NK)\times 1}^{\mathrm{H}},$$

$$\overline{\boldsymbol{G}}_n = \left[\underline{\boldsymbol{G}}_n, \underline{\boldsymbol{G}}_{n-1}, \cdots \underline{\boldsymbol{G}}_{n-N+2}\right]_{(2K)\times(2(N-1)K)}.$$

The ML detection problem is given by

$$\hat{\overline{\boldsymbol{X}}}_n = \arg \max_{\overline{\boldsymbol{X}}_n} \sum_{i=1}^{N_R} \log p\left(\overline{\boldsymbol{y}}_{n,i} | \overline{\boldsymbol{G}}_n\right). \tag{3.12}$$

Based on (2.2) and (3.11), after detailed derivations, (3.12) is converted to an MSD rule as [26]

$$\hat{\underline{\boldsymbol{G}}}_n = \sum_{k=0}^{K-1} \arg \min_{\underline{\boldsymbol{G}}_n(k)} \Re \left\{ \sum_{i=1}^{N_R} \sum_{i'=0}^{N-1} \sum_{j'=i'+1}^{N-1} t_{i',j'} \underline{\boldsymbol{y}}_{n-i',i}^{\mathrm{H}}(k) \left(\prod_{n'=i'}^{j'-1} \underline{\boldsymbol{G}}_{n-n'}(k)\right) \underline{\boldsymbol{y}}_{n-j',i}(k) \right\}, \tag{3.13}$$

where $\Re(\cdot)$ denotes the calculation of the real part of a number. $\underline{\boldsymbol{y}}_{n,i}(k), \underline{\boldsymbol{X}}_n(k), \underline{\boldsymbol{G}}_n(k)$ denote the corresponding matrices associated with the k-th sub-carrier, i.e.,

$$
\begin{aligned}
\left[\underline{\boldsymbol{y}}_{n,i}(k)\right]_{i',1} &\triangleq \left[\underline{\boldsymbol{y}}_{n,i}\right]_{((i'-1)K+k+1,1)}, \\
\left[\underline{\boldsymbol{X}}_n(k)\right]_{i',j'} &\triangleq \left[\underline{\boldsymbol{X}}_n\right]_{((i'-1)K+k+1,(j'-1)K+k+1)}, \\
\left[\underline{\boldsymbol{G}}_n(k)\right]_{i',j'} &\triangleq \left[\underline{\boldsymbol{G}}_n\right]_{((i'-1)K+k+1,(j'-1)K+k+1)}, \quad i' = 1, 2; j' = 1, 2. \tag{3.14}
\end{aligned}
$$

And $\boldsymbol{T} = [t_{i',j'}] = \left(\Sigma_\alpha + \frac{\sigma_z^2}{E_\alpha} \boldsymbol{I}_N\right)^{-1}$, where the normalized $N \times N$ autocorrelation matrix Σ_α has elements given by $\Sigma_\alpha[i', j'] = J_0\left(2\pi f_D(2T_s)(i' - j')\right)$. Note that during the derivation, we assume that the total power of fading process associated with each transmit-receive antenna pair is equal to each other, i.e., $\sum_{l=0}^{L-1} \sigma_{i,j,l}^2 = E_\alpha, \forall i, j$. For simplicity, we also ignore the correlations among the channel frequency responses at different sub-carriers [26].

From (3.13), we can detect $\underline{\boldsymbol{G}}_n$ by solving K independent minimization problems, i.e., we can handle each sub-carrier independently. And it is necessary to calculate $KM^{2(N-1)}$ metrics to detect $\underline{\boldsymbol{G}}_n$. So the computational complexity is $KM^{2(N-1)}/(N-1)$ metric calculations per code word, which grows exponentially with N. A simple and efficient way to reduce the computational complexity is to replace the previous symbol matrices $\underline{\boldsymbol{G}}_{n-1}, \ldots, \underline{\boldsymbol{G}}_{n-N+2}$ in (3.13) by decision-feedback matrices $\hat{\underline{\boldsymbol{G}}}_{n-1}, \ldots, \hat{\underline{\boldsymbol{G}}}_{n-N+2}$. In this way, we obtain symbol-by-symbol decision instead of

block decision. Thus (3.13) can be translated into the following decision-feedback decoding rule as

$$\underline{\hat{\boldsymbol{G}}}_n(k) = \arg\min_{\underline{\boldsymbol{G}}_n(k)} \Re \left\{ \sum_{i=1}^{N_R} \underline{\boldsymbol{y}}_{n,i}^{\mathrm{H}}(k) \underline{\boldsymbol{G}}_n(k) \sum_{j'=1}^{N-1} t_{0,j'} \left(\prod_{n'=1}^{j'-1} \underline{\hat{\boldsymbol{G}}}_{n-n'}(k) \right) \underline{\boldsymbol{y}}_{n-j',i}(k) \right\}. \quad (3.15)$$

Finally the decision-feedback space-time differential decoding algorithm can be summarized as follows:

1. Initialization: Let $\underline{\hat{\boldsymbol{A}}}_0 = \underline{\boldsymbol{A}}_0$; Compute $\boldsymbol{T} = \left(\Sigma_\alpha + \frac{\sigma_z^2}{E_\alpha} \boldsymbol{I}_N \right)^{-1}$.

2. Estimation of the initial symbols by MSD:

   for $n = 1, 2, \ldots, N-1$

   $\underline{\hat{G}}_n$ by (3.13), choose the window size as 2;

   Differentially decoding $\underline{\hat{A}}_n = \underline{\hat{G}}_n \underline{\hat{A}}_0$.

   end

3. Decision-feedback detection:

   for $n = N, N+1, \ldots$

   Estimate $\underline{\hat{G}}_n$ by (3.15), choose the window size as N;

   Differentially decoding $\underline{\hat{A}}_n = \underline{\hat{G}}_n \underline{\hat{A}}_0$.

   end

b. Comparison in Computational Complexity with EM-based Iterative Receiver

In this section, we compare the computational complexities for the two non-coherent detection algorithms: the decision-feedback differential space-time decoding and the EM-based iterative receiver design. Specifically, we compare the number of complex multiplications in both methods.

Decision-feedback differential space-time decoding based on (3.15) involves a total of $KN_R((2+4)M^2 + (N-1) + 4\frac{(N-1)(N-2)}{2}) = KN_R(6M^2 + (N-1)(2N-3))$ complex multiplications. However, some multiplications are not necessary since they have already been computed previously. That is, we modify (3.15) to

$$
\begin{aligned}
\underline{\hat{\boldsymbol{G}}}_n(k) &= \arg\min_{\underline{\boldsymbol{G}}_n(k)} \Re \left\{ \sum_{i=1}^{N_R} \underline{\boldsymbol{y}}_{n,i}^{\mathrm{H}}(k) \underline{\boldsymbol{G}}_n(k) \sum_{j'=1}^{N-1} t_{0,j'} \hat{\underline{\boldsymbol{G}}}_{n-1}(k) \left(\prod_{n'=2}^{j'-1} \hat{\underline{\boldsymbol{G}}}_{n-n'}(k) \right) \underline{\boldsymbol{y}}_{n-j',i}(k) \right\} \\
&= \arg\min_{\underline{\boldsymbol{G}}_n(k)} \Re \left\{ \sum_{i=1}^{N_R} \underline{\boldsymbol{y}}_{n,i}^{\mathrm{H}}(k) \underline{\boldsymbol{G}}_n(k) \sum_{j'=1}^{N-1} t_{0,j'} \hat{\underline{\boldsymbol{G}}}_{n-1}(k) \underline{\boldsymbol{F}}_{(n-1)-(j'-1),i}(k) \right\}
\end{aligned}
$$

$$
\text{with} \qquad \underline{\boldsymbol{F}}_{(n-1)-(j'-1),i}(k) = \left(\prod_{n''=1}^{j'-2} \hat{\underline{\boldsymbol{G}}}_{(n-1)-n''}(k) \right) \underline{\boldsymbol{y}}_{(n-1)-(j'-1),i}(k). \qquad (3.16)
$$

Note that $\underline{\boldsymbol{F}}_{(n-1)-(j'-1),i}(k)$ for $j' \geq 3$ has been determined during the detection of $\hat{\underline{\boldsymbol{G}}}_{n-1}(k)$. In this way, we can further reduce the number of complex multiplications to $KN_R(6M^2 + 5(N-1))$.

It is not straightforward to evaluate the computational complexity of the EM-based iterative space-time decoding algorithm, as summarized in Section 1. For simplicity, we only compute the number of complex multiplications during the EM iterations and ignore the FFT operations when calculating the channel responses in the frequency domain. According to (17) in [12], $IKN_R(6+12)M^2$ complex multiplications are required to detect one STC-OFDM codeword, where I denotes the number of iterations.

For QPSK modulation and 5 iterations for EM algorithm, we see that the EM-based iterative decoding is about 12.5 times slower than the decision-feedback differential space-time decoding with the observation window size $N = 5$. If we take into account the temporal-filtering to estimate the time-domain channel responses, the FFT operations in the metric calculation and the initial estimation of $\underline{\boldsymbol{X}}^{(0)}$, the computational complexity will be even higher. Due to the increasing demand of real-

time wireless transmission, we adopt the low-complexity decision-feedback differential space-time coding in the physical layer of our image transmission system.

3. Product Code Structure and Fast Local Search Algorithm

The product code structure is illustrated in Fig. 15. Let $\mathcal{R} = \{r_1, r_2, \ldots, r_m\}$, with $r_1 < \cdots < r_m$, be the set of RCPC code rates, N_P the number of packets and L_P the packet length in symbols (e.g., bytes). For $r_i \in \mathcal{R}$, $L(r_i)$ denotes the sum of the number of source symbols and RS redundant symbols used in a packet protected by RCPC code rate r_i. Thus, we have $L(r_i)$ source segments $S_1, \ldots, S_{L(r_i)}$, where segment S_j, $1 \leq j \leq L(r_i)$, consists of $m_j \in \{1, \ldots, N_P\}$ source symbols that are protected by $f_j = N_P - m_j$ RS symbols.
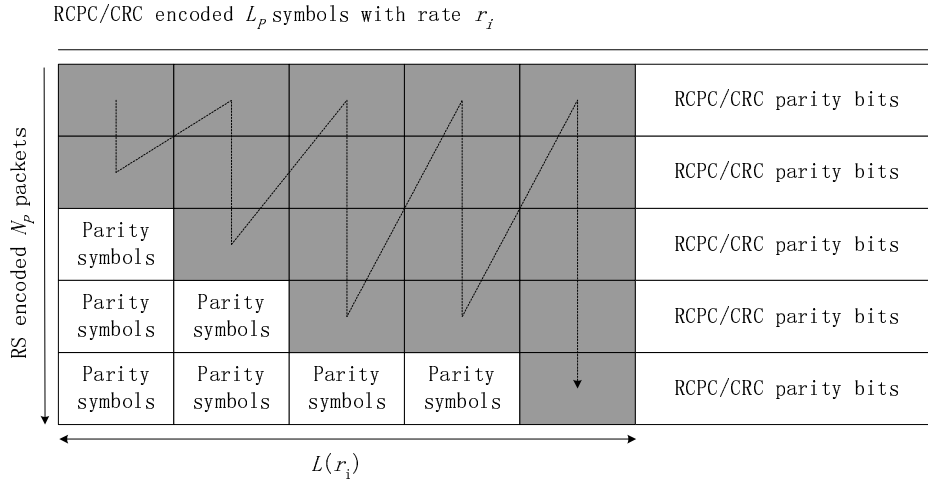
Fig. 15. Product code structure. There are $N_P = 5$ packets. Every shaded cell is a source symbol. The embedded source bitstream flows along the direction of the dashed line.

The N_P packets are sent over the wireless channel. Each received packet is decoded with the RCPC decoder. If the CRC detects an error, then the packet is considered to be decoded with errors (we suppose that all errors can be detected).

Suppose now that n out of N_P packets are decoded with errors, then the RS codes ensure that all segments that contain at most $N_P - n$ source symbols can be recovered. By adding the constraint $f_1 \geq f_2 \geq \cdots \geq f_{L(r_i)}$, we guarantee that the receiver can decode at least the first j segments whenever at most f_j packets are with errors. In the sequel, $\mathcal{F}_i$ denotes the set of $L(r_i)$-tuples $(f_1, \ldots, f_{L(r_i)})$ such that $f_1 \geq f_2 \geq \cdots \geq f_{L(r_i)}$ and $f_j \in \{0, \ldots, N_P - 1\}$ for $j = 1, \ldots, L(r_i)$. Moreover, $p_N(n)$ denotes the probability that n out of N_P packets are with errors. For fading channels parameterized by the average BER, the probability function $p_N(n)$ can be obtained via simulation with Jakes' method [66]. The optimization problem is to determine $F = (f_1, \ldots, f_{L(r_i)}) \in \mathcal{F}_i$ for each code rate r_i to achieve the best reconstructed image quality in some criteria.

One usual criterion is DO solution. Let $D(\cdot)$ denote the operational distortion-rate function of the source coder and let χ be the random variable whose value is the number of error packets. For a given code rate r_i, a DO $L(r_i)$-RS protection is a solution to the problem

$$\min_{F \in \mathcal{F}_i} \mathrm{E}[D](F) = \min_{F \in \mathcal{F}_i} \sum_{k=0}^{L(r_i)} P_k(F) D(t_k), \qquad (3.17)$$

where $P_0(F) = P(\chi > f_1), P_k(F) = P(f_{k+1} < \chi \leq f_k)$ for $k = 1, \ldots, L(r_i) - 1$, $P_{L(r_i)}(F) = P(\chi \leq f_{L(r_i)}), t_0 = 0$, and $t_k = \sum_{j=1}^{k} m_j$ for $k = 1, \ldots, L(r_i)$. For $k = 1, \ldots, L(r_i) - 1$, we have $P_k(F) = 0$ if $f_k = f_{k+1}$ and $P_k(F) = \sum_{n=f_{k+1}+1}^{f_k} p_N(n)$, otherwise.

An optimal product code is then given by an RCPC code rate r_i and an $L(r_i)$-RS protection F that solve the minimization problem

$$\min_{r_i \in \mathcal{R}} \min_{F \in \mathcal{F}_i} \sum_{k=0}^{L(r_i)} P_k(F) D(t_k). \qquad (3.18)$$

Solving problem (3.18) by brute-force is impractical because the number of possible solutions is $\sum_{i=1}^{m} \binom{L(r_i)+N_P-1}{L(r_i)}$.

Instead of solving the high-complexity problem in (3.18), a RO solution is first computed as an RS protection scheme that maximizes the expected number of correctly received source symbols. That is, an RO $L(r_i)$-protection is a solution to the problem

$$\max_{F \in \mathcal{F}_i} \mathrm{E}[r](F) = \max_{F \in \mathcal{F}_i} \sum_{k=0}^{L(r_i)} P_k(F) t_k. \tag{3.19}$$

The computation of an RO solution is straightforward. Indeed,

$$\mathrm{E}[r](F) = \sum_{j=1}^{L(r_i)} m_j \sum_{i=0}^{f_j} p_N(i). \tag{3.20}$$

Thus, an RO solution is $(f_r, \ldots, f_r)$, where

$$f_r = \arg \max_{i=0,\ldots,N_P-1} (N_P - i) \sum_{n=0}^{i} p_N(n). \tag{3.21}$$

It was shown in [29] that for a fixed length $L(r_i)$, an RO solution provides a good approximation of the DO solution and that the latter has a stronger protection than the former. A local search algorithm thus tries to improve an RO solution by an additional local searching in the neighborhood of this solution. This neighborhood is restricted to solutions that provide stronger protection. If a candidate in the neighborhood is better than the current solution, we adopt it and repeat the local search from the new solution. Otherwise, we stop.

Thus, starting with a fast computation of an RO solution to (3.19), a quick local search can be added to reach an approximation of a DO solution to (3.17). Then a fast joint optimization algorithm is proposed in [29] to solve the problem in (3.18). The idea is to alternately decrease the RCPC code rate and apply the local

search algorithm of [29]. Results in [29] show that the local search algorithm gives comparable PSNR performance to previous approaches [69, 70]. But it is significantly faster because it only needs to inspect a few RCPC code rates to reach a near-optimal solution.

C. Progressive Image Transmission over DSTC systems

Fig. 16 gives the overall block of the system. It consists of three main functional blocks: progressive Image Coding, JSCC and differential space-time coded OFDM (DSCT-OFDM) systems. The image is first fed into an embedded image encoder to generate one bitstream. The scalable property of the output bitstream requires a UEP scheme to guarantee the error robustness. And the bursty nature of errors in fading channels prompts the employment of RS code because of its good bursty error correction capability. And more powerful error protection can be achieved if another channel code (e.g., convolutional code) is applied perpendicularly to the RS codes. Based on this idea, one straightforward solution is the product code structure in [70]. Thus, the embedded bitstream is transformed into a sequence of packets in the product code structure by the RCPC/CRC and RS channel encoder. We then transmit all the packets via the DSTC-OFDM system. At the receivers, we decode the received symbols using decision-feedback differential detection. After channel decoding, parity checking is performed via CRC decoding. Once errors are found, the corresponding packet is considered to be decoded with errors. RS codes in the product code enable us to recover part of bitstream from the remaining packets. Note that only the bits before the first error in the bitstream can be used to reconstruct the transmitted image by the image decoder.

The main component of our image transmission system is the product code de-
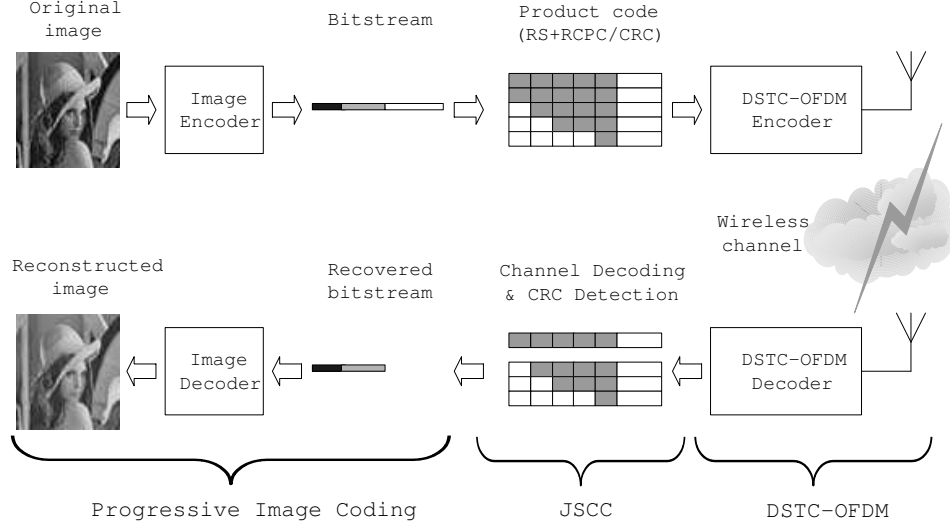
Fig. 16. Overall block of image transmission system over DSTC-OFDM systems.

sign, which is optimized by determining the best RS protection for each RCPC code rate. This is time-consuming when many RCPC code rates are allowed. A local search algorithm that jointly optimizes the RS and RCPC code is described in [29].

As introduced in Section B.3, the product code design requires two sets of parameters as inputs: the operational distortion-rate function of source coder $D(r_s)$ and the probability function $p_N(n)$.

The distortion-rate function is easy to generate by practically encoding and decoding the original image. That is, we encode the image at a given highest source rate and then decode the bitstream at different low rates. The probability function $p_N(n)$ is difficult to evaluate accurately by analytical methods. Given an average SNR of fading channels and a channel code rate $r_i \in \mathcal{R}$, we perform 1000 practical image transmissions over the STC-OFDM system and count $n_N(n)$, the number of trials where n out of N_P packets are with errors. Thus we can compute the probability function by $p_N(n) = n_N(n)/1000$.

Note that at high average SNR (hence low BER), channel coding is not necessary and more source bits together with RS redundancy symbols can be assigned to achieve better performance. Thus the candidate channel rates for the product code design are $\mathcal{R}' = \{1\} \cup \mathcal{R}$, where code rate 1 means no RCPC is applied.

Once the two sets of parameters are obtained, by employing the local search algorithm, we jointly optimize the RS and the RCPC codes to give the best design of product code. Then it is straightforward to compute the average MSE analytically by (3.18) and convert average MSE to PSNR performance by (2.21).

The process of performance analysis is summarized in Fig. 17.
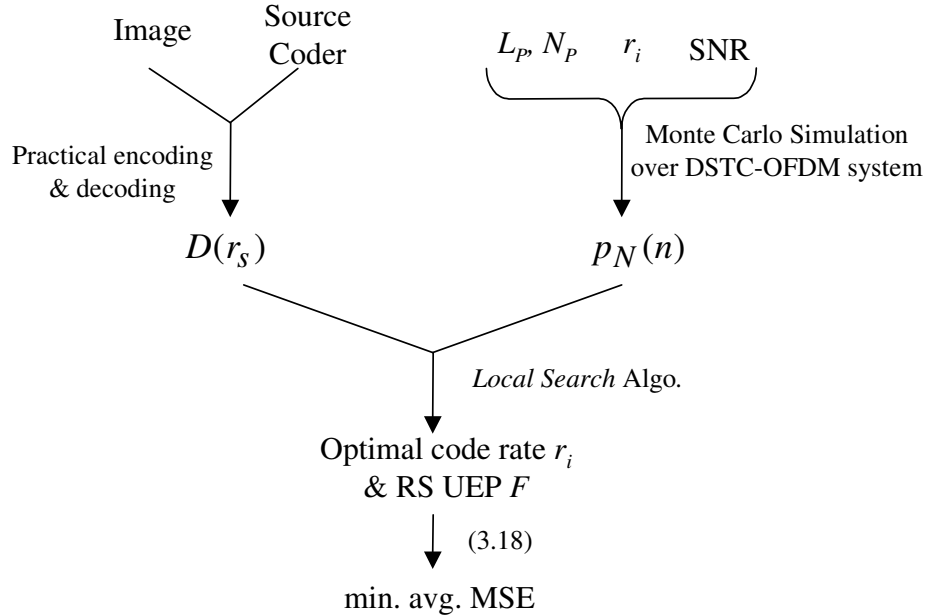
Fig. 17. Summarization of performance evaluation of the image transmission system over DSTC-OFDM systems. The two inputs of the local search algorithm are: the operational distortion-rate function of the image coder $D(r_s)$ and the probability of packet decoding error $p_N(n)$ for a certain RCRC rate.

D.   Iterative Decoding of Differentially Space-time Coded Multiple Descriptions of Images

1.   MD Source Coding via SPIHT+UEP

The MD source coder can be simply based on embedded coding (e.g., SPIHT [3]) and UEP [29, 71]. An example with two descriptions is given in Fig. 18 [75], where the embedded source coder is employed to produce a rate $(2 - \rho)R$ bitstream with $0 \leq \rho \leq 1$. The first ρR portion of the embedded bitstream is repeated in both descriptions, as indicated by the box, while the remaining $2(1 - \rho)R$ portion is split between the two descriptions. It is a clear UEP scheme since the first ρR portion of the bitstream is protected by a rate-1/2 channel code via repetition, while the remaining portion is not protected at all. Furthermore, MD coding can be viewed as means to introduce redundancy for error robustness. Thus, conceptually any practical JSCC scheme with soft threshold channel coding can be employed as the MD coder in our system.

Description 1	ρR	$(1 - \rho)R$
Description 1	ρR	$(1 - \rho)R$

Fig. 18. An example with two descriptions generated via embedded source coding and UEP.

In our scheme, the MDs are generated via the product code structure with RCPC/CRC and RS codes, as shown in Fig. 15. We choose RS codes along the columns because of their good capabilities to correct bursty errors from the fading channels. When compared with the example in Fig. 18, this structure shows an obvious UEP scheme and guarantees a successful MD coder with each packet (row) as

one description. Besides the RS codes along the columns, we also apply RCPC/CRC codes along the rows to further enhance the performance.

It is simple to generate MDs using the discussed product code design. But the major problem is how to optimize the product code by determining the best RS EPS for each RCPC rate. One efficient solution by using the local search algorithm [76] has been comprehensively discussed in previous sections.

2. An Iterative DSTC Decoding Algorithm in Fading Channels

Nguyen and Ingram have developed an iterative decoding algorithm in [86] by concatenating DSTC with a convolutional code, as shown in Fig. 19. The input bits are first encoded with the outer coder-a convolutional code. The coded bits are then interleaved and fed into the inner coder-DSTC to achieve the transmitter diversity. The recursive property of DSTC makes it a fitful inner coder in serial concatenation to achieve the interleaver gain. Furthermore, the recursive DSTC encoder has a trellis structure, which make it possible to perform decoding using the Viterbi algorithm or the BCJR algorithm [87].
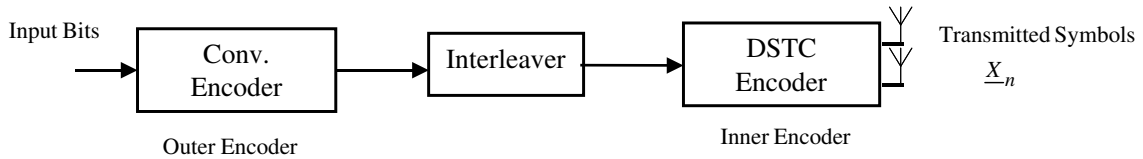
Fig. 19. Serial concatenated code of convolutional code and DSTC.

The proposed receiver consists of an MAP DSTC decoder (inner decoder) [86], a convolutional decoder (outer coder), an interleaver and a deinterleaver, as described in Fig. 20. The two decoders exchange extrinsic values or APP of transmitted bits between themselves in successive iterations. The DSTC demodulator has the channel

values and the APP as its inputs. The MAP decoder calculates the APP or the LLR of each of these extrinsic values. These values are then deinterleaved to bring them in the right order of the MD source decoder. Using these inputs, the convolutional decoder calculates the extrinsic values and passes them back to the MAP DSTC decoder through an interleaver. At the last iteration, the MD source decoder also outputs the estimations of the original input bits. Details of the receiver are discussed as in [86].
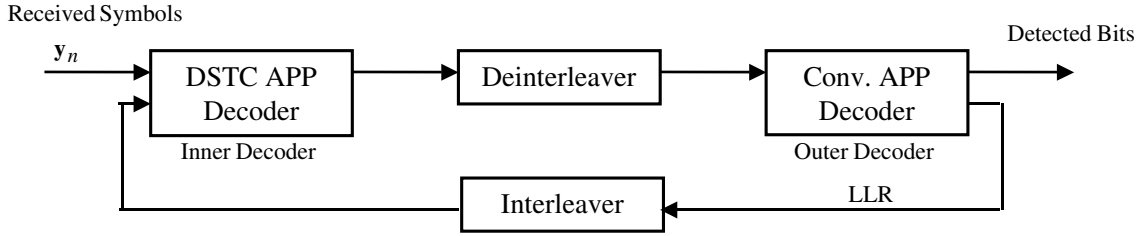
Fig. 20. Iterative decoding of serial concatenated code.

3.   Iterative Decoding of Differentially Space-Time Coded MDs of Images

We combine the outer MD code and the inner DSTC together for iterative decoding of MDs of images. The link that connects these two constituent codes is the RCPC coding component in the MD code (see Fig. 15). It plays the role of the outer convolutional code in the concatenated system of [86].

Our proposed image transmission system is shown in Fig. 21. First the original embedded image bitstream goes through the MD encoder (product code). After the interleaver, each description (packet) is encoded by DSTC and transmitted through the wireless channel. At the receiver, turbo decoding is performed based on the concatenation of the DSTC decoder, the deinterleaver, the RCPC decoder and the interleaver, as discussed in Section 2. Based on results in [86], we expect the turbo decoding performance to improve with successive iterations. After the transmission of

all the packets through the wireless channel and the channel decoding after a certain number of iterations, parity checking is performed via CRC decoding. Whenever an error is detected, the corresponding packet is considered to be decoded with errors. With the help of the RS code in the product code structure, we recover part of the source bitstream and reconstruct the original image by the SPIHT image decoder.
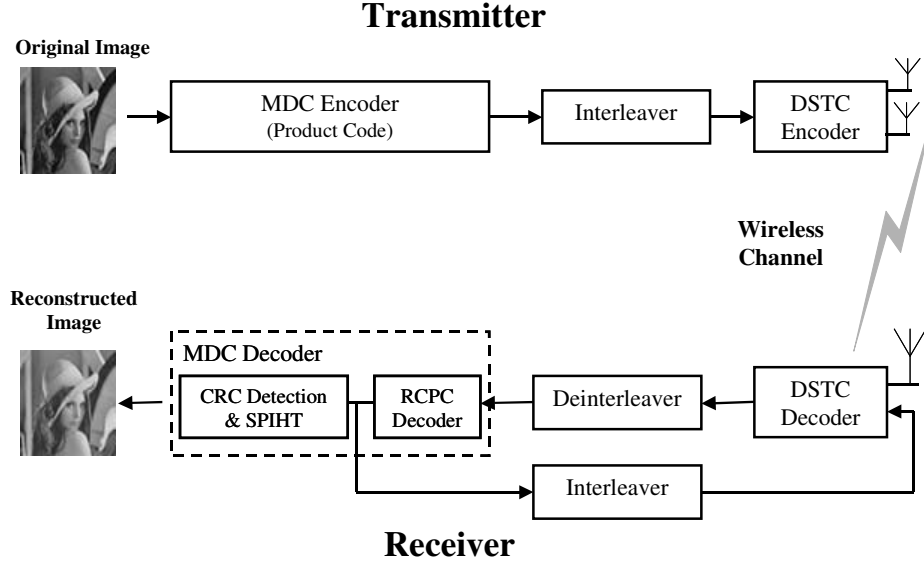
Fig. 21. Overall system of transmission of multiple descriptions of images through differential space-time coding.

This process of performance evaluation is similar with that in Section C, and can also be summarized in Fig. 17.

E.   Numerical Results and Discussions

1.   Progressive Image Transmission over DSTC-OFDM systems

In this section, we will present the numerical results to evaluate our proposed image transmission scheme over DSTC-OFDM systems. To give comprehensive comparisons, we also give the simulation results for coherent detection and EM-based iterative receiver.

The STC-OFDM systems introduced in previous sections are simulated using QPSK modulator. A 3-tap frequency-selective channel with equal power between each pair of transmit and receive antenna is assumed. And each tap of channel is modelled as a flat-fading channel with normalized doppler shift $f_D T_s = 0.01$. The number of sub-carriers in the OFDM system is $K = 128$.

We transmit the 512×512 Lena image through these systems. The SPIHT [3] image coder is used to compress the image to generate an embedded source bitstream. The bitstream is then transformed into the product code structure with the packet length $L_P = 64$ Bytes. Two transmission rates, i.e., 0.5 and 1 bit per pixel (bpp), are considered in our work with the number of packets $N_P = 256$ and $N_P = 512$, respectively. In each packet, a 16-CRC code with generator polynomial 0x15935 is applied to detect the error. And for the RCPC codes, the generator polynomials were $(0117, 0127, 0155, 0171)$, the mother code rate was 1/4, and the puncturing rate was 8. Thus, the set of RCPC rates is $\mathcal{R} = \{8/9, 8/10, \ldots, 8/32\}$ and the candidate RCPC rates for the product code design are $\mathcal{R}' = \{1\} \cup \mathcal{R}$. The decoding of the RCPC code is done with a list Viterbi algorithm where the maximum number of candidate paths is 100.

Below we show the experimental results in two parts: BER performance of STC-OFDM systems and reconstructed image qulity in PSNR.

a.   BER Performance

BER performance of the DSTC-OFDM system with $N_T = 2, N_R = 1$ and different window sizes are shown in Fig. 22 (a) in solid curves. It is natural to see the error floor for conventional DSTC decoding algorithm (i.e., window size $N = 2$). Except for a little performance loss when SNR<10 dB, decision-feedback method (denoted by "DF-DSTC") is truly an efficient way to reduce the error floor for SNR>20 dB. From Fig. 22 (a), we also find that the major gains can be achieved with moderate observation window size N, i.e., the gaps between the BER curves become smaller and smaller with the increase of N. Similar observations are reported in [28]. This property allows us to achieve good performance without using large window sizes with prohibitive complexity.

In Fig. 22 (a), we see a gap of about 3 dB between the DF-DSTC decoding (in solid curves) and coherent detection with perfect CSI (denoted by "CD-STC", in dashed curves) for SNR<20 dB when error floor is almost absent. This agrees with the analysis in [24]. Fig. 22(a) also plots BER performance of EM-based iterative receiver (denoted by "EM-STC", in diamond solid curves), which is about 2.5 dB better than that of DF-DSTC when SNR<20 dB. With the increase of SNR, the gap becomes larger and larger because the effect of error floor is more obvious for DSTC. Note that we should adjust SNR for EM-STC to perform fair comparisons with DSTC since we lose some rate when inserting pilot symbols.

Finally, BER performances of the systems with more receive antennas ($N_R = 2$) are plotted in Fig. 22 (b). We can make similar observations when comparing with the case of a single receive. And it is not surprising to see that more diversity gains are obtained with more receive antennas.
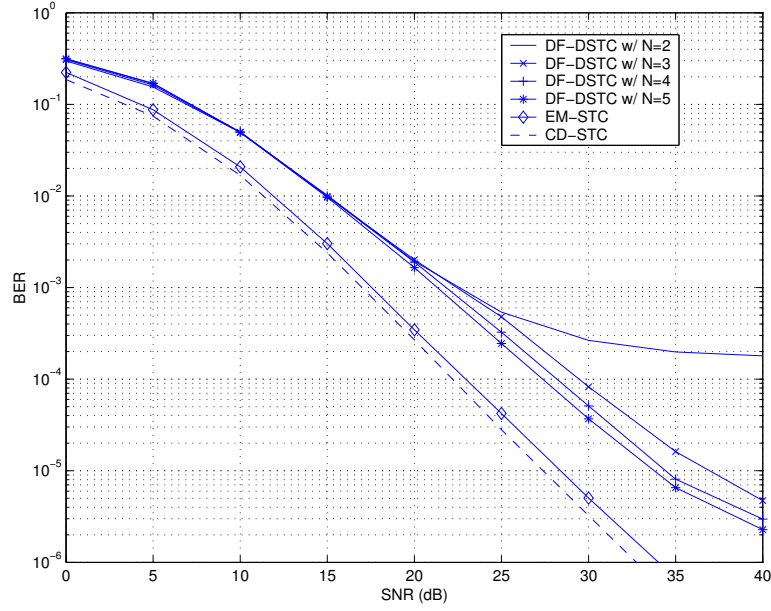
(a) $N_T = 2, N_R = 1$
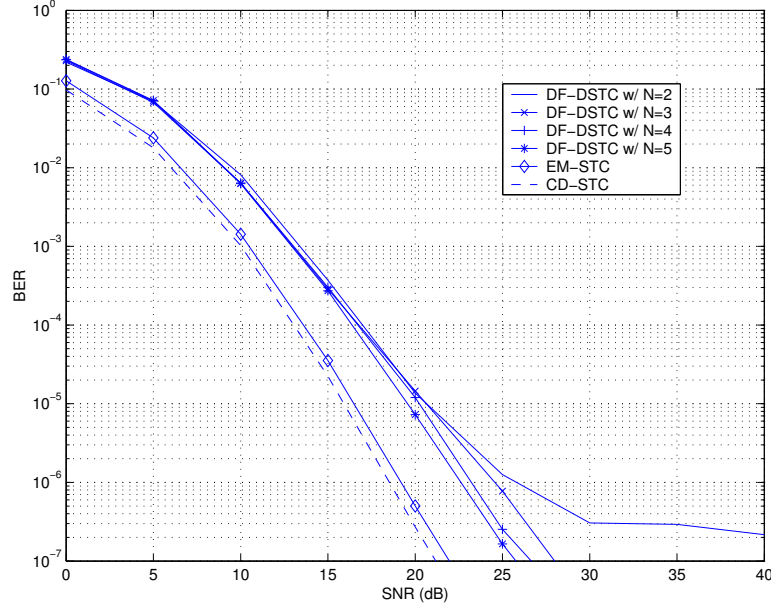
(b) $N_T = 2, N_R = 2$

Fig. 22. BER performances of QPSK-modulated STC-OFDM systems with $N_T = 2$ transmit antennas and (a) $N_R = 1$ and (b) $N_R = 2$ receive antennas. The normalized doppler shift $f_D T_s = 0.01$. And the number of sub-carriers in the OFDM system is $K = 128$. N denotes the observation window size used in DF-DSTC; For EM-STC, we choose the number of OFDM slots in one STC codeword $P = 2$, the number of STC codewords in one data burst $q = 5$, the number of EM iterations $I = 5$.

b.   Reconstructed Image Quality

Fig. 23 plots the reconstructed image quality (in PSNR) vs. SNR performance of STC system with $N_T = 2, N_R = 1$. Two transmission rates, i.e., 0.5 and 1 bpp, are considered. It is seen that the improvements of BER performance in our systems can be translated into quality gains in reconstructed images. With the increase of SNR, the PSNR results of all the systems approach the limit given by source coding. Corresponding to BER performance in Fig. 22, we find that when BER$< 10^{-5}$, PSNR curves will reach a plateau and no much gains can be obtained by increasing the SNR.

At the transmission rate of 0.5 bpp, the PSNR results of DF-DSTC systems with various observation window sizes are shown in the solid curve ($N = 5$) and the dashed curve ($N = 2$) in Fig. 23 (a). For larger window size ($N = 5$), when SNR$>$20 dB, the contribution to reduce the error floor will lead to a 0.6 dB higher PSNR limit. That is, the reduction of error floor enables us to achieve the best reconstructed image quality given a certain transmission rate. Note that the error floor in the BER performance of DSTC is determined by the Doppler frequency. For higher Doppler frequencies, the error floor will be more pronounced, which leads to more performance loss for the reconstructed image. Fig. 23 (a) also shows the PSNR performance of coherent detection and EM-based iterative decoding schemes. Comparing to EM-STC, we see some performance loss in PSNR results for DF-DSTC at low SNRs. But this loss becomes smaller and smaller with the increase of SNR.

When the transmission rate is increased to 1 bpp, as shown in Fig. 23 (b), we observe almost the same performance loss in PSNR at low SNRs when comparing to the case with the low transmission rate. However, the overall improvement of PSNR values will mitigate the visual difference of the reconstructed image, as illustrated in Fig. 24. On the other hand, the degradation in image quality with decision-feedback
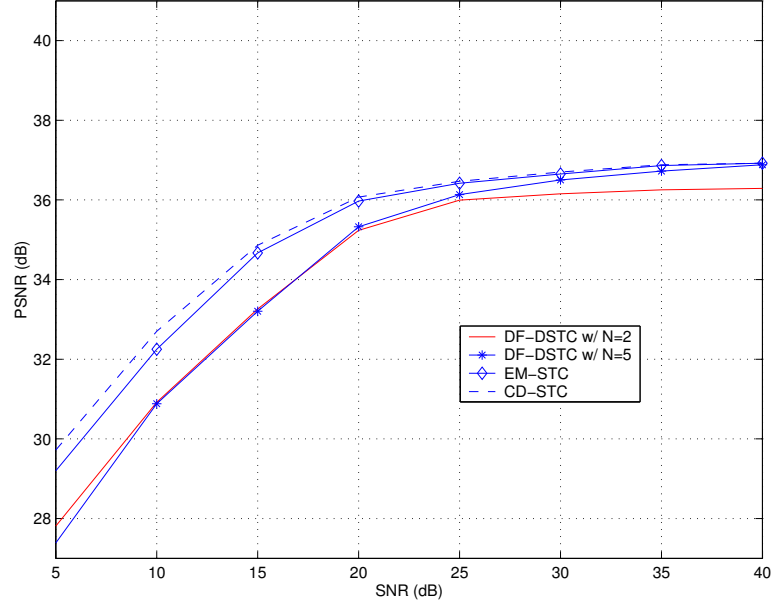
(a) 0.5 bpp
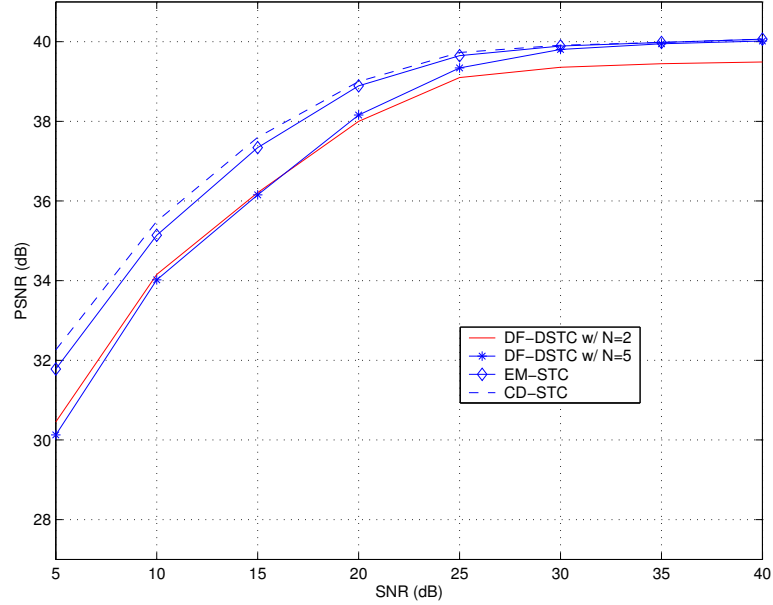
(b) 1 bpp

Fig. 23. PSNR Reconstructed image quality in PSNR (dB) of the image transmission system over the QPSK-modulated STC-OFDM system with $N_T = 2, N_R = 1$. A product code structure with the packet length $L_P = 64$ Bytes is assumed. Two different numbers of packets, $N_P = 256$ and $N_P = 512$, are considered, which lead to the transmission rates of (a) 0.5 bpp and (b) 1 bpp, respectively. Various detection schemes (i.e., CD-STC, EM-STC and DF-DSTC) are assumed. Other parameters are the same with those in Fig. 22.

(a) DF-DSTC, 0.5 bpp, PSNR=27.38 dB   (b) EM-STC, 0.5 bpp, PSNR=29.20 dB

(c) DF-DSTC, 1 bpp, PSNR=30.12 dB   (d) EM-STC, 1 bpp, PSNR=31.78 dB

Fig. 24. Reconstructed images of Lena over the STC-OFDM system with $N_T = 2$ transmit antennas and $N_R = 1$ receive antenna when SNR=5 dB, using DF-DSTC at the transmission rates of (a) 0.5 bpp and (c) 1 bpp; and using EM-STC at the transmission rates of (b) 0.5 bpp and (d) 1 bpp.

differential decoding is offset by its computational simplicity. DF-DSTC decoding technique is a very efficient and simple way to handle the case without CSI at the receiver, while the complicated EM-based iterative receiver is time consuming and not easy to design, especially for hardware implementation. Thus, DF-DSTC decoding can be a good solution when the channel is not too noisy.

From Fig. 25, the diversity gains with more antennas can make the reconstructed image quality approach the PSNR limit sooner. This is another efficient way to reduce the performance gap between DF-DSTC and EM-STC, e.g., at SNR=15 dB. In Fig. 26, we also show the visual difference of the reconstructed image after the transmission over the STC-OFDM system with $N_T = 2, N_R = 2$ at a quite low SNR=5 dB. We see that difference becomes even smaller when comparing to the single-receiver STC-OFDM system.

Fig. 25 (a) includes the results from a related work of [9] (refer to Fig. 14 (b) in [9], where "MDC-SPIHT" denotes the multiple SPIHT sub-bitstream transmission). The significant performance gains show the effectiveness of the JSCC scheme in our system.
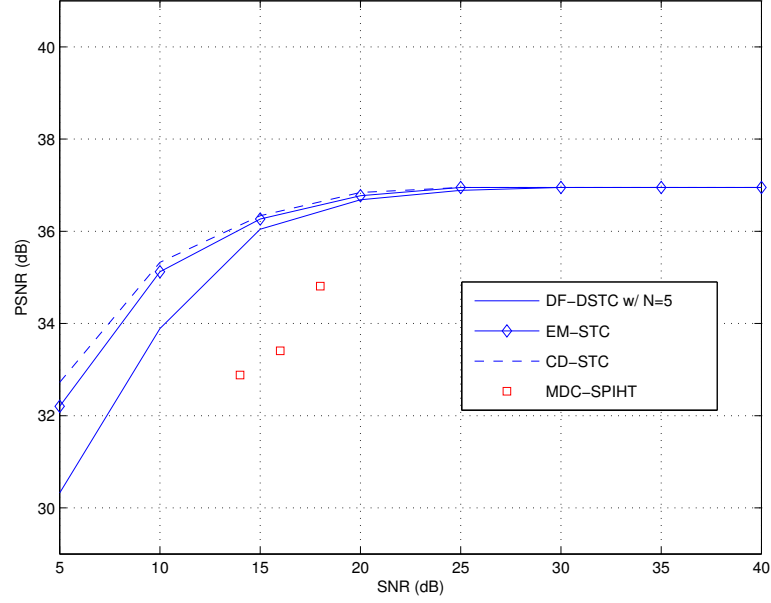
(a) 0.5 bpp
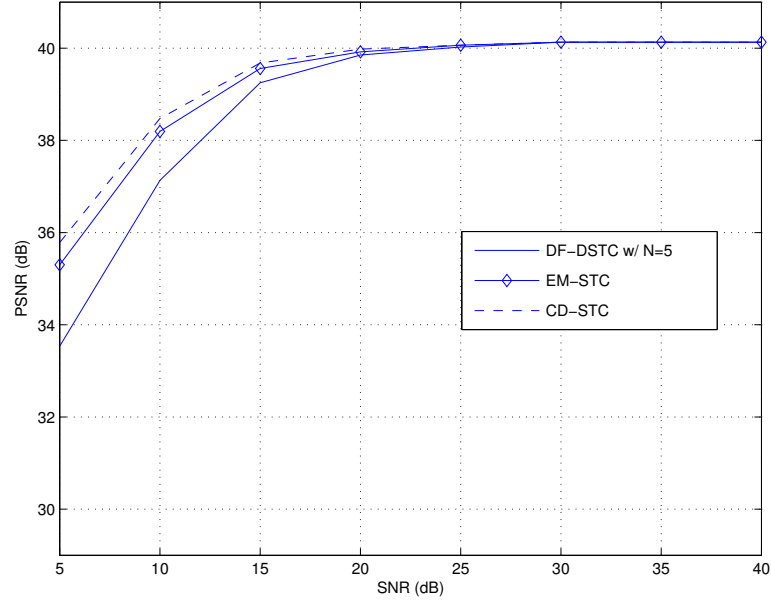
(b) 1 bpp

Fig. 25. PSNR Reconstructed image quality in PSNR (dB) of the image transmission system over the QPSK-modulated STC-OFDM system with $N_T = 2, N_R = 2$. A product code structure with the packet length $L_P = 64$ Bytes is assumed. Two different numbers of packets, $N_P = 256$ and $N_P = 512$, are considered, which lead to the transmission rates of (a) 0.5 bpp and (b) 1 bpp, respectively. Various detection schemes (i.e., CD-STC, EM-STC and DF-DSTC) are assumed. Other parameters are the same with those in Fig. 22.

(a) DF-DSTC, 0.5 bpp, PSNR=30.32 dB   (b) EM-STC, 0.5 bpp, PSNR=32.20 dB

(c) DF-DSTC, 1 bpp, PSNR=33.53 dB   (d) EM-STC, 1 bpp, PSNR=35.30 dB

Fig. 26. Reconstructed images of Lena over the STC-OFDM system with $N_T = 2$ transmit antennas and $N_R = 2$ receive antenna when SNR=5 dB, using DF-DSTC at the transmission rates of (a) 0.5 bpp and (c) 1 bpp; and using EM-STC at the transmission rates of (b) 0.5 bpp and (d) 1 bpp.

2.   Iterative Decoding of Differentially Space-time Coded MDs of Images

For the sake of simplicity, we simulated our proposed scheme for iterative decoding of the MDs of images by assuming BPSK modulation and a flat-fading channel with Jake's correlation structure [66] and normalized Doppler shift $f_D T = 0.01$. Note that for the differential detection, this high-mobility channel may result in an error floor even when AWGN is absent. However, in the low SNR range, e.g., 0-20 dB, which is our interest, the error floor is much less pronounced.

We consider transmitting the 512×512 grayscale Lena image. The SPIHT coded bitstream of Lena first goes through the product code to generate MDs with the number of packets $N = 200$ and the packet length $L = 48$ Bytes. Thus the transmission rate is about 0.29 bits per pixel (bpp). In each packet, a 16-CRC code is applied to detect the error. And the set of RCPC rates is $\mathcal{R} = \{8/9, 8/10, \ldots, 8/48\}$. For a given number of iterations (with three being the maximum), we evaluate the system by its average PSNR performance.

The SNR vs. average PSNR performance of the proposed system is tabulated in Table II, where "`Iter.0`" denotes the first decoding process without feedback of APP from the convolutional decoder to the DSTC decoder (see Fig. 20). We observe a PSNR gain of about 0.3~1.2 dB with three iterations in the 0-20 dB SNR range. Thus iterative decoding is an effective scheme to improve the PSNR performance. To give a clear comparison, we plot the PSNR results in Fig. 27. One important observation is that slight performance gains are achieved for more than one iteration. We think that the moderate increase in decoding complexity is a worthwhile investment for improved system performance. We also see that with the increase of SNR, the gaps between the curves of various iteration numbers become smaller and smaller. Thus, our iterative decoding scheme works better in low SNR or bad channel conditions.

Table II. Comparisons of PSNR performance for various numbers of iterations.

SNR	PSNR (dB)			
(dB)	Iter. 0	Iter. 1	Iter. 2	Iter. 3
0	24.54	25.63	25.85	26.17
5	29.49	30.13	30.43	30.49
10	31.94	32.81	32.96	33.09
15	33.17	33.52	33.54	33.60
20	33.64	33.89	33.89	33.90
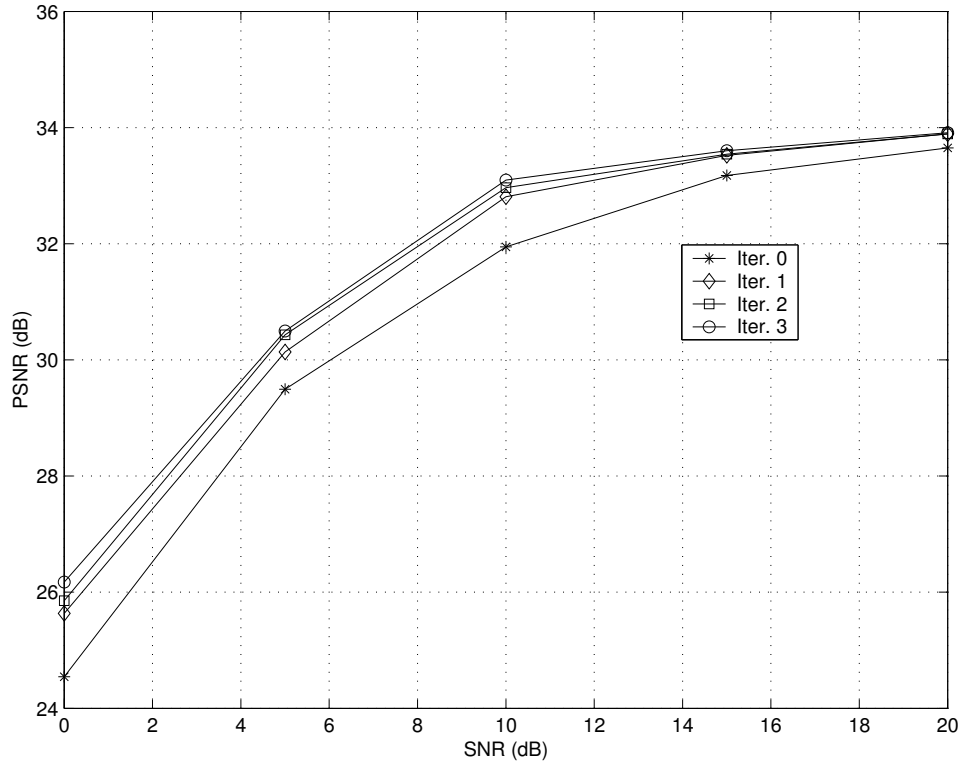
Fig. 27. Transmitted image qualities (in PSNR) of our proposed system.

F. Conclusions

The work in this chapter is one extension of that in Chapter II within a scenario much closer to the real application. In details, we describe an end-to-end image communication system that combines JSCC and physical-layer wireless communication techniques (e.g., DSTC and OFDM). Experiments show that SNR/BER improvements can be translated into quality gains in reconstructed images. Moreover, compared to the another non-coherent detection algorithm, i.e., EM-based iterative receiver, differentially space-time coded OFDM systems suffer some quality loss in reconstructed images. With the efficiency and simplicity of decision-feedback differential decoding, differentially space-time coded OFDM is thus a feasible modulation scheme for applications such as wireless image over mobile devices (e.g., cell phones).

We also make a seamless connection between the above image transmission system over wireless fading channels with the MD coding, and use iterative (turbo) decoding techniques developed for serially concatenated coding systems to improve the performance of the receiver in successive decoding iterations. We treat MD coding, realized by embedded image coding plus unequal error protection (e.g., product code structure), as the outer constituent code and use a differential space-time code as the inner constituent code. Experimental results show that our iterative scheme can effectively improve the system performance. Furthermore, most of the gain in PSNR is achieved with only one iteration in the low SNR range, e.g., 0-20 dB.

CHAPTER IV

DIRTY-PAPER CODE DESIGN: A SOURCE-CHANNEL CODING APPROACH

A.   Introduction

Another research topic related to source-channel coding, Costa ("dirty-paper") coding, will be covered in this chapter. We first invoke an information-theoretical interpretation of algebraic binning for CCSI to justify our source-channel coding based approach. Then, building upon results in [47, 34], we state that the performance loss (in SNR) in our practical code designs is the sum of the *packing loss* $\Delta\mathrm{SNR_p}$ from channel coding and a *modulo loss* $\Delta\mathrm{SNR_m}$, which is a function of both the granular loss from source coding and the target rate (or SNR). At high rate, the modulo loss is approximately equal to the granular loss, but as the rate decreases, it becomes higher and higher than the granular loss. Thus, besides advanced channel codes, it is imperative to employ strong source codes so that the granular loss is small for near-capacity dirty-paper coding, especially at low rate.

Following this guideline, we propose two practical Costa code designs which flavor different embedding rate regions.

1. **Nested turbo code** for high and medium rates ($\geq$ 1.0 bit/sample): This approach is proposed based on high-dimensional nested lattice codes [34] that partitions a channel code into source codes [43]. Compared to the implementations reported in [43, 44], we are able to realize a better matching of the employed source and channel codes in terms of their equivalent lattice dimensions, and hence achieve better performance. Specifically, we propose a nested turbo scheme using TTCM [49] as the channel code and a source code based

on soft-output TCQ (SOTCQ) [88]. Such a turbo-like source code is chosen because it has a similar parallel concatenated code structure as used in the TTCM [49] channel code. This property facilitates the nesting of the source code inside the channel code. In our implementation, we take into account both parallel branches of the source code in quantizing the side information, thus effectively constructing a good TCQ-like source code. We show that, depending on the percentage of samples processed by one of the parallel branches in our nested turbo code, there exists a tradeoff between the turbo-like TCQ source code and the TTCM channel code. Optimizing this tradeoff offers a means of balancing the dimensionalities of the source and the channel codes.

2. **Code design based on TCQ and IRA codes** for low embedding rates (< 1.0 bit/sample): The algebraic message-based binning interpretation of Costa coding indicates that one can shoot for the granular gain via source coding and the packing gain via channel coding. In practice, the former should be done with powerful quantizers (e.g., TCQ [35]) having almost spherical Voronoi cells in a high-dimensional Euclidean space, and the latter with near-capacity channel codes (e.g., IRA codes [52]). This justifies our combined source-channel coding approach to dirty-paper coding based on TCQ and IRA codes. Treating TCQ as a form of lattice VQ, we seamlessly combine TCQ with both non-systematic and systematic IRA codes in a source-channel coding setup without sacrificing the performance of either component, i.e., both the TCQ and IRA code components still work well when combined together in our elaborate dirty-paper code construction. This is one main advantage over the nested turbo approach where we see the obvious constraint between source coding and channel coding in terms of their individual performance. Thus, our scheme based on TCQ and

IRA codes comes closer to the Costa limit at low rates. However, this scheme cannot straightforwardly be applied to the high rate regime, and whether or not they can be redesigned to operate well at high embedding rate is not clear.

This chapter is organized as follows. In Section B, we review the background knowledge on Costa coding and motivate our code design guideline. Following this guideline, the nested turbo code and the code design based on TCQ and IRA codes are proposed in Section C and Section D, respectively. Then the efficiency of our proposed schemes is evaluated via simulation in Section E. Finally, we draw the conclusions and suggest the future work in Section F.

B.   Background and Motivations

1.   Nested Lattice Code Construction

Although Costa's proof shows the existence of capacity-achieving random binning schemes, it does not give any indication about practical code construction. Zamir *et al.* [34] suggested an algebraic binning scheme based on nested lattice codes. The scheme consists of a coarse lattice code nested within a fine lattice code. The fine lattice code needs to be a *good* channel code and the coarse lattice code needs to be a *good* source code to approach the capacity in (1.2).

Fig. 28 (a) illustrates 1-D nested lattice/scalar codes with an infinite uniform constellation, where Δ denotes the step-size. The channel codewords are grouped into cosets/bins (labeled as 0, 1, 2, and 3) for source coding. At the encoder, the side information S is linearly scaled by α [30] and quantized to U by the source code selected by the message m to be transmitted (e.g., the coset/bin labelled 1 in Fig. 28 (b)), so that the obtained quantization error $X = U - \alpha S$ satisfies the power constraint $E[X^2] \leq P_X$. Then, X is transmitted over the additive white Gaussian noise channel

with noise $Z \sim N(0, P_Z)$. According to [30], the optimal $\alpha = \frac{P_X}{P_X + P_Z} = \frac{\text{SNR}}{\text{SNR}+1}$, with SNR$=\frac{P_X}{P_Z}$. The decoder (see Fig. 28 (c)) receives the signal $Y = X + S + Z$, scales it by α, and finds the codeword $\hat{U}$ closest to αY. Finally the index of the bin containing $\hat{U}$ is identified as the decoded message.

(a) Binning Scheme

(b) Encoding
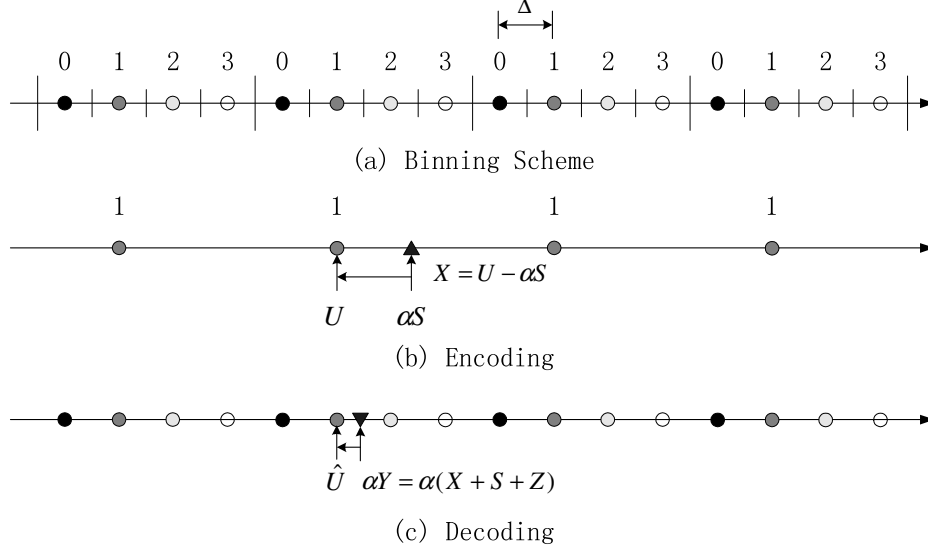
(c) Decoding

Fig. 28. 1-D nested lattice codes for Costa coding.

It is shown in [34] that this nested scheme approaches the capacity in (1.2) as the dimensionality of the employed lattices approaches infinity. However, nested lattice coding calls for a joint source-channel code design, typically with the same dimensional coarse lattice source code and fine lattice channel code, which are difficult to implement in high dimensions.

2. Lattice Precoding and Achievable Rates

Let Λ be an n-dimensional lattice quantizer with basic Voronoi cell $\mathcal{V}$. Associated with $\mathcal{V}$ are several important quantities: the cell volume $|\mathcal{V}|$, the second moment $P(\Lambda)$, and the normalized second moment $G(\Lambda)$, defined by $|\mathcal{V}| = \int_{\mathcal{V}} d\mathbf{x}$, $P(\Lambda) = \frac{1}{n|\mathcal{V}|} \int_{\mathcal{V}} |\mathbf{x}|^2 d\mathbf{x}$,

and $G(\Lambda) = P(\Lambda)/|\mathcal{V}|^{\frac{2}{n}}$, respectively. The minimum of $G(\Lambda)$ over all n-dimensional lattices is denoted as G_n. $G_n > \frac{1}{2\pi e}, \forall n$ and $\lim_{n \to \infty} G_n = \frac{1}{2\pi e}$. The granular gain of Λ is $g(\Lambda) = -10 \log_{10} 12G(\Lambda)$, which is maximally 1.53 dB. Denote $\mathbf{D}$ as the random dither uniformly distributed over $\mathcal{V}$.

For any source codewords (or constellation points) $\mathbf{u} \in \mathcal{V}$, the encoder transmits

$$\mathbf{X} = [\mathbf{u} - \alpha\mathbf{S} - \mathbf{D}] \bmod \Lambda,$$

while the decoder receives $\mathbf{Y} = \mathbf{X} + \mathbf{S} + \mathbf{Z}$ and computes

$$\mathbf{Y}' = [\alpha\mathbf{Y} + \mathbf{D}] \bmod \Lambda = [\mathbf{u} + \mathbf{N}'] \bmod \Lambda,$$

where α is a scaling factor and

$$\mathbf{N}' \triangleq [(1 - \alpha)\mathbf{D} + \alpha\mathbf{Z}] \bmod \Lambda$$

is the equivalent *modulo lattice channel noise.*

The maximum achievable rate of the modulo lattice channel is $\frac{1}{n}I(\mathbf{U}; \mathbf{Y}')$, achieved by a uniformly distributed input $\mathbf{U}$ over $\mathcal{V}$. Due to the dither $\mathbf{D}$, $\mathbf{X}$ is independent of $\mathbf{u}$ and uniformly distributed over $\mathcal{V}$ with $E[||\mathbf{X}||^2] = P_X = P(\Lambda)$. Then, for $n > 1$, $\frac{1}{n}I(\mathbf{U}; \mathbf{Y}')$ can be lower bounded by assuming $\mathbf{D}$ has *i.i.d. Gaussian components* and using the MSE-optimal $\alpha = \frac{P_X}{P_X + P_Z} = \frac{\text{SNR}}{\text{SNR}+1}$ [30], yielding [47]

$$\frac{1}{n}I(\mathbf{U}; \mathbf{Y}') \geq \frac{1}{2}\log_2(1 + \text{SNR}) - \frac{1}{2}\log_2 2\pi eG(\Lambda). \tag{4.1}$$

Note that for any finite n, the components of $\mathbf{D}$ (and $\mathbf{X}$) are not Gaussian or independent. In practice, n has to be high for the i.i.d. Gaussian assumption to be approximately true and for the lower bound in (4.1) to be tight.

3.   Motivations of the Proposed Code Designs

We offer an algebraic *message-based binning* interpretation of dirty-paper coding in terms of source-channel coding in [33]. From an information-theoretical perspective, there are granular gain and boundary gain in source coding, and packing gain and shaping gain in channel coding. Dirty-paper coding is primarily a channel coding problem (for transmitting messages), one should consider the packing gain and the shaping gain. In addition, the side information necessitates source coding to satisfy the power constraint, i.e., the constellation needs to be infinitely replicated so that one can quantize the side information to satisfy the power constraint [34]. Thus source coding in dirty-paper coding is not conventional in the sense that there is only granular gain, but no boundary gain. One needs to establish the equivalence between the shaping gain in channel coding and the granular gain in source coding for dirty-paper coding. Then one can shoot for the shaping gain via source coding and the packing gain via channel coding.

The rate bound (4.1) indicates that with ideal channel coding, the loss in rate due to lattice quantization (or source coding) is maximally $\frac{1}{2}\log_2 2\pi eG(\Lambda)$ bit/sample. With practical channel coding, there is an additional packing loss $\Delta\mathrm{SNR}_\mathrm{p}$ (in dB). In order to measure the losses from both source coding and channel coding in decibels, following [89], we define the *modulo loss* (in dB) corresponding to the lower bound in (4.1) due to the modulo operation in lattice quantization as

$$\Delta\mathrm{SNR}_\mathrm{m} \triangleq 10\log_{10}\frac{\mathrm{SNR}}{\mathrm{SNR}^*} = 10\log_{10}\frac{2\pi eG(\Lambda)2^{2C^*}-1}{2^{2C^*}-1}, \qquad (4.2)$$

where $\mathrm{SNR}^* = 2^{2C^*}-1$ is the capacity-achieving SNR.

When the rate C^* is high, $\Delta\mathrm{SNR}_\mathrm{m} \approx 10\log_{10}2\pi eG(\Lambda) = 1.53 - g(\Lambda)$ dB, i.e., the modulo loss is approximately equal to the granular loss from source coding in

this case. But as the rate C^* decreases, Fig. 29 indicates that the modulo loss ΔSNR_m increases when $G(\Lambda)$ is fixed. To reduce ΔSNR_m, it is imperative to use high-dimensional lattice quantizers (or VQ in general) to achieve as much granular gain as possible so that $2\pi e G(\Lambda)$ approaches one. At $C^* = 0.25$ bit/sample, when the granular gain $g(\Lambda)$ of Λ is 1.22, 1.28, 1.33, 1.36, 1.38 and 1.40 dB, ΔSNR_m equals 0.98, 0.81, 0.65, 0.56, 0.49 and 0.43 dB, respectively. This highlights the importance of having a strong source code in dirty-paper coding, especially at low rate. Thus, the practical performance loss ΔSNR (in dB) in our designs is the sum of the packing loss ΔSNR_p due to IRA codes and the modulo loss ΔSNR_m due to TCQ, i.e.,

$$\Delta SNR = \Delta SNR_p + \Delta SNR_m. \tag{4.3}$$
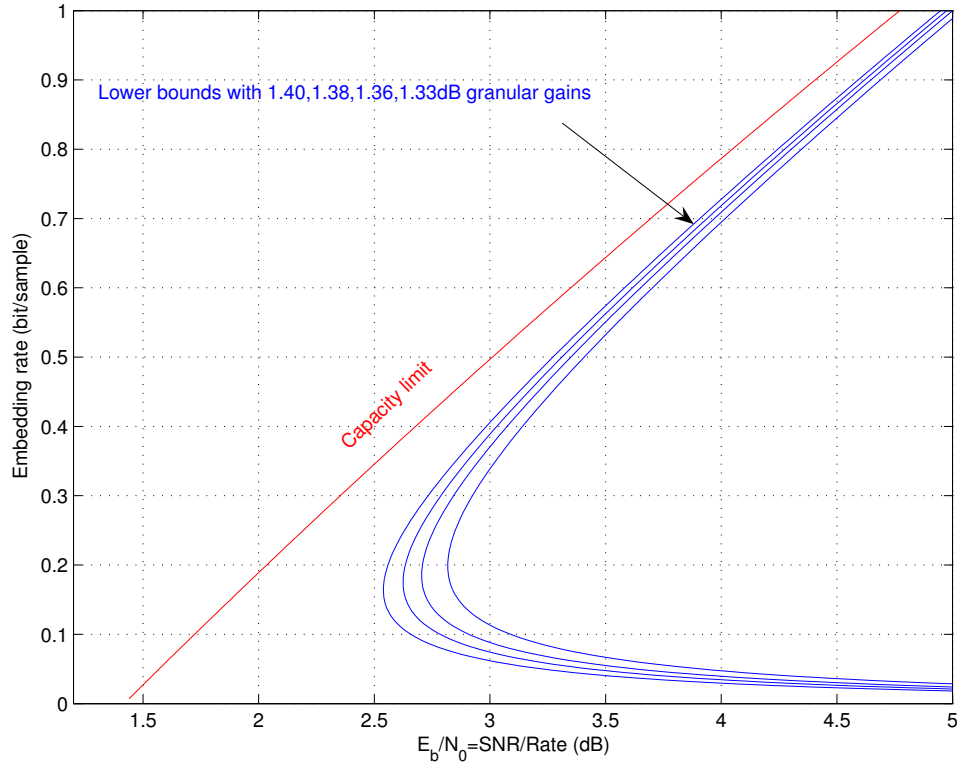
Fig. 29. The dirty-paper capacity limit and the lower bound in (4.1) for $g(\Lambda) = 1.40, 1.38, 1.36$ and 1.33 dB. It is seen that as the rate decreases, the modulo loss ΔSNR_m increases for fixed $G(\Lambda)$.

With (4.3), the aim of Costa code design is now clear: one needs to employ both strong source and channel codes so that the *total* loss is minimized. In addition, once the source and channel codes are chosen, one can obtain the expected performance of the resulting Costa code, provided that the source code is strong, i.e., the granular loss 1.53-$g(\Lambda)$ is small. This automatically precludes the scalar Costa scheme [45] from approaching the capacity. Conversely, once the performance of a Costa code is known, one can separately measure $\Delta \text{SNR}_\text{m}$ due to source coding from (4.2), where $G(\Lambda)$ is replaced by the MSE distortion P_X introduced by the quantizer, and the packing loss $\Delta \text{SNR}_\text{p}$ due to channel coding. These are the guidelines we follow in the practical code constructions below.

C. Nested Turbo Code Construction

According to [34] and (4.3), a nested lattice code can asymptotically approach the capacity of Costa coding in (1.2) when the dimensionality of the employed lattices (for source coding and channel coding) goes to infinity. However, the bad news is that, whereas recent progresses in iterative decoding of graph-based turbo/LDPC codes have made it possible to implement equivalent lattice channel codes of very high dimensions (e.g., in the thousands), such progresses have not yet been mirrored in source coding. For example, a recent attempt on turbo TCQ [88] has resulted in worse results than TCQ, which can perform roughly the same as a 69-th dimensional lattice source code with 0.2 dB of granular loss [4]. The performance difference [32] between lattice codes for source and channel coding due to this fundamental "dimensionality mismatch" explains the main difficulty involved in practical Costa code design. It also makes it almost impossible to implement high-dimensional nested codes with the same dimensional lattice source and channel codes. But the good news is that two things

work to our favor. First, for two lattices to be nested, they do not have to be of the same dimensionality (e.g., a Z-lattice can be nested in any construction-A lattice as the coarse-fine lattice pair [90]); second, although advanced source coding techniques such as TCQ can only reach about 69-th dimension (in terms of lattice source code), the small 0.2 dB granular loss of TCQ is acceptable in practical applications. Thus, our main task in Costa code design is to find the best nesting between the strongest practical source and channel codes.

In this approach, we study practical Costa code designs based on high-dimensional nested lattice codes [34] under the framework of nesting (or binning) that groups channel codewords into source codes. Compared to the implementations reported in [43, 44], we are able to realize a better matching of the employed source and channel codes in terms of their equivalent lattice dimensions and hence achieve better performance. Specifically, we propose two means of alleviating the severity of the dimensionality mismatch. First we propose a novel approach that uses SOTCQ as the source code in conjunction with TTCM as the channel code. The turbo-like SOTCQ is chosen as the source code because it has a similar parallel concatenated code structure as used in the TTCM channel code. This property facilitates the nesting of the source code inside the channel code. In our implementation, we take into account both parallel branches of the source code in quantizing the side information, thus effectively constructing a good TCQ-like source code. In terms of equivalent lattice code dimensions, SOTCQ is of higher dimension than TCQ and hence for our scheme, the extent of the dimensional mismatch is inherently lower than that of [43, 44].

We then propose an additional means of balancing the dimensionalities of the equivalent lattices of the employed source and channel code. The nested turbo scheme of [43, 44] processes exactly half of the samples in one of the parallel branches of the channel code. We show that, depending on the percentage of samples processed

by one of these parallel branches, there exists a tradeoff between the TCQ/SOTCQ source code and the TTCM channel code. Optimizing this tradeoff offers a means of *dimensionality balancing.* Our simulations indicate promising results at moderate to high embedding rates. At rates of 2.0 bit/sample and 1.0 bit/sample, our scheme significantly outperforms those of [91] and [43, 44], respectively. At lower rates (e.g., 0.5 bit/sample), however, because of the nesting constraint in our code design that introduces strong coupling between the source and channel codes, our scheme performs only moderately well, although it still outperforms that of [91].

1.   The SOTCQ/TTCM scheme

Before introducing our nested lattice coding scheme based on SOTCQ/TTCM, we first briefly describe the nested turbo scheme of [43], which uses TCQ as the source code and TTCM as the channel code.

The trellis structure in [43] is constructed via a rate-$k/n/m$ concatenated code (denoted by C_1+C_2, with C_1 being the rate-k/n convolutional code and C_2 being the rate-n/m convolutional code). The message to be transmitted $\mathtt{m}$ is used to shift the codewords of C_1 by a fixed amount and select a source code for quantization. TTCM consists of a parallel concatenated code with convolutional code C_2 in both parallel branches. C_2 in the bottom branch is preceded by an n-bit symbol interleaver and followed by an m-bit symbol deinterleaver. The two branches are multiplexed by taking the even samples of the codeword from the top branch and the odd samples from the bottom branch (an even-odd multiplexing which processes exactly half of the total samples in a single parallel branch). At the decoder, the received signal is decoded to the closest codeword, and the n-bit input sequence of C_2, i.e., the codeword of C_1, is recovered. Finally, the transmitted message is reconstructed by calculating the syndrome of the recovered codeword of C_1.

The key issue in encoding is to determine the n-bit input sequence to the TTCM encoder, which is denoted by $\vec{I}_2 = [I_2(0), \ldots, I_2(L-1)]$, where L is the sequence length (or trellis size) and $I_2(t)$ is the t-th n-bit input symbol to C_2 in the sequence. The presence of an interleaver increases the dimensionality (and hence performance) of the equivalent lattice channel code. However, as a result of this increase in channel code dimensions, the performance of the source code suffers. From a code construction point of view, $\vec{I}_2$ in the scheme of [43, 44] is computed during the process of TCQ at the top branch based on the trellis $C_1 + C_2$. The bottom branch however employs an interleaver and hence after multiplexing the two branches, the quantization error is much larger when compared with that of the original TCQ, thus the performance loss of the source code.

The dimensionality mismatch of the source and channel code in the TCQ/TTCM scheme of [43, 44] motivated us to seek a stronger source code which could better facilitate the nesting. We thus propose the nested turbo code construction in Fig. 30, where the calculation of $\vec{I}_2$ is realized via SOTCQ. Specifically, we compute the soft-output version of sequence $\vec{I}_2$, denoted by $\vec{I}_{S2}$, using a soft-output Viterbi algorithm (SOVA) [92]. By forcing the t-th n-bit input symbol to a specific value, i.e., $I_2(t) = c_2 \in C = \{0, 1, \ldots, 2^n - 1\}$, the soft-output $I_{S2}(t, c_2)$ is given by the minimal total distortion corresponding to all possible input sequences $\vec{I}_2 \in C^L$

$$I_{S2}(t, c_2) = \min_{\substack{\vec{I}_2 \in C^L; \\ I_2(t) = c_2 \in C}} \sum_{l=0}^{L-1} \Big\{ \underbrace{\lfloor U(l) - \alpha S(l) \rfloor^2}_{\rho(l)} \Big\}, \tag{4.4}$$

where $\vec{S} = [S(0), \ldots, S(L-1)]$ is the length-L sequence of side information and $\vec{U} = [U(0), \ldots, U(L-1)]$ the corresponding sequence of codewords for a certain input sequence $\vec{I}_2$ with $I_2(t) = c_2$. The quantization error (branch metric) is denoted by

$\rho(l)$. After computing the components $I_{S2}(t, c_2)$ for all $t = 0, 1, \ldots, L - 1$ and all $c_2 \in \mathcal{C}$, $\vec{I}_{S2}$ is grouped as a matrix

$$
\vec{I}_{S2} = \begin{bmatrix} I_{S2}(0,0) & \cdots & I_{S2}(L-1,0) \\ \vdots & \ddots & \vdots \\ I_{S2}(0, 2^n - 1) & \cdots & I_{S2}(L-1, 2^n - 1) \end{bmatrix}. \tag{4.5}
$$
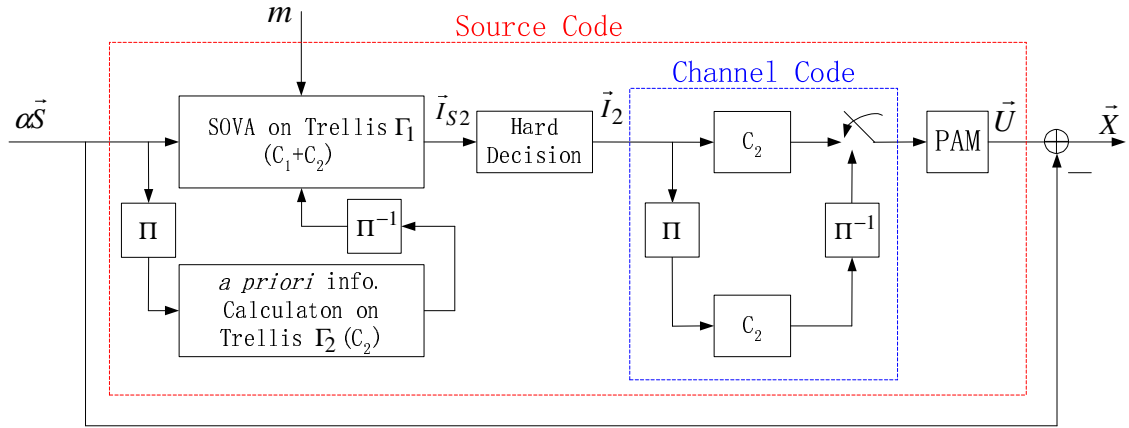
Fig. 30. Proposed nested turbo encoder for the Costa problem.

The calculation of $\vec{I}_{S2}$ in our nested turbo code construction is based on two parallel SOTCQs, as illustrated in the left part of Fig. 30. The trellis of the top branch, Γ_1, is constructed by $C_1 + C_2$, while the one at the bottom, Γ_2, contains only C_2. This parallel-branch structure is necessary for embedding the message m in trellis Γ_1. A SOVA is used to compute the soft-output $\vec{I}_{S2}$. The systematic bits are punctured at odd instants in trellis Γ_1 because of the even-odd multiplexing in the TTCM encoder, i.e., $\rho_1(t) = |U(t) - \alpha S(t)|^2$ if t is even; $\rho_1(t) = 0$ if t is odd, where $\rho_1(t)$ is the branch metric at instant t in trellis Γ_1. The metrics at odd instants are provided by trellis Γ_2 as *a priori* information. Borrowing the idea of the initialization step in TTCM decoding, for a systematic C_2, we compute the *a priori* information at instant t, denoted by $A_2(t, c_2)$, as the minimal distortion corresponding to the

input bits $I_2(t) = c_2$ and all possible parity bits $B(t) \in \mathcal{B} = \{0, 1, \ldots, 2^{m-n} - 1\}$, i.e.,

$A_2(t, c_2) = 0$ if t is even; $A_2(t, c_2) = \min_{I_2(t)=c_2; B(t)\in\mathcal{B}} |U(\Pi(t)) - \alpha S(\Pi(t))|^2$ if t is odd,

where $\Pi(t)$ denotes the same symbol interleaver as used in the TTCM encoder. This

a priori information is then deinterleaved and fed into the top trellis code. To invoke

$\rho_1(t)$ and $A_2(t, c_2)$ in the computation of the soft-output $I_{S2}(t, c_2)$, we modify (4.4)

to

$$I_{S2}(t, c_2) = \min_{\substack{\vec{I}_2 \in \mathcal{C}^L; \\ I_2(t) = c_2 \in \mathcal{C}}} \sum_{l=0}^{L-1} \left\{ \rho_1(l) + A_2(\Pi^{-1}(l), c_2) \right\},$$

with $\Pi^{-1}(l)$ denoting the symbol deinterleaver. After the SOVA on trellis Γ_1, we out-

put $\vec{I}_{S2}$ and convert it to $\vec{I}_2$ by hard thresholding $I_2(t) = \arg\min_{c_2 \in \mathcal{C}=\{0,1,\ldots,2^n-1\}} I_{S2}(t, c_2)$.

Since the turbo-like SOTCQ source code in this case has a similar parallel con-

catenated code structure as that of TTCM, the dimensionality of the source code is

higher than that of simple TCQ (with even-odd multiplexing), and thus it facilitates

better nesting of the source code inside the channel code. Indeed our simulations

indicate that our code design outperforms those of [43, 44].

2. Dimensionality balancing

Although we tend to quell the severity of the dimensionality mismatch to some extent

by employing a strong turbo-like source code, yet one cannot help but eye the potential

gain in performance if the source and channel code were even more closer in terms

of their dimensionality. Thus, to further reduce the dimensionality mismatch, we

propose a simple, but effective solution to the problem.

Let T denote the percentage of samples processed in the top branch in the

parallel-branch structure. By default both of the schemes described above (i.e.,

TCQ/TTCM and SOTCQ/TTCM) process exactly half of the samples in the top branch, that is, $T = 50\%$. Increasing T from 50%, reduces the effect of the interleaver in the bottom branch causing the degradation in the channel coding performance. However, in the same time, it guarantees improved source coding performance. (Note that, when $T = 100\%$ the scheme becomes a regular TCQ based on trellis $C_1 + C_2$.) In other words, increasing T from 50% increases the dimensionality of the source code but decreases the dimensionality of the channel code. Thus the parameter T offers a means of balancing the dimensionality of the equivalent lattice codes of the employed source and channel code. The best dimensionality balance between source and channel coding can be reached by searching for the optimal percentage T^* between 50% and 100% that leads to minimal BER after decoding the message. Note that this balancing procedure is equally applicable to both TCQ/TTCM and SOTCQ/TTCM schemes.

Our experiments show that the MSE distortion P_X introduced by the quantizer decreases when T is increased from 50 % to 100% in both the TCQ/TTCM and SOTCQ/TTCM schemes, which is expected since the underlying source coding component is becoming stronger with increasing T. When $T = 100\%$, we have the conventional TCQ scheme based on trellis $C_1 + C_2$.

On the other hand, the simulations clearly show that for the same T, our SOTCQ/TTCM design outperforms the TCQ/TTCM code in terms of achieving a smaller P_X. This improvement in source coding ultimately leads to the better performance of our SOTCQ/TTCM scheme over that of [44].

D.   Costa Code Design Based on TCQ and IRA Codes

Following the code design guidelines in Section B.3, we also propose a combined source-channel coding approach to dirty-paper coding based on TCQ and IRA codes. Specifically, treating TCQ as a form of lattice VQ, we seamlessly combine TCQ with both non-systematic and systematic IRA codes in a source-channel coding setup without sacrificing the performance of either component. That is: both the TCQ and IRA code components still work the best when combined together in our elaborate dirty-paper code constructions. This is the main advantage over our nested turbo code approach as described in the previous section.

After using the generator polynominals in [93] to implement TCQ of different number of states and subsequently obtaining the equivalent $g(\Lambda)$, we compute $\Delta\text{SNR}_\text{m}$ from (4.2) with C^*=0.25 bit/sample. Assuming that $\Delta\text{SNR}_\text{p} = 0.34$ dB (confirmed in our simulations), Table III lists the predicted total performance loss ΔSNR when the target rate is C^*=0.25 bit/sample.

We view TCQ as an efficient means of implementing an *equivalent* high-dimensional lattice quantizer Λ and use scalar notation in the sequel. The dither D is generated by keeping random inputs that are only quantized to zero by TCQ. Although dithering plays an important role theoretically, we observe little of its impact on the code performance.

• Encoder: The side information S is first linearly scaled by α, then $\alpha S + D$ is quantized to u by a coset of the TCQ selected by the message m so that the obtained quantization error

$$X = u - \alpha S - D \tag{4.6}$$

satisfies the power constraint $E[X^2] = P_X$. X is transmitted over the side-information channel.

Table III. The modulo loss $\Delta\mathrm{SNR_m}$ computed from (4.2) for TCQ of different number of states and the predicted total performance loss $\Delta\mathrm{SNR}$ in our proposed dirty-paper code designs based on TCQ and IRA codes, assuming the packing loss $\Delta\mathrm{SNR_p}$ from IRA codes is 0.34 dB and a target rate of $C^*{=}0.25$ bit/sample.

# of states in TCQ	$g(\Lambda)$ (dB)	$\Delta\mathrm{SNR_m}$ (dB)	$\Delta\mathrm{SNR_p}$ (dB)	$\Delta\mathrm{SNR}$ (dB)
$2^8{=}256$	1.33	0.65	0.34	0.99
$2^9{=}512$	1.36	0.56	0.34	0.90
$2^{10}{=}1024$	1.38	0.49	0.34	0.83
$2^{11}{=}2048$	1.40	0.43	0.34	0.77
$2^{12}{=}4096$	1.42	0.37	0.34	0.71
$2^{13}{=}8192$	1.43	0.34	0.34	0.68
$2^{14}{=}16384$	1.44	0.31	0.34	0.65

• Decoder: The decoder receives $Y = X + S + Z$ and finds the codeword $\hat{u}$ closest to

$$Y' = \alpha Y + D = u + N', \tag{4.7}$$

where $N' \triangleq (1-\alpha)(-X)+\alpha Z$ is the equivalent channel noise. Note that the "mod Λ" operation is implicitly implemented in TCQ. Finally the index of the bin containing $\hat{u}$ is identified as the decoded message.

The aim of our code design is to use the strongest possible TCQ to achieve most of the 1.53 dB granular gain while employing IRA codes to approach the capacity, and thus to match the predicted performance in Table III.

1.   Proposed TCQ Plus Non-systematic IRA Code Designs

We first present our dirty-paper code design based on a 256-state TCQ (with 1.33 dB granular gain) and *non-systematic* IRA codes. The encoder is shown in Fig. 31. Each bit of the accumulator (ACC) output sequence is repeated $\log_2 M$ times and the first two resulting bits are combined with the TCQ output bits (via modulo sum) before being used to index an M-PAM constellation. The constellation size M=16 is experimentally chosen among $\{4, 8, 16, 32\}$ so that the EXIT chart [94] of TCQ starts obviously above the origin (see Fig. 32 for the EXIT chart of TCQ with different constellation schemes). From Fig. 31, it is easy to see that the embedding rate is K/N bit/sample.
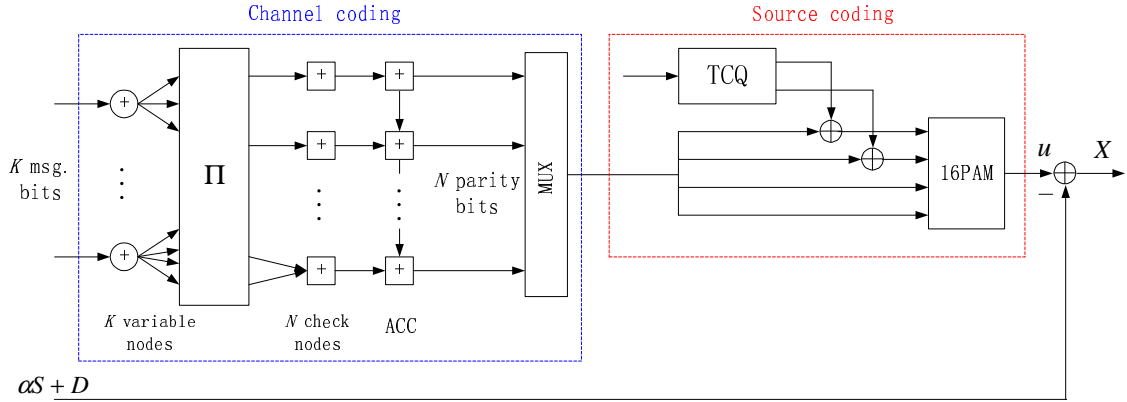
Fig. 31. Block diagram of our proposed dirty-paper encoder based on TCQ and non-systematic IRA code.

For the CND profile, we introduce bi-regularity to the non-systematic IRA code as done in [47]. That is, part of the check nodes are of degree 1, which helps move the CND EXIT chart up from the origin. Denote the percentage of edges associated with degree-1 check nodes as a_1. For various values of a_1 and the other check node degree, we examine the CND&ACC&TCQ EXIT charts and select the CND profile as: degree 1: 60% and degree 2: 40%.
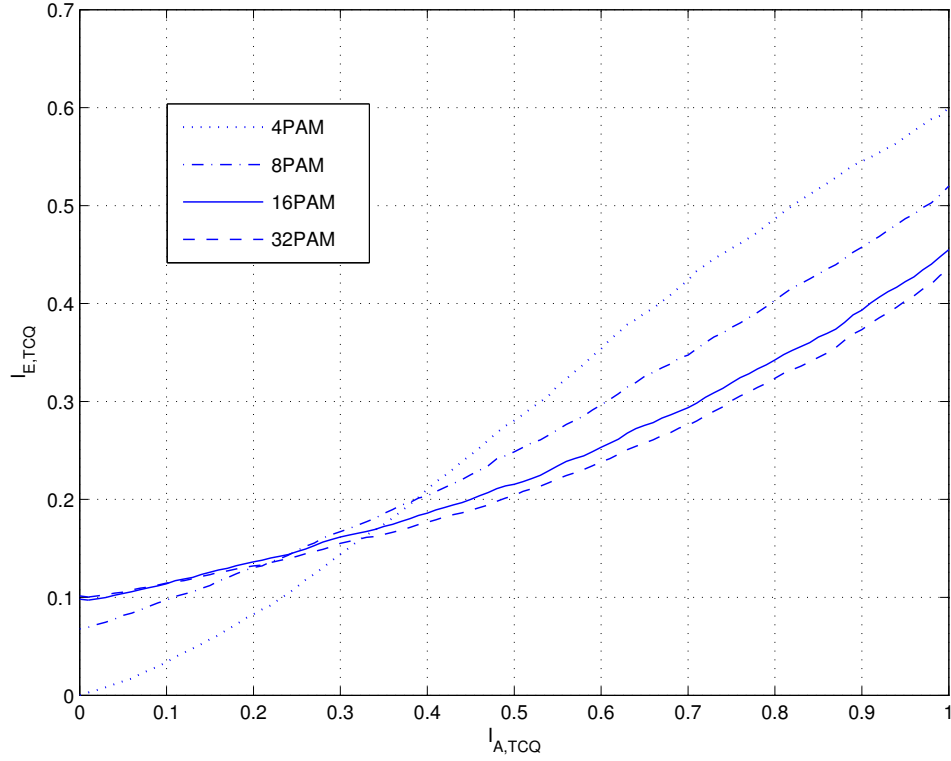
Fig. 32. EXIT chart of TCQ with various constellation sizes.

The variable node decoding (VND) EXIT chart starts from the origin, so there is a small *vertical* opening between the starting points of the CND and VND EXIT charts for practical IRA code design.

The decoder is schematically shown in Fig. 33, which consists of an inner BCJR decoder based on TCQ and ACC, an inner CND, and an outer VND. The BCJR decoder computes the extrinsic information $I_{E,ACC}$ over the joint trellis of TCQ and ACC. Then $I_{E,ACC}$ is forwarded to the inner CND as the *a priori* information. The CND generates the extrinsic information $I_{E,CND}$ that are forwarded through the edge de-interleaver Π^{-1} to the outer VND. The VND generates the extrinsic information $I_{E,VND}$ that is fed back through the edge interleaver Π to the CND. Finally, one decoding iteration is completed by feeding back the extrinsic information generated
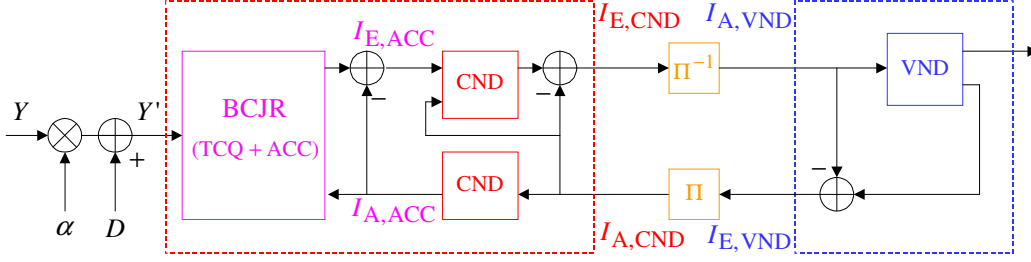
Fig. 33. Block diagram of the proposed decoder for TCQ and non-systematic IRA code.

by the CND to the BCJR decoder.

Based on the VND EXIT charts (dashed lines in Fig. 34) with different variable node degrees, we design the VND profile by matching the EXIT chart of the CND&ACC&TCQ part. To achieve the 0.25 bit/sample embedding rate, we set $K/N = 1/4$ with $K = 60,000$ and $N = 240,000$. The resulting VND profile is: degree 2: 61.29%, degree 3: 22%, degree 10: 14.86%, and degree 120: 1.857%. From Fig. 35, we see a tunnel between the CND&ACC&TCQ and VND EXIT charts, which enables convergence.
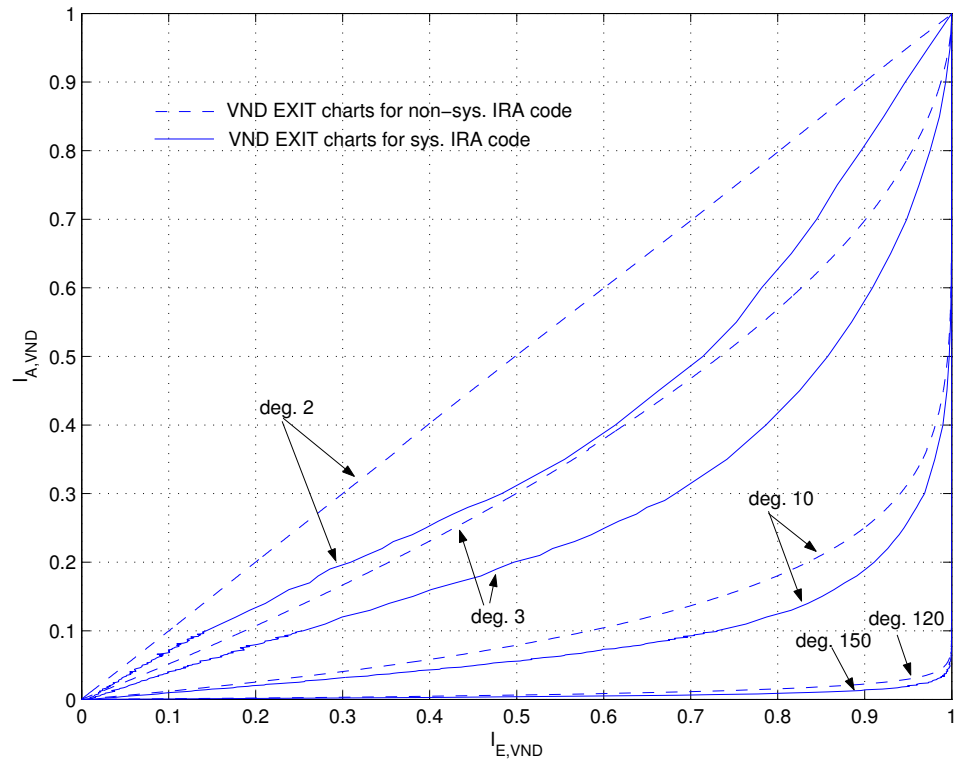
Fig. 34. VND EXIT charts with different variable node degrees.
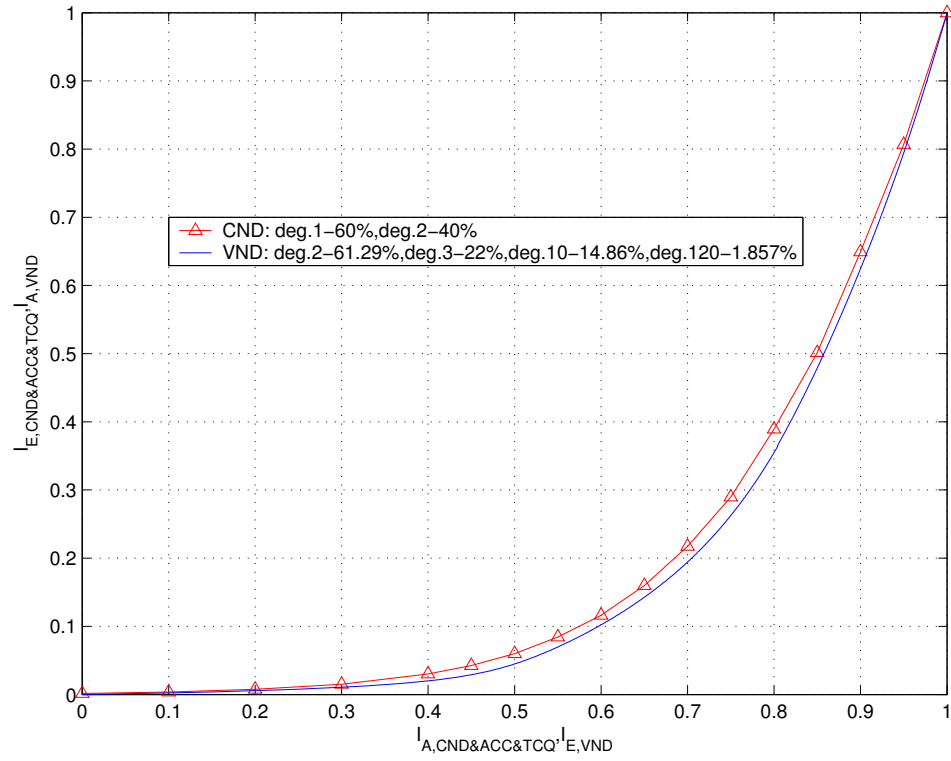
Fig. 35. EXIT charts of the non-systematic IRA code at SNR=-2.844dB with $K = 60,000$ and $N = 240,000$. TCQ has 256 states.

2. Proposed TCQ Plus Systematic IRA Code Designs

We now examine dirty-paper code design based on TCQ and *systematic* IRA codes. As advocated by Jin *et al.* in their original IRA code paper [52], we use a systematic IRA code to move the starting point of the VND EXIT chart to the *right* of the origin. This way, the *horizontal* opening between the starting points of the CND and VND EXIT charts will allow practical IRA code design. However, we discover that whereas the right shift of the VND EXIT chart from using systematic IRA codes is relatively large for pure channel coding problems, this shift is very small in dirty-paper coding (see the solid lines of Fig. 34), which involves both source coding and channel coding. We thus additionally employ bi-regularity in CND, which has demonstrated its effectiveness in moving the CND EXIT chart up from the origin in our non-systematic IRA code design. This way, the VND EXIT chart is moved to the right of the origin while the CND EXIT chart moved up from the origin to facilitate IRA code design.

Our proposed encoder is shown in Fig. 36. Its "parity part" is the same as in the non-systematic IRA code of Fig. 31. We compare the CND&ACC&TCQ$_1$ EXIT charts and select the CND profile as: degree 1: 73.33% and degree 4: 26.67%. TCQ$_2$ shown in the "systematic part" of Fig. 36 is the same as TCQ$_1$ (256 states with 1.33 dB granular gain). So the overall granular gain of our source code is 1.33 dB. The embedding rate is $K/(K + N)$ bit/sample.

The decoder is schematically shown in Fig. 37, where two BCJR decoders are used. For the "systematic part", we compute the *a priori* information I_{A,TCQ_2} based on the extrinsic information from the VND. Then the output extrinsic information I_{E,TCQ_2} is fed back to the VND. The decoder for the "parity part" resembles that in our non-systematic IRA code design.
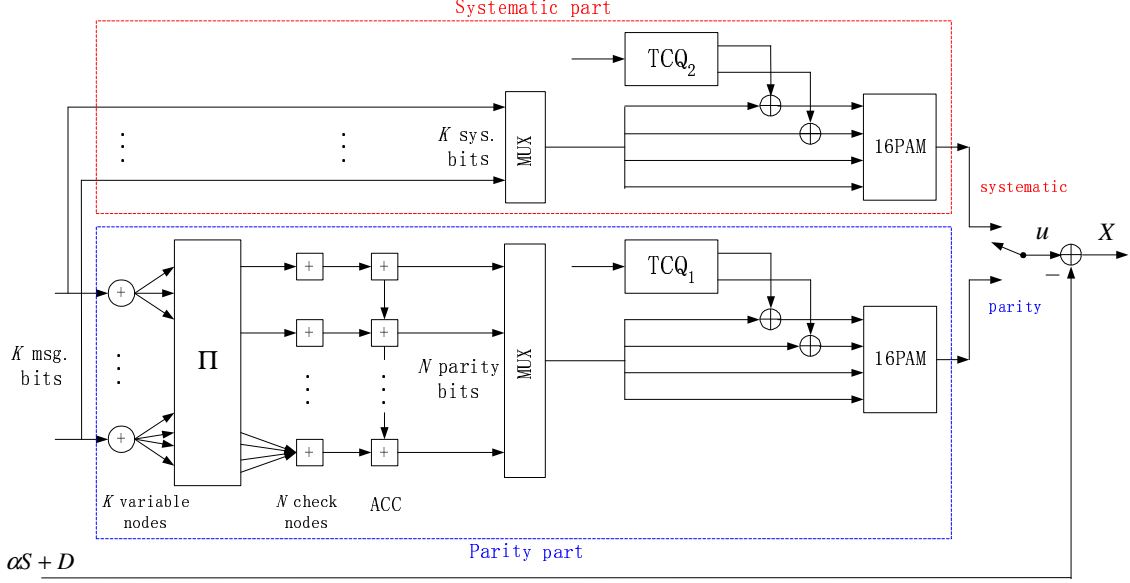
Fig. 36. Block diagram of the proposed dirty-paper encoder based on TCQ and systematic IRA code.

Due to the presence of the BCJR decoder corresponding to the "systematic part", we evaluate the VND&TCQ$_2$ EXIT charts via simulations, in which we set $K/N = 1/3$ with $K = 60,000$ bits and $N = 180,000$ bits to achieve the 0.25 bit/sample embedding rate. We design the VND profile by matching the EXIT chart of the CND&ACC&TCQ$_1$ part. The resulting VND profile is: degree 2: 58.45%, degree 3: 23.38%, degree 10: 16.94%, and degree 150: 1.223%. From Fig. 38, we see a convergence enabling tunnel between the CND&ACC&TCQ$_1$ and VND&TCQ$_2$ EXIT charts.
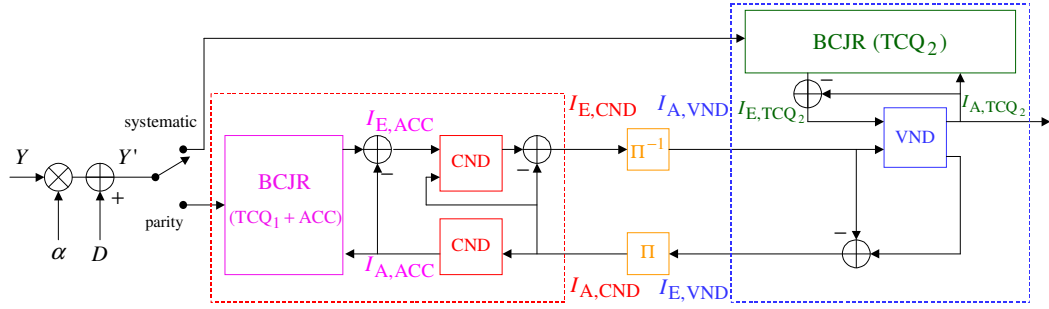
Fig. 37. Block diagram of the decoder for TCQ and systematic IRA code.
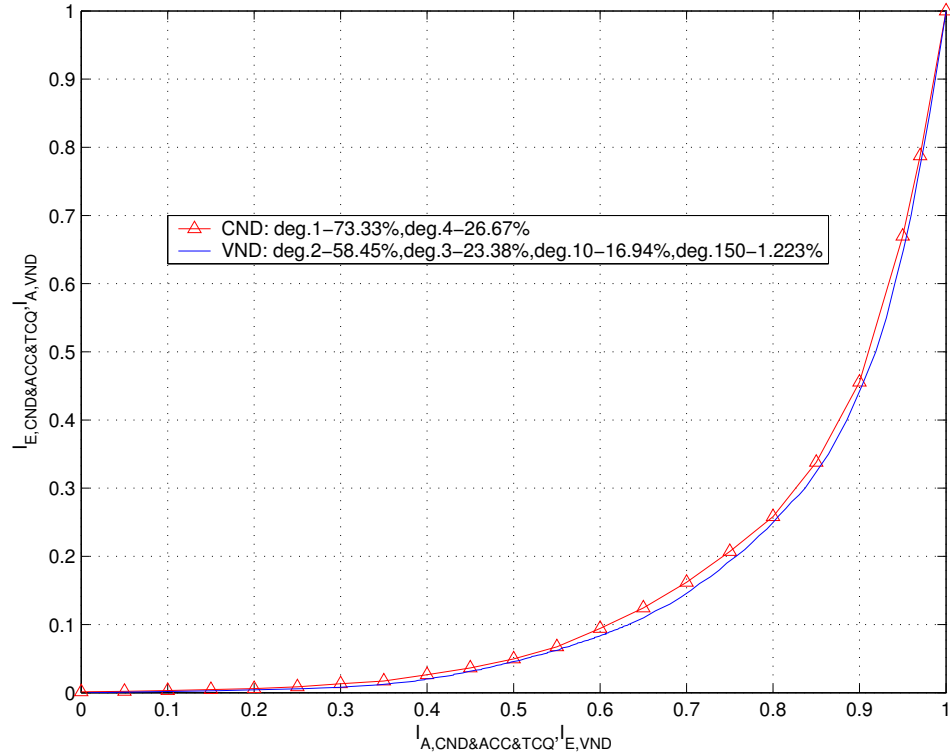
Fig. 38. EXIT charts of the systematic IRA code at SNR=-2.844dB with $K = 60,000$ and $N = 180,000$. Both TCQ$_1$ and TCQ$_2$ have 256 states.

E.   Numerical Results

1.   Nested Turbo Code Construction

We simulated our code design for embedding rates of 2.0, 1.0, and 0.5 bit/sample. A specific embedding rate is realized by appropriately choosing the code rate parameters (n, k, m). For all embedding rates, both convolutional codes C_1 and C_2 were chosen as the constraint-length four Ungerboeck code [93]. C_2 has to be systematic to fit the turbo algorithm. If C_1 is also systematic, there exists error propagation when recovering the original message sequence by calculating the syndromes, since the parity-check polynomials have infinite weights. Therefore, non-systematic C_1 should be used.

The code C_2 is mapped to a finite constellation, which we call the basic constellation. The side information can have an arbitrary large magnitude, therefore we replicate the basic constellation infinitely so that the side information never lies in the overload region of the quantizer (so that the power constraint is satisfied). The quanitzer thus selects a copy of the basic constellation codeword which lies nearest to the side information.

We evaluate the system performance by its BER at a certain SNR. First we look at the effect of varying Δ on the code performance. Our experiments indicate little performance improvement by selecting optimal Δ, and this is true for different T's and embedding rates. Thus, in the following simulations, Δ is set to 1.0 for all embedding rates. In addition, all results are based on 256-state TCQ and a BER of 10^{-5}.

a.   Simulation Results at 2.0 bit/sample

For an embedding rate of 2.0 bit/sample, the rate k/n of code C_1 has to be chosen such that $n-k = 2$. Hence C_1 is chosen as a non-systematic rate 1/3 code. The polynomials are found using a computer search over all possible rate 1/3 codes [93]. The generator polynomials for C_1 are $g_0(D) = 23$, $g_1(D) = 4$ and $g_2(D) = 2$ in octal notation. Code C_2 is chosen as a systematic rate 3/4 code with parity check polynomials $h_0(D) = 23$, $h_1(D) = 10$, $h_2(D) = 0$, and $h_3(D) = 0$. The codewords of C_2 are thus mapped to a 16-PAM constellation. Fig. 39 shows the effect of dimensionality balancing for the SOTCQ/TTCM scheme at an embedding rate of 2.0 bit/sample.

Our best results indicate a performance gap to capacity of only 0.94 dB. As seen in the plot, the source coding loss of (4.2) decreases as T increases, but is offset by an increase in the channel coding loss. This clearly illustrates the source-channel coding tradeoff in our nested turbo code design.

We applied the same dimensionality balancing procedure to the TCQ/TTCM scheme of [43, 44]. A summary of these results is provided in Table IV; the performance of a simple TCQ/TCM scheme of [91] are given as a benchmark. Table IV indicates the huge performance gain in performance as compared to the performance of the work in [91].

Dimensionality balancing only shows a small performance gain at this embedding rate. Indeed, as shown in the table, our SOTCQ/TTCM scheme performs slightly better than the TCQ/TTCM scheme of [43, 44].

Fig. 39. Effect of dimensionality balancing on the performance of our proposed nested turbo scheme when the rate is 2.0 bit/sample and interleaver length is L=50,000.

Table IV. Performance gap (in dB) from the capacity for different code designs when the rate is 2.0 bit/sample. A rate-1/3/4 concatenated code and a 1-D lattice with step size $\Delta = 1.0$ was used.

		L = 10,000				L = 50,000			
	TCQ/TCM	TCQ/TTCM		SOTCQ/TTCM		TCQ/TTCM		SOTCQ/TTCM	
$T(T^*)$	-	50%	72.5%	50%	70%	50%	73 %	50%	70.5%
$g(\Lambda)$	1.36	0.99	1.12	1.07	1.15	0.99	1.12	1.07	1.15
ΔSNR_m	0.18	0.58	0.44	0.49	0.41	0.58	0.44	0.49	0.41
ΔSNR_p	3.57	0.64	0.65	0.60	0.61	0.56	0.58	0.52	0.53
ΔSNR	3.75 [91]	1.22	1.09	1.09	1.02	1.14	1.02	1.01	0.94

b.   Simulation Results at 1.0 bit/sample

Fig. 40 shows the performance of our nested scheme SOTCQ/TTCM at an embedding rate of 1.0 bit/sample. C_1 is chosen as a non-systematic rate $1/2$ code with generator polynomials $g_0(D) = 23$ and $g_1(D) = 10$ in octal notation. Code C_2 on the other hand is a rate $2/3$ systematic code with parity check polynomials $h_0(D) = 23$, $h_1(D) = 10$, and $h_2(D) = 0$. The codewords of C_2 are mapped to an 8-PAM constellation.

Compared to even-odd multiplexing $(T = 50\%)$, our dimensionality balancing procedure is able to gain more than 0.3 dB in performance. Moreover, as indicated by Table V, at $T=50\%$, our proposed scheme SOTCQ/TTCM performs more than 0.2 dB better than the TCQ/TTCM scheme [43, 44]. These observations indicate that the dimensionality balancing is more effective at lower rates. A comparison of the source coding losses in Figs. 39 and 40 reveals that the source coding loss at $T=50\%$ is much higher in the case of 1.0 bit/sample than for 2.0 bit/sample. Therefore, the underlying source and channel codes are inherently more unbalanced in terms of their dimensionality at lower rates, and hence there exists a larger room for improvement. Also note that optimal dimensionality balancing for TCQ/TTCM is achieved at a higher value of T^* than with SOTCQ/TTCM, which is intuitive since the source code in the latter scheme is of higher dimensions.
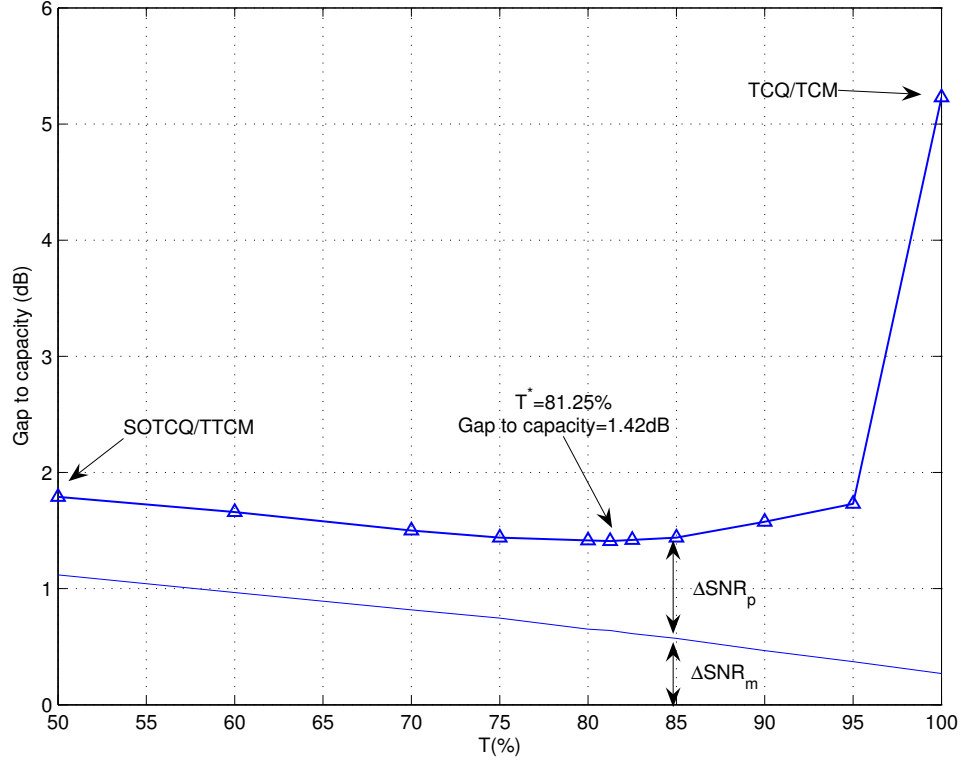
Fig. 40. Effect of dimensionality balancing on the performance of our proposed nested turbo scheme when the rate is 1.0 bit/sample and interleaver length is L=50,000.

Table V. Performance gap (in dB) from the capacity for different code designs when the rate is 1.0 bit/sample. A rate-1/2/3 concatenated code and a 1-D lattice with step size $\Delta = 1.0$ was used.

	TCQ/TCM	L = 10,000				L = 50,000			
		TCQ/TTCM		SOTCQ/TTCM		TCQ/TTCM		SOTCQ/TTCM	
$T(T^*)$	-	50%	82.5%	50%	80%	50%	83.5%	50%	81.25%
$g(\Lambda)$	1.33	0.406	0.95	0.67	1.04	0.406	0.97	0.67	1.04
$\Delta\mathrm{SNR_m}$	0.28	1.45	0.76	1.12	0.65	1.45	0.74	1.12	0.65
$\Delta\mathrm{SNR_p}$	4.95	0.62	0.87	0.71	0.88	0.57	0.79	0.67	0.77
$\Delta\mathrm{SNR}$	5.23 [44]	2.07 [44]	1.63	1.86	1.53	2.02	1.53	1.79	1.42

c.   Simulation Results at 0.5 bit/sample

In order to get a fractional embedding rate, we use a 2-D QAM constellation. C_1 is chosen to be Ungerboeck's systematic rate 2/3 code for a QAM constellation, with the feedback polynomial being $h_0(D) = 23$ and the feedforward polynomials being $h_1(D) = 4$ and $h_2(D) = 16$. In order to avoid its infinite weights, the parity check matrix of C_1 used for calculating the syndromes is pre-multiplied by $h_0(D)$. Code C_2 is chosen as a rate 3/4 with $h_0(D) = 23$, $h_1(D) = 4$, $h_2(D) = 16$, and $h_3(D) = 2$. The mapping from the codewords of C_2 to the constellation is based on Ungerboeck's partitioning of a 16-QAM constellation [93].

Fig. 41 shows the effectiveness of the dimensionality balancing procedure at this low rate. Compared to the even-odd multiplexing ($T = 50\%$) we attain a performance gain of more than 0.5 dB. Moreover, as seen from Table VI, our proposed nested turbo scheme (SOTCQ/TTCM) outperforms TCQ/TTCM [43, 44] by more than 0.6 dB. Thus the dimensionality balancing is clearly more effective at lower rates. Another interesting observation from the figure is that T^* for both schemes is close to 100%; hence at low rates a low level of interleaving suffices to attain large performance gains.
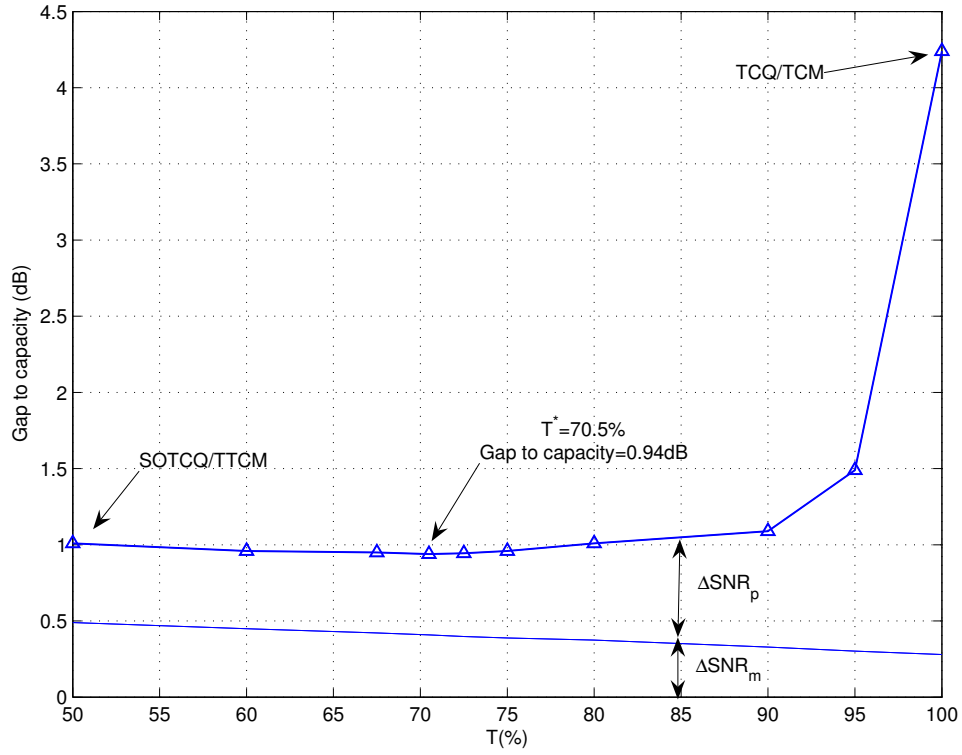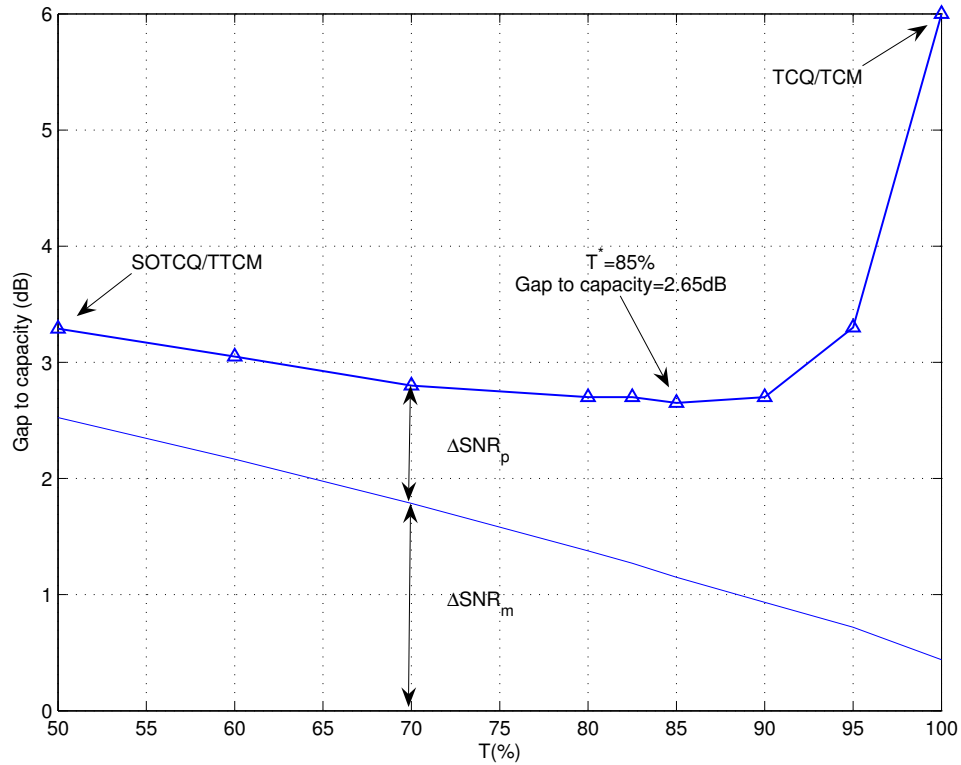
Fig. 41. Effect of dimensionality balancing on the performance of our proposed nested turbo scheme when the rate is 0.5 bit/sample and interleaver length is L=50,000.

Table VI. Performance gap (in dB) from the capacity for different code designs when the rate is 0.5 bit/sample. A rate-2/3/4 concatenated code and a 2-D lattice with step size $\Delta = 1.0$ was used.

		L = 10,000				L = 50,000			
	TCQ/TCM	TCQ/TTCM		SOTCQ/TTCM		TCQ/TTCM		SOTCQ/TTCM	
$T(T^*)$	-	50%	90%	50%	82.5%	50%	92.5 %	50%	85%
$g(\Lambda)$	1.32	-0.35	0.96	0.09	0.85	-0.35	1.05	0.09	0.92
$\Delta\mathrm{SNR_m}$	0.42	3.19	1.08	2.52	1.27	3.19	0.92	2.52	1.15
$\Delta\mathrm{SNR_p}$	5.58	0.81	1.86	0.86	1.53	0.73	1.87	0.77	1.50
$\Delta\mathrm{SNR}$	6.00 [44]	4.00	2.94	3.38	2.80	3.92	2.79	3.29	2.65

2. Dirty-paper Code Design Based on TCQ and IRA Codes

For the Costa coding based on TCQ and IRA codes, we provide the simulation results at embedding rates of 0.25 and 0.5 bit/sample with TCQ of various memories. For each case, we compute the granular gain via TCQ and design the IRA code to achieve the predicted performance in Table III. The code design process is fulfilled by matching the CND and VND EXIT charts, as discuss in Section D. The adjustable parameters are the constellation size, the bi-regular check node profile, and the variable node profile.

We evaluate the code design via the BER performance at the target SNR (from Table III), and its efficiency is confirmed when the BER is in the order of 10^{-5}. Then we give a detailed comparison of our TCQ/IRA scheme with the nested turbo approach and the current code design in [47].

a. Code Designs at 0.25 bit/sample

At the embedding rate of 0.25 bit/sample, **five** code designs are studied given various numbers of states in TCQ and non-systematic/systematic IRA codes.

1) **Code design based on 256-state TCQ and non-systematic IRA code** The code design procedure together with the IRA profiles have been given in Section D.1. After simulating 100 blocks of transmission, we obtain a BER of 1.50×10^{-5} when SNR=-2.844 dB, which is 0.984 dB away from the SNR* for C^*=0.25 bit/sample embedding rate. This performance is slightly better than the predicted 0.99 dB gap shown in Table III when the granular gain of TCQ is 1.33 dB (again the 0.34 dB packing loss is due to practical IRA coding). The maximal number of decoding iterations is set to be 150 and the actual number to achieve convergence is between 40 and 110.

2) **Code design based on 512-state TCQ and non-systematic IRA code**
We have also designed a 512-state TCQ (with 1.36 dB granular gain) together with a non-systematic IRA code with $K = 30,000$ and $N = 120,000$. 16PAM constellation is applied. The CND profile is: degree 1: 80% and degree 3: 20%, and the VND profile is: degree 1: 46.17%, degree 2: 38.39%, degree 10: 13.92%, and degree 140: 1.523%. After simulating 100 blocks of transmission, we obtain a BER of 1.56×10^{-5} when SNR=-2.9258 dB, which is 0.90 dB away from the SNR* at 0.25 bit/sample, matching the predicted performance in Table III. The maximal number of decoding iterations is set to be 150 and the actual number to achieve convergence is between 50 and 115.

3) **Code design based on 1024-state TCQ and non-systematic IRA code**
For this case, we set $K/N = 1/4$ with $K = 22,500$ and $N = 90,000$. The resulting VND profile is: degree 2: 64.88%, degree 3: 24.33%, degree 13: 10.17%, and degree 360: 0.627%. After simulating 100 blocks of transmission, we obtain a BER of 4.76×10^{-5} when SNR=-2.993 dB, which is 0.83 dB away from the capacity in (1.2) at 0.25 b/s embedding rate. This performance matches the predicted 0.49+0.34=0.83 dB gap in Table III when the granular gain of TCQ is 1.38 dB (with 0.34 dB packing loss due to practical IRA coding). The maximal number of decoding iterations is set to be 150 and the actual number to achieve convergence is between 44 and 105.

4) **Code design based on 256-state TCQ$_1$/256-state TCQ$_2$ and systematic IRA code**
In Section D.2, we reach a code design based on the systematic IRA code. Both TCQ$_1$ in the "parity part" and TCQ$_2$ in the "systematic part" have 256 states. Similar to the case with non-systematic IRA code (and 256-state TCQ), 50 blocks of transmission are simulated at 0.25 bit/sample embedding rate. We obtain a BER of 2.08×10^{-5} at the same 0.984 dB gap from SNR*. The maximal number of decoding

iterations is again 150 and the actual number to achieve convergence is between 50 and 115.

5) **Code design based on 512-state TCQ_1/1024-state TCQ_2 and systematic IRA code**

In general, TCQ_2 can be different from TCQ_1 as long as they are designed such that both satisfy the same power constraint P_X. This way, they can be used interchangeably from a power consumption point of view. However, the difference between them lies in their granular gain. Since the decoding complexity for TCQ_2 is lower than that for TCQ_1, within the same complexity limit, the potential offered by two TCQs in achieving higher granular gains than a single TCQ can (with non-systematic IRA codes) is our main impetus for studying code designs based on systematic IRA codes. We have constructed a systematic IRA code ($K = 30,000$ and $N = 90,000$) together with a 512-state TCQ_1 (with 1.36 dB granular gain) and a 1024-state TCQ_2 (with 1.38 dB granular gain) for an overall granular gain of 1.3662dB in source coding, which leads to a 0.55 dB modulo loss. Together with the assumed 0.34 dB packing loss, the estimated overall gap to capacity will be 0.89 dB. We reach an IRA design with the CND profile as: degree 1: 73.33% and degree 4: 26.67%, and the VND profile as: degree 1: 57.24%, degree 2: 31.23%, degree 10: 9.98%, and degree 150: 1.55%. After simulating 20 blocks of transmission, we obtain a BER of 5×10^{-5} when SNR=-2.945 dB, which is 0.883 dB away from the SNR* at 0.25 bit/sample. The maximal number of decoding iterations is set to be 150 and the actual number to achieve convergence is between 40 and 100.

For clear comparisons, we summarize the above code designs in Table VII and see that all of them can work well at the predicted performances based on (4.2) and (4.3).

Table VII. Performance gap (in dB) from the capacity for dirty-paper code designs based on TCQ and (non-systematic and systematic) IRA codes at 0.25 bit/sample

	# of states in TCQ(s)	Predicted ΔSNR	Simulated ΔSNR
Non-sys. IRA design	256-state TCQ	0.99	0.98
	512-state TCQ	0.90	0.90
	1024-state TCQ	0.83	0.83
Sys. IRA design	256-state TCQ_1/256-state TCQ_2	0.99	0.98
	512-state TCQ_1/1024-state TCQ_2	0.89	0.88

b. Code Design at 0.5 bit/sample and Comparisons with Nested Turbo Approach

To compare to the nested turbo code construction, we provide a code design based on 256-state TCQ and non-systematic IRA code at the embedding rate of 0.5 bit/sample. Given the 1.33dB granular gain, we evaluate the modulo loss $\Delta\text{SNR}_\text{m} = 0.40$dB based on (4.2). For the channel code, rate-1/2 IRA code is required, and thus a larger packing loss can be expected. We assume $\Delta\text{SNR}_\text{m} = 0.40$dB and design the IRA code at SNR=0.80dB (At 0.5 bit/sample, the SNR to achieve the capacity limit is 0dB). Following the procedure described in Section D.1, we select 8-PAM constellation and determine the bi-regular CND profile: degree 1: 10%, degree 3 90%, and the VND profile: degree 2: 31.33%, degree 3: 59.45%, degree 28: 9%, degree 300: 0.223%.

We constructed a rate-1/2 non-systematic IRA code with $K = 60,000$, $N = 120,000$ and simulated the system at SNR=0.81dB. After 100 blocks of transmission, the BER is as low as 4.5×10^{-6} with 75-180 iterations.

Fig. 42 gives an explicit comparison between the scheme based on TCQ and IRA codes and the nested turbo code construction. The former works better in both source coding and channel coding, and thus outperforms the latter by 1.84dB!

Besides the employed powerful source and channel codes, our TCQ/IRA design
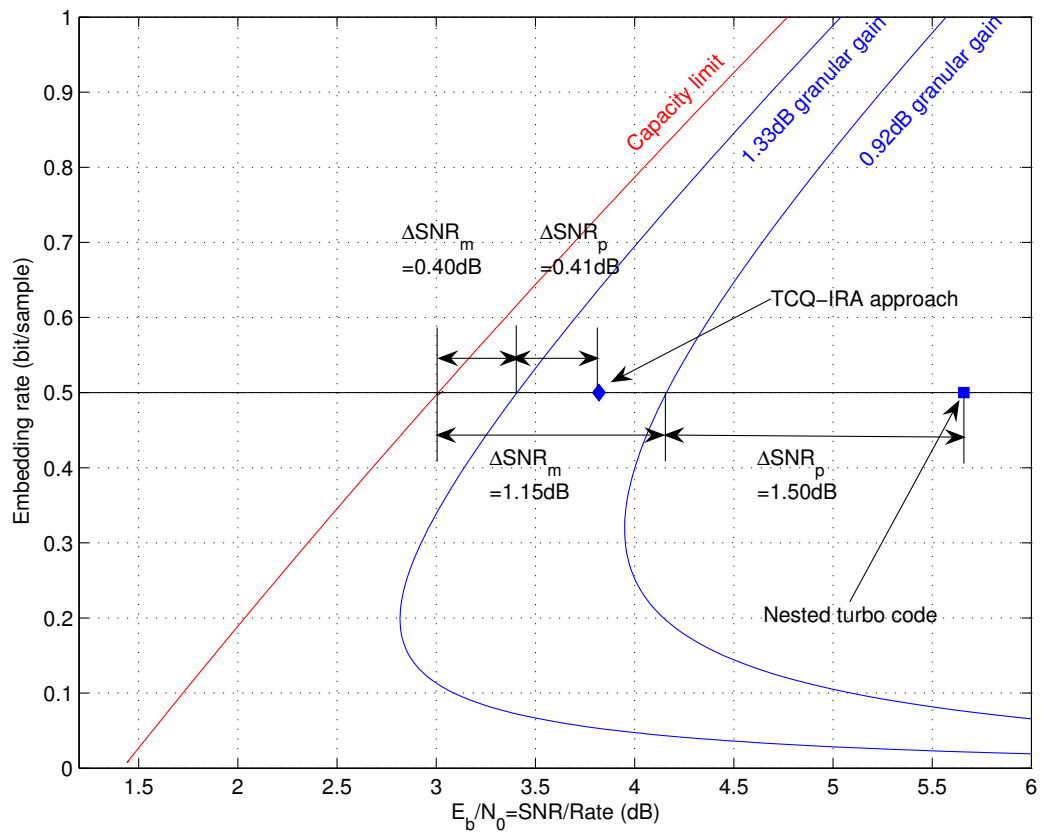
Fig. 42. Performance comparison between the TCQ/IRA scheme and the nested turbo code design at 0.5 bit/sample.

exhibits no coupling between source coding and channel coding. While in the nested approach of Fig. 30, a strong coupling exists since the TTCM channel code is part of the whole SOTCQ source coding. Hence, any gain in the performance of the source code results in a loss in the performance of the channel code and vice versa. This inherent source-channel coding performance tradeoff, as demonstrated in Figs. 39-41, is the main weakness responsible for the sub-par performance of our nested turbo code design at low rates.

On the other hand, for high embedding rates, it is still not clear how the TCQ/IRA design and other constructions geared towards low rates [47, 48] would operate and what would be the performance. Thus our proposed two practical Costa code designs are complementary to each other and offer the best performance so far in the whole embedding rate region (from low rates to high rates).

c.   Comparisons with ten Brink and Erez's Scheme

A clear performance comparison between our TCQ/IRA design with ten Brink and Erez's scheme [47] is shown in Fig. 43. We assume a 256-state TCQ in our design and a memory-8 VQ in [47]. The achieved granular gains are 1.33dB and 1.28dB, respectively, and thus the modulo losses $\Delta\text{SNR}_\text{m}$ can be computed by (4.2) as 0.65dB and 0.81dB at 0.25 bit/sample. By assuming the same packing loss $\Delta\text{SNR}_\text{p} = 0.34$dB, the performance gain over ten Brink and Erez's scheme should be 0.16dB, which has been confirmed by our simulation results in Fig. 43. Note that larger gain can be expected at lower embedding rates.

We then compare the two schemes in their complexities. Because the main computational complexity of our dirty-paper codes lies in BCJR decoding, we provide a quantitative complexity comparison in terms of the number of *loop* operations needed for each BCJR decoding iteration.

For the design in [47], $K = 60,000$ and $N = 360,000$. The ACC takes three-bit inputs with systematic doping applied to the second and third bits, so the *effective* block length of TCQ is $N/3 = 120,000$. The number of input bits in the trellis is 1(VQ)+3(ACC)=4. Thus the number of loop operations is $2^{(8+1)}$(# of states)$\times 2^4$(input bits)$\times$120,000(length)=$512 \times 4 \times 480,000$ per BCJR decoding iteration.

In our design based on non-systematic IRA code and 256-state TCQ, $K = 60,000$, $N = 240,000$, the number of input bits is 1(TCQ)+1(ACC)=2. The BCJR decoder thus needs to run $2^{(8+1)} \times 2^2 \times 240,000 = 512 \times 4 \times 240,000$ loop operations per iteration. This design is thus only half as complex as that in [47]. We see that, although systematic (or unsigned bit) doping in [47] reduces the effective block length of TCQ, it exponentially increases the complexity of the BCJR decoder due
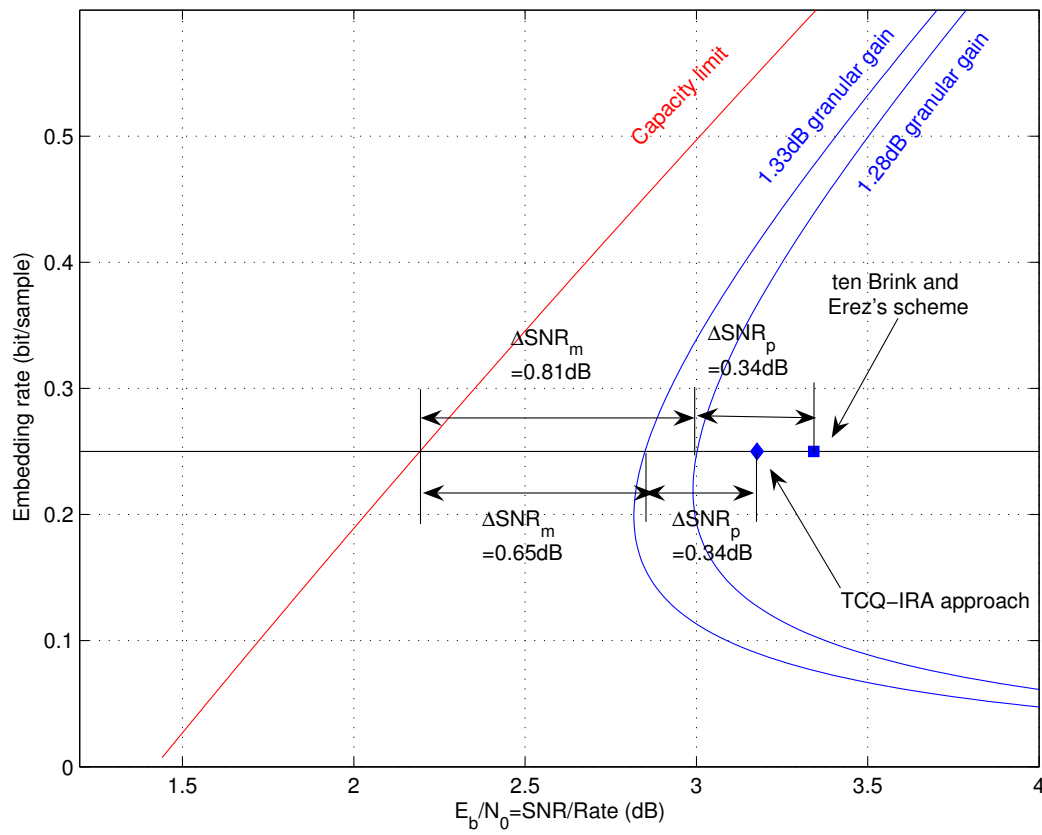
Fig. 43. Performance comparison between the TCQ/IRA design and the scheme in [47] at 0.25 bit/sample.

to increased number of input bits to the ACC. Furthermore, when it is coupled with VQ in [47], as manifested by the non-Gaussian pdf of the quantization error in Fig. 44(a), the source coding performance is degraded. In contrast, the pdf in Fig. 44(b) of the quantization error with 256-state TCQ in our code design without systematic doping is very close to be Gaussian. This explains why *our design performs better (at lower complexity)*.

In our design based on systematic IRA code and 256-state TCQs, $K = 60,000$ and $N = 180,000$, the number of input bits is 1(TCQ$_2$)+1(systematic bit)=2 for the "systematic part" and 1(TCQ$_1$)+1(ACC)=2 for the "parity part". In the "systematic part", the total number of loop operations is $2^8 \times 2^2 \times 60,000 = 256 \times 4 \times 60,000$. In the "parity part", the number is $2^{(8+1)} \times 2^2 \times 180,000 = 512 \times 4 \times 180,000$. The combined number of loop operations is thus $512 \times 4 \times 210,000$ per iteration, which is $\frac{7}{8}$ of the complexity of our design based on non-systematic IRA code.

Finally, the total number of loop operations in our code designs using 512-state TCQ and non-systematic IRA code (with $K = 30,000$ and $N = 120,000$) and using 512-state TCQ$_1$, 1024-state TCQ$_2$ and systematic IRA code (with $K = 30,000$ and $N = 90,000$) is the same at $512 \times 4 \times 240,000$ per BCJR decoding iteration.
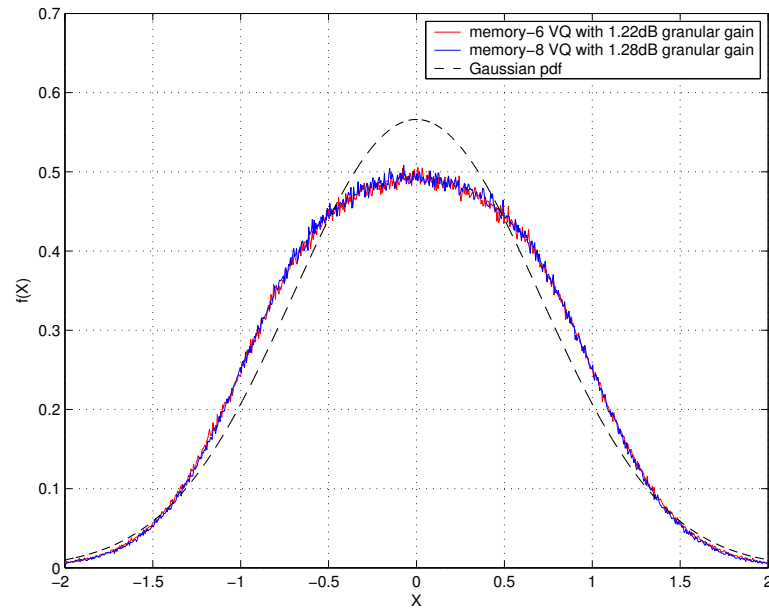
(a) ten Brink and Erez's scheme [47]
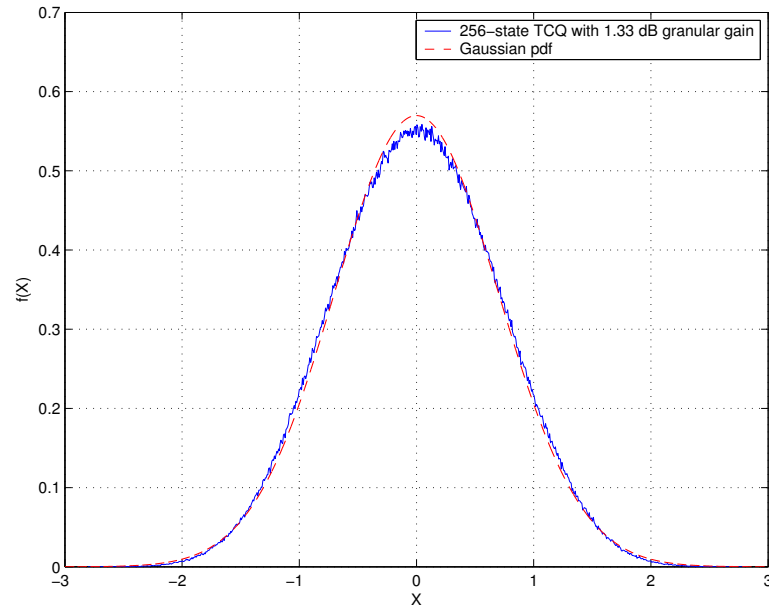
(b) TCQ/IRA design

Fig. 44. Comparison of the pdf of quantization error X between the scheme in [47] with memory-8 VQ and our TCQ/IRA design with 256-state TCQ, together with the Gaussian pdf.

F.   Conclusions and Future Work

We have addressed the hard problem of practical dirty-paper code designs and proposed two approaches based on the philosophy of source-channel coding.

Compared with the TCQ/TTCM scheme of [43, 44], where TCQ is weakened by the employment of TTCM, our nested SOTCQ/TTCM scheme improves the interaction between the source code and the channel code. This is achieved by improving source coding using SOTCQ and via a novel dimensionality balancing procedure that optimizes the percentage of samples between parallel branches in our nested turbo code design. The effectiveness of our SOTCQ/TTCM scheme and the dimensionality balancing procedure is confirmed by simulations. Compared to the even odd multiplexing of [43, 44], the dimensionality balancing approach promises significant performance gains especially at low to moderate embedding rates. The underlying nested TCQ/TTCM and SOTCQ/TTCM scheme, however, are not suitable for low embedding rates.

At low embedding rates, the combined source-channel coding approach we take enables us to seamless combine TCQ and IRA codes in the best performing dirty-paper code and see a separate modulo loss due to source coding and the packing loss due to channel coding. Compared to the nested coding approach in [47] that necessitates systematic doping and tailor-designed generator polynomials for shaping codes, our source-channel coding philosophy is much simpler with standard TCQ [35] and no systematic doping, leading to better performance at lower complexity. Compared to the superposition coding approach in [48], our main contributions are the explicit and better code designs with performance matching those predicted in Table III.

Our nested turbo scheme provides the best performs so far at medium-to-high

rates (e.g., ≥ 1.0 bit/sample), while our TCQ/IRA approach works the best at the low rate regime (e.g., < 1.0 bit/sample). Thus our two practical Costa code designs are complementary to each other.

Now we are trying to improve our approach based on TCQ and IRA codes (see Table III) with TCQ of higher memories at 0.25 bit/sample, while addressing applications of dirty-paper coding in data hiding, coding for broadcast channels, precoding for interference channels, and transmitter cooperation in wireless networks. We note that several Costa code designs have recently been applied to data-hiding/watermarking [95, 45, 96, 97, 98] and digital broadcasting [99]. Exploring the proposed code designs for these applications is our next step. One preliminary work on image data hiding is reported in [100] and some promising results have been presented.

CHAPTER V

CONCLUSIONS

The two basic components of information theory, source coding and channel coding, have been investigated separately since the birth of Shannon's information separation theorem [1, 2]. In these years, the research on their combination, i.e., source-channel coding, has attracted great interests. One direction is inspired by the invalidation of the separation theorem in practical scenario without assuming infinite codeword lengths. In this case, JSCC is required to tradeoff source and channel coding for better performance over separate coding. On the other hand, for some hottest problems, e.g., coding with side information [101, 102, 31, 30], their nature characterized by source-channel coding has been discovered [33], which will indicate a source-channel coding approach for their practical code designs.

The above discussions motivate the two problems studied in this dissertation: 1) wireless image transmission and 2) dirty-paper code design.

In the first part of the dissertation, we consider a progressive image transmission system over wireless channels by combining JSCC, STC and OFDM. To simplify the analysis, we assume coherent detection with perfect CSI at the receivers. Its BER performance is evaluated theoretically based on a newly built broadband MIMO fading model, which involves both time-domain fading correlation due to Doppler shift and spatial-domain fading correlation among different receive antennas induced by those environmental parameters. Then for a given average SNR (hence BER), a fast local search algorithm is applied to optimize UEP in JSCC, subjected to fixed total transmitted energy for various constellation sizes. This design allows the measurement of the expected reconstructed image quality. With this end-to-end system

performance evaluation, an adaptive modulation scheme is proposed to pick the constellation size that offers the best reconstructed image quality for each average SNR. Simulation results of practical image transmissions confirm the effectiveness of our proposed adaptive modulation scheme.

A more practical scenario is also considered without the assumption of perfect CSI. We employ low-complexity decision-feedback decoding for differentially space-time coded OFDM systems to exploit the transmit diversity. For JSCC, we adopt a product channel code structure that is proven to provide powerful error protection and good bursty error robustness. A fast product code optimization algorithm is applied in the JSCC/UEP design. Compared to another non-coherent detection algorithm, i.e., the iterative receiver based on expectation-maximization algorithm for the space-time coded OFDM systems, differentially space-time coded OFDM systems suffer some quality loss in reconstructed images. With the efficiency and simplicity of decision-feedback differential decoding, differentially space-time coded OFDM is thus a feasible modulation scheme for practical applications such as wireless image over mobile devices (e.g., cell phones). Motivated by the employment of more powerful channel codes for further performance improvement, we apply iterative (turbo) decoding techniques developed for serially concatenated coding systems to improve the performance in successive decoding iterations. We also treat the product code structure as one means of MD coding realized by embedded image coding plus UEP. That is, we propose the iterative decoding of differentially space-time coded MDs of Images by using MD coding as the outer constituent code and a differential space-time code as the inner constituent code. Experimental results show that our iterative scheme can effectively improve the system performance. Furthermore, most of the gain in PSNR is achieved with only one iteration in the low SNR range, e.g., 0-20 dB.

The second part of the dissertation deals with practical code designs for dirty-paper coding, the Gaussian case of Gelfand-Pinsker coding or coding with side information at the encoder. We first invoke an information-theoretical interpretation of algebraic binning and point out that the total performance loss (in SNR) can be broken into the sum of the packing loss from channel coding and a modulo loss, which depends on the granular loss from source coding and the target dirty-paper coding rate (or SNR). These observations motivate we the code design guidelines in terms of source-channel coding: one needs powerful source codes to achieve almost all the 1.53 dB granular gain and near-capacity channel codes to realize as much packing gain as possible.

Following these guidelines based on source-channel coding, two dirty-paper code designs have been proposed to target at different embedding rate regions.

We first address practical code design based on nested lattice codes and propose a nested turbo construction using SOTCQ for source coding and TTCM for channel coding. A novel procedure is devised to balance the dimensionalities of the equivalent lattice codes corresponding to SOTCQ and TTCM. Our code construction significantly outperforms existing TCQ/TCM and TCQ/TTCM designs and exhibits a gap of 0.94, 1.42 and 2.65 dB to the Costa capacity at 2.0, 1.0, and 0.5 bit/sample, respectively. Despite the effectiveness of our dimensionality balancing procedure, the gap to capacity at the embedding rate of 0.5 bit/sample remains at 2.65 dB, which shows its non-efficiency at low rates. This is because a strong coupling between the source and channel codes exists in our nested design, where the TTCM channel code is part of the whole SOTCQ source coding. Hence, any gain in the performance of the source code results in a loss in the performance of the channel code and vice versa. This inherent source-channel coding performance tradeoff is the main weakness responsible for the sub-par performance of our nested turbo approach at low rates.

We then examine practical designs by combining TCQ with both systematic and non-systematic IRA codes. Like previous approaches, we exploit the EXIT chart technique for capacity-approaching IRA channel code design; but unlike previous approaches, we emphasize the role of strong source coding and endeavor to achieve as much granular gain as possible by using TCQ. More importantly, our novel code designs enable TCQ and IRA codes to work as well in a combined source-channel coding setup as they do individually. At 0.25 bit/sample, our design using 1024-state TCQ and IRA codes performs 0.83 dB away from the capacity, which is the best performance so far. We are thus approaching the theoretical limit of dirty-paper coding. Moreover, when compared to the recent scheme in [47], our design operates at only half complexity.

Our TCQ/IRA approach targets at low rates (e.g., <1.0 bit/sample), while our nested SOTCQ/TTCM scheme provides the best performs so far at medium-to-high rates (e.g., $\geq$ 1.0 bit/sample). Thus our two proposed practical dirty-paper code designs are complementary to each other.

REFERENCES

[1] C. E. Shannon, "A mathematical theory of communication," *Bell System Technical Journal*, vol. 27, pp. 379-423, July 1948.

[2] T. Cover and J. Thomas, *Elements of Information Theory*. New York: Wiley, 1991.

[3] A. Said and W. A. Pearlman, "A new, fast, and efficient image codec based on set partitioning in hierarchical trees," *IEEE Trans. Circuits and Systems for Video Tech.*, vol. 6, pp. 243-250, June 1996.

[4] D. Taubman and M. Marcellin, *JPEG2000: Image Compression Fundamentals, Standards, and Practice*, Boston: Kluwer, 2001.

[5] V. Chande and N. Farvardin, "Progressive transmission of images over memoryless noisy channels", *IEEE Journal on Selected Areas in Communications*, vol. 18, pp. 850-860, June 2000.

[6] R. Hamzaoui, V. Stanković, and Z. Xiong, "Fast algorithm for distortion-based error protection of embedded image codes", *IEEE Trans. Image Processing*, vol. 14, pp. 1417-1421, October 2005.

[7] V. Stanković, R. Hamzaoui, and D. Saupe, "Fast algorithm for rate-based optimal error protection of embedded codes", *IEEE Trans. Communications*, vol. 51, pp. 1788-1795, November 2003.

[8] A. Nosratinia, J. Lu, and B. Aazhang, "Source-channel rate allocation for progressive transmission of images", *IEEE Trans. Communications*, vol. 51, pp. 186-196, February 2003.

[9] J. Song and K. J. R. Liu, "Robust progressive image transmission over OFDM systems using space-time block code", *IEEE Trans. Multimedia*, vol. 4, pp. 394-406, September 2002.

[10] L. Cimini, "Analysis and simulation of a digital mobile channel using orthogonal frequency division multiplexing," *IEEE Trans. Communications*, vol. 33, pp. 665-675, July 1985.

[11] I. Kalet, "The multitone channel," *IEEE Trans. Communications*, vol. 37, pp. 119-124, February 1989.

[12] B. Lu, X. Wang, and Y. Li, "Iterative receivers for space-time block-coded OFDM systems in dispersive fading channels," *IEEE Trans. Wireless Communications*, vol. 1, pp. 213-225, April 2002.

[13] Y. Li, N. Seshadri, and S. Ariyavisitakul, "Channel estimation for OFDM systems with transmitter diversity in mobile wireless channels," *IEEE Journal on Selected Areas in Communications*, vol. 17, pp. 461-471, March 1999.

[14] S. Alamouti, "A simple transmit diversity technique for wireless communications," *IEEE Journal on Selected Areas in Communications*, vol. 16, pp. 1451-1458, October 1998.

[15] V. Tarokh, N. Seshadri, and R. Calderbank, "Space-time codes for high data rate wireless communication: performance criterion and code construction," *IEEE Trans. Inform. Theory*, vol. 44, pp. 744-765, March 1998.

[16] V. Tarokh, H. Jafarkhani, and R. Calderbank, "Space-time block coding for wireless communications: performance results," *IEEE Journal on Selected Areas in Communications*, vol. 17, pp. 451-460, March 1999.

[17] V. Tarokh, H. Jafarkhani, and R. Calderbank, "Space-time block codes from orthogonal designs," *IEEE Trans. Inform. Theory*, vol. 45, pp. 1456-1467, July 1999.

[18] B. Hochwald and T. Marzetta, "Unitary space-time modulation for multiple-antenna communications in Rayleigh flat fading," *IEEE Trans. Inform. Theory*, vol. 46, pp. 543-564, March 2000.

[19] Y. Li, L. J. Cimini, and N. R. Sollenberger, "Robust channel estimation for OFDM systems with rapid dispersive fading channels," *IEEE Trans. Communications*, vol. 46, pp. 902-915, July 1998.

[20] Y. Li and N. R. Sollenberger, "Adaptive antenna arrays for OFDM systems with cochannel interference," *IEEE Trans. Communications*, vol. 47, pp. 217-229, February 1999.

[21] C.N. Georghiades and J.C. Han, "Sequence estimation in the presence of random parameters via the EM algorithm," *IEEE Trans. on Communications*, vol. 45, pp. 300-308, March 1997.

[22] G. McLachlan and T. Krishnan, *The EM Algorithm and Extensions*, New York: Wiley, 1996.

[23] B.L. Hughes, "Differential space-time modulation," *IEEE Trans. Inform. Theory*, vol. 46, pp. 2567-2578, November 2000.

[24] V. Tarokh and H. Jafarkhani, "A differential detection scheme for transmit diversity," *IEEE Journal on Selected Areas in Communications*, vol. 18, pp. 1169-1174, July 2000.

[25] D. Divsalar and M. K. Simon, "Multiple-symbol differential detection of MPSK," *IEEE Trans. Communications*, vol. 38, pp. 300-308, March 1990.

[26] Y. Liu and X. Wang, "Multiple-symbol decision-feedback space-time differential decoding in fading channels," *EURASIP Journal on Applied Signal Processing*, pp. 297-304, March 2002.

[27] R. Schober, W. Gerstacker, and J. Huber, "Decision-feedback differential detection of MDPSK for flat Rayleigh fading channels," *IEEE Trans. Communications*, vol. 47, pp. 1025-1035, July 1999.

[28] R. Schober and L. H. Lampe, "Noncoherent receivers for differential space-time modulation," *IEEE Trans. Communications*, vol. 50, pp. 768-777, May 2002.

[29] V. Stanković, R. Hamzaoui, and Z. Xiong, "Real-time error protection of embedded codes for packet erasure and fading channels. *IEEE Trans. Circuits and Systems for Video Tech.*, vol. 14, pp. 1064-1072, August 2004.

[30] M. Costa, "Writing on dirty paper," *IEEE Trans. Inform. Theory*, vol. 29, pp. 439-441, May 1983.

[31] S.I. Gelfand and M.S. Pinsker, "Coding for channel with random parameters," *Probl. Contr. and Inform. Theory*, vol. 9, pp. 19-31, 1980.

[32] M. Eyuboglu and G. Forney, "Lattice and trellis quantization with lattice- and trellis-bounded codebooks-high-rate theory for memoryless sources," *IEEE Trans. Inform. Theory*, vol. 39, pp. 46-59, January 1993.

[33] Z. Xiong, V. Stanković, S. Cheng, A. Liveris, and Y. Sun, "Source-channel coding for algebraic multiterminal binning," *Proc. ITW'04*, San Antonio, TX, Oct. 2004.

[34] R. Zamir, S. Shamai, and U. Erez, "Nested linear/lattice codes for structured multiterminal binning," *IEEE Trans. Inform. Theory*, vol. 48, pp. 1250-1276, June 2002.

[35] M. W. Marcellin and T. R. Fischer, "Trellis-coded quantization of memoryless and Gauss-Markov sources," *IEEE Trans. Communications*, vol. 38, pp. 82-93, January 1990.

[36] C. Berrou and A. Glavieux, "Near optimum error correcting coding and decoding: turbo-codes," *IEEE Trans. Communications*, vol. 44, pp. 1261-1271, October 1996.

[37] R. Gallager, *Low Density Parity Check Codes*, Cambridge: MIT Press, 1963.

[38] D. MacKay, "Good error-correcting codes based on very sparse matrices," *IEEE Trans. Inform. Theory*, vol. 45, pp. 399-431, March 1999.

[39] I. Cox, M. Miller, and A. McKellips, "Watermarking as communications with side information," *Proc. of the IEEE*, vol. 87, pp. 1127-1141, July 1999.

[40] U. Erez, S. Shamai, and R. Zamir, "Capacity and lattice-strategies for cancelling known interferences," *IEEE Trans. Inform. Theory*, vol. 51, pp. 3820-3833, November 2005.

[41] G. Caire and S. Shamai, "On the achievable throughput of a multi-antenna Gaussian broadcast channel," *IEEE Trans. Inform. Theory*, vol. 49, pp. 1691-1706, July 2003.

[42] H. Weingarten, U. Steinberg, and S. Shamai, "The capacity region of the Gaussian MIMO broadcast channel," *Proc. ISIT'04*, pp. 174, Chicago, IL, June 2004.

[43] J. Chou, S. Pradhan, and K. Ramchandran, "Turbo coded trellis-based constructions for data embedding: channel coding with side information ," *Proc. of Asilomar Conf. Signals, Systems and Computers*, vol. 1, pp. 305-309, November 2001.

[44] J. Chou, *Channel Coding with Side Information: Theory, Practice and Applications*, Ph.D. dissertation, University of California at Berkeley, Berkeley, CA, 2002.

[45] J. J. Eggers, R. Bäuml, R. Tzschoppe, and B. Girod, "Scalar costa scheme for information embedding," *IEEE Trans. Signal Processing*, vol. 51, pp. 1003-1019, April 2003.

[46] T. Philosof, U. Erez, and R. Zamir, "Combined shaping and precoding for interference cancellation at low SNR," *Proc. ISIT'03*, pp.68, Yokohama, Japan, July 2003.

[47] U. Erez and S. ten Brink, "A close-to-capacity dirty paper coding scheme," *IEEE Trans. Inform. Theory*, vol. 51, pp. 3417-3432, October 2005.

[48] A. Bennatan, D. Burshtein, G. Caire, and S. Shamai, "Superposition coding for side-information channels," submitted to *IEEE Trans. Inform. Theory*, April 2004.

[49] P. Robertson and T. Wörz, "Bandwidth-efficient turbo trellis-coded modulation using punctured component codes," *IEEE Journal on Selected Areas in Communications*, vol. 16, pp. 206-218, Feburary 1998.

[50] G. Forney, "Trellis shaping," *IEEE Trans. Inform. Theory*, vol. 38, pp. 281-300, March 1992.

[51] M. Eyuboglu and G. Forney, "Trellis precoding: combined coding, precoding and shaping for intersymbol interference channels," *IEEE Trans. Inform. Theory*, vol. 38, pp. 301-314, March 1992.

[52] H. Jin, A. Khandekar, and R. McEliece, "Irregular repeat-accumulate codes," *Proc. 2nd Intl. Symp. Turbo Codes*, pp. 1-8, September 2000.

[53] S. ten Brink and G. Kramer, "Design of repeat-accumulate codes for iterative detection and decoding," *IEEE Trans. Signal Processing*, vol. 51, pp. 2764-2772, November 2003.

[54] S. ten Brink and G. Kramer, "Turbo processing for scalar and vector channels," *Proc. 3rd Intl. Symp. Turbo Codes*, pp. 23-30, September 2003.

[55] T. M. Cover, "Broadcast channels," *IEEE Trans. Inform. Theory*, vol. 18, pp. 2-14, January 1972.

[56] P. G. Sherwood and K. Zeger, "Progressive image coding for noisy channels," *IEEE Signal Processing Letters*, vol. 4, pp. 189-191, July 1997.

[57] H. Bolckei, D. Gesbert and A. Paulraj, "On the capacity of OFDM-based spatial multiplexing systems", *IEEE Trans. Communications*, vol. 50, pp. 225-234, Feburary 2002.

[58] D. Asztely, "On antenna arrays in mobile communication systems: fast fading and GSM base station receiver algorithms", Royal Institute of Technology, Stockholm, Sweden, IR-S3-SB-9611, 1996.

[59] J. Fuhl, A. F. Molisch and E. Bonek, "Unified channel model for mobile radio systems with smart antennas", *Proc. Inst. Elect. Eng.*, vol. 145, pp. 32-41, Feburary 1998.

[60] M. Alouini and A. Goldsmith, "Adaptive modulation over Nakagami fading channels", *Kluwer Journal on Wireless Communications*, vol. 13, pp. 119-143, May 2000.

[61] J. M. Shapiro, "Embedded image coding using zerotrees of wavelet coefficients," *IEEE Trans. Signal Processing*, vol. 41, pp. 3445-3462, December 1993.

[62] University of California at Los Angeles (UCLA) Image Communications Lab, "Wavelet image coding: PSNR results," 1998.

[63] D. Taubman, "High performance scalable image compression with EBCOT," *IEEE Trans. Image Processing*, vol. 9, pp. 1158-1170, July 2000.

[64] I. Witten, R. Neal, and J. Cleary, "Arithmetic coding for data compression," *Communications of the ACM*, vol. 30, pp. 520-540, June 1987.

[65] J. Proakis, *Digital Communications*, *4th Ed.*, New York: McGraw-Hill, 2000.

[66] W. Jakes, *Microwave Mobile Communications*, Piscataway, NJ: IEEE Press, 1974.

[67] T. V. Ramabadran and S. S. Gaitonde, "A tutorial on CRC computations", *IEEE Micro*, vol. 8, pp. 62-75, August 1988.

[68] J. Hagenauer, "Rate-compatible punctured convolutional codes (RCPC codes) and their applications," *IEEE Trans. Communications*, vol. 36, pp. 389-400, April 1988.

[69] P. G. Sherwood and K. Zeger, "Error protection for progressive image transmission over memoryless and fading channels," *IEEE Trans. Communications*, vol. 46, pp. 1555-1559, December 1998.

[70] D. Sachs, R. Anand, and K. Ramchandran, "Wireless image transmission using multiple-description based concatenated code," *Proc. DCC'00*, Snowbird, UT, March 2000.

[71] V. Stanković, R. Hamzaoui and Z. Xiong, "Packet loss protection of embedded data with fast local search," *Proc. ICIP'02*, Rochester, NY, September 2002.

[72] V. Stanković, R. Hamzaoui, Z. Xiong, "Efficient channel code rate selection algorithms for forward error correction of packetized multimedia bitstreams in varying channels", *IEEE Trans. Multimedia: Special Issue on Streaming Media*, vol. 6, pp. 240-248, April 2004.

[73] C. Lan, T. Chu, K. Narayanan and Z. Xiong, "Scalable image and video transmission using irregular repeat accumulate (IRA) codes with fast algorithm for optimal unequal error protection", *IEEE Trans. Communications*, vol. 52, pp. 1092-1101, July 2004.

[74] S. Lin and D. J. Costello, *Error Control Coding: Fundamentals and Applications*, Englewood Cliffs, NJ: Prentice-Hall, 1983.

[75] V. Goyal, "Multiple description coding: compression meets the network," *IEEE Signal Processing Magazine*, vol. 18, pp. 74-93, September 2001.

[76] V. Stanković, R. Hamzaoui and Z. Xiong, "Joint product code optimization for scalable multimedia transmission over wireless channels," *Proc. ICME'02*, vol. 1, pp. 865-868, August 2002.

[77] M. Srinivasan, "Iterative decoding of multiple descriptions," *Proc. DCC'99*, pp. 463-472, March 1999.

[78] V. Vaishampayan, "Design of multiple description scalar quantizers," *IEEE Trans. Inform. Theory*, vol. 39, pp. 821-834, May 1993.

[79] A. Guyader, E. Fabre, C. Guillemot, and M. Robert, "Joint source-channel turbo decoding of entropy-coded sources," *IEEE Journal on Selected Areas in Communications*, vol. 19, pp. 1680-1696, September 2001.

[80] T. Guionnet, C. Guillemot and E. Fabre, "Soft decoding of multiple descriptions," *Proc. ICME'02*, vol. 2, pp. 601-604, August 2002.

[81] J. Kliewer and R. Thobaben, "Combining FEC and optimal soft-input source decoding for the reliable transmission of correlated variable-length encoded signals," *Proc. DCC'02*, pp. 83-91, April 2002.

[82] N. Kamaci, Y. Altunbasak, and R.M. Mersereau, "Multiple description coding with multiple transmit and receive antennas for wireless channels: the case of digital modulation," *IEEE GLOBECOM'01*, vol. 6, pp. 3272-3276, November 2001.

[83] N. At and Y. Altunbasak, "Multiple description coding for wireless channels with multiple antennas," *IEEE GLOBECOM'01*, vol. 3, pp. 2040-2044, November 2001.

[84] K. Narayanan and G. Stuber, "A serial concatenation approach to iterative demodulation and decoding," *IEEE Trans. Communications*, vol. 47, pp. 956-961, July 1999.

[85] J. Barros, J. Hagenauer, and N. Gortz, "Turbo cross decoding of multiple descriptions," *Proc. ICC'02*, vol. 3, pp. 1398-1402, May 2002.

[86] A. Nguyen and M. Ingram, "Iterative demodulation and decoding of differential space-time block codes," *Proc. VTC'00*, vol. 18, pp. 2394-2400, 2000.

[87] L. Bahl, J. Cocke, F. Jelinek, and J. Raviv, "Optimal decoding of linear codes for minimizing symbol error rate," *IEEE Trans. Vehicular Tech.*, vol. 20, pp. 284-287, March 1974.

[88] V. Chappelier, C. Guillemot, and S. Marinkovic, "Turbo trellis-coded quantization," *Proc. 5th Intl. Symp. Turbo Codes*, Brest, France, Sept. 2003.

[89] S. Shamai and R. Laroia, "The intersymbol interference channel: lower bounds on capacity and channel precoding loss," *IEEE Trans. Inform. Theory*, vol. 42, pp. 1388-1404, September 1996.

[90] J. Conway and N. Sloane, *Sphere Packings, Lattices and Groups*, New York: Springer, 1999.

[91] W. Yu, D. Varodayan, and J. Cioffi, "Trellis and convolutional precoding for transmitter-based interference pre-subtraction," *IEEE Trans. Communications*, vol. 53, July 2005.

[92] J. Hagenauer and P. Hoeher, "A Viterbi algorithm with soft-decision outputs and its applications," *Proc. GLOBECOM'89*, Dallas, TX, November 1989.

[93] G. Ungerboeck, "Channel coding with multilevel/phase signals," *IEEE Trans. Inform. Theory*, vol. 28, pp. 55-67, January 1982.

[94] S. ten Brink, "Convergence behavior of iteratively decoded parallel concatenated codes," *IEEE Trans. Communications*, vol. 49, pp. 1727-1737, October 2001.

[95] B. Chen and G. Wornell, "Achieving performance of digital watermarking systems," *Proc. IEEE Int. Conf. Multimedia Comput. Syst.*, Florence, Italy, June 1999.

[96] J. Chou and K. Ramchandran, "Turbo-based constructions for robust image and video watermarking," *Proc. ICIP'02*, Rochester, NY, September 2002.

[97] M. Miller, G. Doerr, and I. Cox, "Applying informed coding and embedding to design a robust high-capacity watermark," *IEEE Trans. Image Processing*, vol. 13, pp. 792-807, June 2004.

[98] P. Comesana, F. Perez-Gonzalez, and F. Willems, "Applying Erez and ten Brink's dirty paper codes to data-hiding," *Proc. SPIE EI'05 on Security, Steganography, and Watermarking of Multimedia Contents VII*, San Jose, CA, January 2005.

[99] J. Kusuma and K. Ramchandran, "Communicating by cosets and applications to broadcast," *Proc. CISS'02*, Princeton, NJ, March 2002.

[100] Y. Yang, Y. Sun, V. Stanković, and Z. Xiong, "Image data-hiding based on capacity-approaching dirty-paper coding," *Proc. SPIE EI'06: Security, Steganography, and Watermarking of Multimedia Contents VIII*, San Jose, CA, January 2006.

[101] D. Slepian and J.K. Wolf, "Noiseless coding of correlated information sources," *IEEE Trans. Inform. Theory*, vol. 19, pp. 471-480, July 1973.

[102] A. Wyner and J. Ziv, "The rate-distortion function for source coding with side information at the decoder," *IEEE Trans. Inform. Theory*, vol. 22, pp. 1-10, January 1976.

APPENDIX A

PERFORMANCE ANALYSIS OF STC-OFDM-BASED MIMO SYSTEM WITH
SPATIAL FADING CORRELATION

Consider the cost function in (2.15), we have

$$
\begin{aligned}
\underline{\hat{X}} &= \arg\min_{\underline{X}} \|\underline{Y} - \underline{X}\underline{H}\|^2 \\
&= \arg\min_{\underline{X}} \sum_{j=0}^{N_R-1} \sum_{n=0}^{K-1} \left\{ \left| Y_j(0,n) - \left(H_{0,j}^n X_0[n] + H_{1,j}^n X_1[n] \right) \right|^2 \right. \\
&\qquad\qquad \left. + \left| Y_j(1,n) - \left(H_{0,j}^n (-X_1^*[n]) + H_{1,j}^n X_0^*[n] \right) \right|^2 \right\} \\
&= \sum_{n=0}^{K-1} \arg\min_{\{X_i[n], i=0,1\}} \sum_{j=0}^{N_R-1} \left\{ \left| Y_j(0,n) - \left(H_{0,j}^n X_0[n] + H_{1,j}^n X_1[n] \right) \right|^2 \right. \\
&\qquad\qquad \left. \underbrace{+ \left| Y_j(1,n) - \left(H_{0,j}^n (-X_1^*[n]) + H_{1,j}^n X_0^*[n] \right) \right|^2}_{\mu(X_i[n], i=0,1)} \right\}, \quad (A.1)
\end{aligned}
$$

where $H_{i,j}^n$ denotes the frequency-domain fading coefficient of the n-th sub-carrier associated with the i-th transmit antenna and the j-th receive antenna.

From (A.1), we see that the estimation can be decoupled into K independent minimization problems, which results in the significant reduction in computing complexity.

Then we study the metric $\mu(X_i[n], i = 0, 1)$ in (A.1). After some algebra, we obtain

$$
\mu(X_i[n], i = 0, 1) = \mu_0(X_0[n]) + \mu_1(X_1[n]) - \sum_{j=0}^{N_R-1} \left\{ |Y_j(0,n)|^2 + |Y_j(1,n)|^2 \right\},
$$

where

$$\mu_0(X_0[n]) = \sum_{j=0}^{N_R-1} \left\{ \left| Y_j(0,n) - H_{0,j}^n X_0[n] \right|^2 + \left| Y_j^*(1,n) - H_{1,j}^{n*} X_0[n] \right|^2 \right\}$$

$$\mu_1(X_1[n]) = \sum_{j=0}^{N_R-1} \left\{ \left| Y_j^*(1,n) + H_{0,j}^{n*} X_1[n] \right|^2 + \left| Y_j(0,n) - H_{1,j}^n X_1[n] \right|^2 \right\}$$

Note that the last term is independent of the detection so that the metric is divided into two parts as $\mu_0(X_0[n])$ and $\mu_1(X_1[n])$. That is, we can detect $X_0[n]$ and $X_1[n]$ separately.

Furthermore, $\mu_0(X_0[n])$ and $\mu_1(X_1[n])$ are actually maximal ratio combining (MRC) metrics with combined symbols as

$$\upsilon_0[n] = \sum_{j=0}^{N_R-1} \left\{ H_{0,j}^{n*} Y_j(0,n) + H_{1,j}^n Y_j^*(1,n) \right\}$$

$$= \sum_{j=0}^{N_R-1} \left\{ \left(\left| H_{0,j}^n \right|^2 + \left| H_{1,j}^n \right|^2 \right) X_0[n] + H_{0,j}^{n*} Z_{0,j}[n] + H_{1,j}^n Z_{1,j}^*[n] \right\};$$

$$\upsilon_1[n] = \sum_{j=0}^{N_R-1} \left\{ H_{1,j}^{n*} Y_j(0,n) - H_{0,j}^n Y_j^*(1,n) \right\}$$

$$= \sum_{j=0}^{N_R-1} \left\{ \left(\left| H_{0,j}^n \right|^2 + \left| H_{1,j}^n \right|^2 \right) X_1[n] - H_{0,j} Z_{1,j}^*[n] + H_{1,j}^{n*} Z_{0,j}[n] \right\},$$

where $Z_{i,j}[n], i,j = 0,1$, is the AWGN at the n-th sub-carrier associated with the i-th transmit antenna and the j-th receive antenna.

For each metric, it combines $2N_R = 4$ diversity branches and the instantaneous SNR is $\gamma_s = \sum_{j=0}^{N_R-1} \{|H_{0,j}^n|^2 + |H_{1,j}^n|^2\}/(2\sigma_z^2)$. Based on (2.11), the correlation between any pair of $H_{i,j}^n$, $i,j = 0,1$ is obtained as

$$\mathrm{E}\{H_{i,j}^n H_{i',j'}^{n*}\} = \begin{cases} 0, & \text{for } i \neq i' \\ \sum_{l=0}^{L-1} \sigma_l^2, & \text{for } i = i'; \ j = j' \\ \sum_{l=0}^{L-1} \sigma_l^2 \rho_l(\Delta, \bar{\theta}_l, \sigma_{\theta_l}), & \text{for } i = i'; \ j \neq j' \end{cases}$$

After some algebra, we can compute the pdf of γ_s as

$$p_{\gamma_s}(x) = \frac{1}{4\rho^3(\bar{\gamma}_c)^2} \left\{ \left(\rho x + \bar{\gamma}_c(1-\rho^2)\right) e^{-x/(\bar{\gamma}_c(1-\rho))} + \left(\rho x - \bar{\gamma}_c(1-\rho^2)\right) e^{-x/(\bar{\gamma}_c(1+\rho))} \right\},$$

where $\rho = \left| \frac{\sum_{l=0}^{L-1} \sigma_l^2 \rho_l(\Delta, \bar{\theta}_l, \sigma_{\theta_l})}{\sum_{l=0}^{L-1} \sigma_l^2} \right|$, and $\bar{\gamma}_c$ is the average SNR of each branch, which can be shown to be half of the average SNR of the MIMO system (denoted by $\bar{\gamma}_s$) with two transmit antennas. If we also consider the penalty on SNR by inserting $G \geq L - 1$ guard intervals in the OFDM system, we have $\bar{\gamma}_c = \frac{K}{K+G} \cdot \frac{\bar{\gamma}_s}{2}$.

Then the average BER of the MIMO system is given by

$$P_b = \int_0^\infty P_b(x) p_{\gamma_s}(x) dx, \tag{A.2}$$

where $P_b(x)$ is the BER performance over AWGN channel with SNR x. For M-PSK modulation, $P_b(x)$ is computed by

$$P_b(x) \cong \frac{N_m}{\log_2 M} Q\left(\sqrt{2x \sin^2 \frac{\pi}{M}}\right) \quad \text{with } N_m = \begin{cases} 1, & M = 2 \\ 2, & M > 2 \end{cases}. \tag{A.3}$$

Note that (A.3) is an exact close-form expression of BER for BPSK and QPSK. When $M > 4$, it is also a good approximation if Gray mapping is applied.

By substituting (A.3) into (A.2), we obtain the average BER as

$$P_b \cong \frac{N_m}{\log_2 M} \cdot \frac{1}{16\rho^3} \left\{ 8\rho^3 + f(1+\rho)(2 - \rho - 8\rho^2 - 5\rho^3) + f(1-\rho)(-2 - \rho + 8\rho^2 - 5\rho^3) \right.$$
$$\left. + f^3(1+\rho)(\rho + 2\rho^2 + \rho^3) + f^3(1-\rho)(\rho - 2\rho^2 + \rho^3) \right\}$$

with $N_m = \begin{cases} 1, & M = 2 \\ 2, & M > 2 \end{cases}$, $f(\xi) = \sqrt{\frac{\frac{K}{K+G} \cdot \frac{\bar{\gamma}_s}{2} \sin^2 \frac{\pi}{M} \cdot \xi}{\frac{K}{K+G} \cdot \frac{\bar{\gamma}_s}{2} \sin^2 \frac{\pi}{M} \cdot \xi + 1}}$.

APPENDIX B

PERFORMANCE ANALYSIS OF STC-OFDM-BASED MIMO SYSTEM WITH
TIME VARIANCE

Model (2.14) is only built upon frequency-domain symbols. To study the effect
of time variance in OFDM systems, we need to examine the data transform and
transmission in both time domain and frequency domain.

We still consider the STC-OFDM-based MIMO system with K sub-carriers,
$N_T = 2$ transmit antennas and $N_R = 2$ receive antennas, signalling through an L-tap
frequency-selective fading channel. Let $\{X_i[n]\}_{n=0}^{K-1}, i = 0, 1$, denote the frequency-
domain transmitted symbol sequence from the i-th transmit antenna. These two
sequences go through an STC encoder and then IFFT blocks to obtain the four time-
domain transmitted sequences as

$$
\begin{aligned}
x_0[0,q] &= \frac{1}{\sqrt{K}} \sum_{n=0}^{K-1} X_0[n] e^{j\frac{2\pi qn}{K}}; \quad x_1[0,q] = \frac{1}{\sqrt{K}} \sum_{n=0}^{K-1} X_1[n] e^{j\frac{2\pi qn}{K}}; \\
x_0[1,q] &= \frac{1}{\sqrt{K}} \sum_{n=0}^{K-1} (-X_1^*[n]) e^{j\frac{2\pi qn}{K}}; \quad x_1[1,q] = \frac{1}{\sqrt{K}} \sum_{n=0}^{K-1} X_0^*[n] e^{j\frac{2\pi qn}{K}}, \quad \text{(B.1)}
\end{aligned}
$$

where $\{x_i[p,q]\}_{q=0}^{K-1}, i = 0, 1; p = 0, 1$, is the time-domain symbol sequence trans-
mitted through the i-th antenna during the p-th OFDM slot in one STC-OFDM
codeword.

To mitigate the effect of inter-symbol interference (ISI), we insert guard intervals
by adding a cyclic suffix to each transmitted sequence. Then the transmitted sequence
with guard interval is $x_i^g[p,q] = x_i[p, q \bmod K], \quad i = 0, 1; \ p = 0, 1; \ q = 0, 1, \ldots, K +$
$G - 1$, where G is the length of guard interval and it must satisfy $G \geq L - 1$.

At the j-th receiver, the received time-domain sequences during the two consecutive OFDM slots are given respectively by

$$
\begin{aligned}
y_j^g(0, q) &= \sum_{l=0}^{L-1} h_{0,j}^l[0, q] x_0^g[0, q - l] + \sum_{l=0}^{L-1} h_{1,j}^l[0, q] x_1^g[0, q - l] + z_j[0, q]; \\
y_j^g(1, q) &= \sum_{l=0}^{L-1} h_{0,j}^l[1, q] x_0^g[1, q - l] + \sum_{l=0}^{L-1} h_{1,j}^l[1, q] x_1^g[1, q - l] + z_j[1, n], \\
& q = 0, 1, \ldots, K + G - 1; \ \ j = 0, 1,
\end{aligned}
\tag{B.2}
$$

where $y_j^g(p, q)$ is the time-domain received symbol in the q-th time slot during the p-th OFDM slot at the j-th receive antenna; $z_j[p, n]$ is the AWGN with variance σ_z^2; $h_{i,j}^l[p, q]$ is the time-domain fading coefficient of the l-th tap at the q-th time slot in the p-th OFDM slot associated with the i-th transmit antenna and the j-th receive antenna. Each fading coefficient is independent of other taps and has the same normalized correlation function with average power $\sigma_l^2, l = 0, 1, \ldots, L - 1$. Since we transmit the symbol sequences during two consecutive OFDM slots, $h_{i,j}[p, n, l]$ can be denoted by $h_{i,j}[k, l]$ with $k = p(K + G) + n, p = 0, 1$, the fading coefficient of the l-th tap at the $(p(K + G) + n)$-th time slot in one STC-OFDM codeword. We assume Jakes' fading channel model [66] with correlation function as (2.2).

When a symbol sequence is received, the first G symbols in the sequence are assumed to be corrupted by ISI from the previous sequence. We remove the ISI by replacing these symbols with the cyclic suffix, i.e., $y_j(p, q) = y_j^g(p, G + (q - G) \bmod K)$, $p = 0, 1$; $q = 0, 1, \ldots, K - 1$.

By performing FFT to these symbol sequences, we obtain the frequency-domain received sequences as

$$
\begin{aligned}
Y_j(0,n) &= \frac{1}{\sqrt{K}} \sum_{q=G}^{K+G-1} \left\{ \sum_{l=0}^{L-1} h_{0,j}^l[0,q] x_0[0,q-l] \right. \\
&\qquad\qquad \left. + \sum_{l=0}^{L-1} h_{1,j}^l[0,q] x_1[0,q-l] + z_j[0,q] \right\} e^{-j\frac{2\pi n q}{K}}; \\
Y_j(1,n) &= \frac{1}{\sqrt{K}} \sum_{q=G}^{K+G-1} \left\{ \sum_{l=0}^{L-1} h_{0,j}^l[1,q] x_0[1,q-l] \right. \\
&\qquad\qquad \left. + \sum_{l=0}^{L-1} h_{1,j}^l[1,q] x_1[1,q-l] + z_j[1,q] \right\} e^{-j\frac{2\pi n q}{K}}, \\
&\qquad n = 0,1,\ldots,K-1; \;\; j = 0,1.
\end{aligned}
\tag{B.3}
$$

Now we substitute (B.1) into (B.3) to carry on the derivation.

$$
\begin{aligned}
Y_j(0,n) &= X_0[n] \left\{ \frac{1}{K} \sum_{q=G}^{K+G-1} H_{0,j}^n[0,q] \right\} + X_1[n] \left\{ \frac{1}{K} \sum_{q=G}^{K+G-1} H_{1,j}^n[0,q] \right\} \\
&\quad + \underbrace{\sum_{p=0}^{1} \sum_{m=0,m\neq n}^{K-1} X_p[m] \left\{ \frac{1}{K} \sum_{q=G}^{K+G-1} H_{p,j}^m[0,q] e^{-j\frac{2\pi(n-m)q}{K}} \right\}}_{\omega_j[0,n]} \\
&\quad + \frac{1}{\sqrt{K}} \sum_{q=0}^{K-1} z_j[0,q] e^{-j\frac{2\pi n q}{K}}; \\
Y_j(1,n) &= (-X_1^*[n]) \left\{ \frac{1}{K} \sum_{q=G}^{K+G-1} H_{0,j}^n[1,q] \right\} + X_0^*[n] \left\{ \frac{1}{K} \sum_{q=G}^{K+G-1} H_{1,j}^n[1,q] \right\} \\
&\quad + \underbrace{\sum_{p=0}^{1} \sum_{m=0,m\neq n}^{K-1} (-1)^{(1-p)} X_{1-p}^*[m] \left\{ \frac{1}{K} \sum_{q=G}^{K+G-1} H_{p,j}^m[1,q] e^{-j\frac{2\pi(n-m)q}{K}} \right\}}_{\omega_j[1,n]} \\
&\quad + \frac{1}{\sqrt{K}} \sum_{q=0}^{K-1} z_j[1,q] e^{-j\frac{2\pi n q}{K}}, \quad n = 0,1,\ldots,K-1; \; j = 0,1,
\end{aligned}
\tag{B.4}
$$

where $H_{i,j}^m[p,q] = \sum_{l=0}^{L-1} h_{i,j}^l[p,q] e^{-j\frac{2\pi l m}{K}}$ is the frequency-domain fading coefficient as-

sociated with the m-th sub-carrier; $\omega_j[0, n]$ and $\omega_j[1, n]$ are inter-channel interferences (ICI) from other sub-carriers due to a loss of sub-carrier orthogonality.

In model (2.14), the ICIs are ignored. And constant fading channels within an STC-OFDM codeword are also assumed. However, this assumption does not hold in (B.4) since the practical channels are time-varying. One straightforward solution is to take the mean of all fading coefficients during one STC-OFDM codeword as a new common fading coefficient, i.e.,

$$
\begin{aligned}
Y_j(0, n) &= \underbrace{X_0[n]\bar{H}_{0,j}^n + X_1[n]\bar{H}_{1,j}^n}_{\beta_j[0,n]} + \omega_j[0, n] + \underbrace{X_0[n]\widetilde{H}_{0,j}^n + X_1[n]\widetilde{H}_{1,j}^n}_{\nu_j[0,n]} \\
&\quad + \underbrace{\frac{1}{\sqrt{K}} \sum_{q=0}^{K-1} z_j[0, q] e^{-j\frac{2\pi nq}{K}}}_{Z_j[0,n]}; \\
Y_j[1, n] &= \underbrace{(-X_1^*[n]\bar{H}_{0,j}^n + X_0^*[n]\bar{H}_{1,j}^n}_{\beta_j[1,n]} + \omega_j[1, n] + \underbrace{X_1^*[n]\widetilde{H}_{0,j}^n - X_0^*[n]\widetilde{H}_{1,j}^n}_{\nu_j[1,n]} \\
&\quad + \underbrace{\frac{1}{\sqrt{K}} \sum_{q=0}^{K-1} z_j[1, q] e^{-j\frac{2\pi nq}{K}}}_{Z_j[1,n]}, \\
&\quad n = 0, 1, \dots, K - 1; \ j = 0, 1, \quad\quad\quad\quad\quad\quad\quad \text{(B.5)}
\end{aligned}
$$

where $\bar{H}_{i,j}^n = \frac{1}{K} \sum_{q=G}^{K+G-1} \frac{H_{i,j}^n[0,q] + H_{i,j}^n[1,q]}{2}$ is the constant fading coefficient within one STC-OFDM symbol associated with the n-th sub-carrier between the i-th transmit antenna and the j-th receive antenna; and $\widetilde{H}_{i,j}^n = \frac{1}{K} \sum_{q=G}^{K+G-1} \frac{H_{i,j}^n[0,q] - H_{i,j}^n[1,q]}{2}$ is the remainder after compensating the modelling mismatch from the time-varying fading channels.

In this way each received symbol is divided into four parts. Specifically, $\beta_j[p, n]$ is the combined transmitted symbol; $\omega_j[p, n]$ is the ICI from other sub-carriers; $\nu_j[p, n]$ is the interference within the n-th sub-carrier caused by modelling mismatch. To

distinguish this interference with the ICI above, we call it intra-channel interference (IACI); $Z_j[p,n]$ is the AWGN in frequency domain.

Since $\mathrm{E}\left\{X_i[n]X_{i'}^*[n']\right\} = \frac{1}{2}\delta_{ii'}\delta_{nn'}$, we show that $\beta_j[p,n]$, $\omega_j[p,n]$, $\nu_j[p,n]$ and $Z_j[p,n]$ are independent complex Gaussian random variables with their own variances as

$$
\mathrm{E}\left\{\beta_j[p,n]\beta_j^*[p,n]\right\} = \frac{\sum_{l=0}^{L-1}\sigma_l^2}{K^2}\sum_{m=0}^{K-1}\sum_{m'=0}^{K-1}\Big\{J_0(2\pi f_D(m-m')T)
$$
$$
+ J_0(2\pi f_D(m-m'+K+G)T)\Big\};
$$

$$
\mathrm{E}\left\{\omega_j[p,n]\omega_j^*[p,n]\right\} = \frac{2\sum_{l=0}^{L-1}\sigma_l^2}{K^2}\Big\{(K-1)K - 2\sum_{m=1}^{K-1}(K-m)J_0(2\pi f_D mT)\Big\};
$$

$$
\mathrm{E}\left\{\nu_j[p,n]\nu_j^*[p,n]\right\} = \frac{\sum_{l=0}^{L-1}\sigma_l^2}{K^2}\sum_{m=0}^{K-1}\sum_{m'=0}^{K-1}\Big\{J_0(2\pi f_D(m-m')T)
$$
$$
- J_0(2\pi f_D(m-m'+K+G)T)\Big\};
$$

$$
\mathrm{E}\left\{Z_j[p,n]Z_j^*[p,n]\right\} = 2\sigma_z^2.
$$

By regarding both ICI and IACI as additive Gaussian noise terms, we can also compute the BER performance by (2.16), but with a new function $f(\xi)$ as

$$
f(\xi) = \sqrt{\frac{\frac{K}{K+G}\cdot\frac{\bar{\gamma}_s^{\mathrm{TV}}}{2}\sin^2\frac{\pi}{M}\cdot\xi}{\frac{K}{K+G}\cdot\frac{\bar{\gamma}_s^{\mathrm{TV}}}{2}\sin^2\frac{\pi}{M}\cdot\xi+1}},
$$

$$
\text{with}\qquad \bar{\gamma}_s^{\mathrm{TV}} = \frac{\mathrm{E}\left\{\beta_j[p,n]\beta_j^*[p,n]\right\}}{\mathrm{E}\left\{\omega_j[p,n]\omega_j^*[p,n]\right\}+\mathrm{E}\left\{\nu_j[p,n]\nu_j^*[p,n]\right\}+\mathrm{E}\left\{Z_j[p,n]Z_j^*[p,n]\right\}}
$$
$$
= \frac{\bar{\gamma}_s\cdot\psi(f_D,T,K,G)}{\bar{\gamma}_s\left(1-\psi(f_D,T,K,G)\right)+1},
$$

$$
\psi(f_D,T,K,G) = \frac{1}{2K^2}\sum_{m=0}^{K-1}\sum_{m'=0}^{K-1}\Big\{J_0(2\pi f_D(m-m')T)+J_0(2\pi f_D(m-m'+K+G)T)\Big\}.
$$

where $\bar{\gamma}_s$ is the average SNR of the MIMO system; The factor $\frac{K}{K+G}$ is the penalty on SNR by inserting guard intervals.

VITA

Yong Sun received the B.S. and M.S. degrees from the Department of Electrical Engineering, Tsinghua University, Beijing, P.R. China, in 1998 and 2001 respectively. In 2005, he received the Ph.D. degree in electrical engineering from Texas A&M University, College Station, TX.

From 2001 to 2005, he was a Research Assistant with the Department of Electrical Engineering at Texas A&M University. He spent the summer of 2005 at Microsoft Research, Redmond, WA as a Research Intern. His research interests include source-channel coding, multimedia signal processing, coding theory, and digital communications.

He was the recipient of the Ebensberger/Fouraker Graduate Fellowship (2005). He also served as a review for many publications, including IEEE Transactions on Communications, IEEE Communication Letters, IEEE Transactions on Signal Processing, and IEEE Transactions on Wireless Communications.

In his graduate career, he had 5 journal papers and 8 conference papers published, and another journal paper submitted.

He can be reached at: Apt. 531, No. 46, Zhongsheng St., Dadong District, Shenyang, Liaoning, P.R. China, 110044.

The typist for this thesis was Yong Sun.